UNIVERSITÀ
degli STUDI
di CATANIA

Dipartimento
di Fisica
e Astronomia
"Ettore Majorana"

PhD programme in physics

Giuseppe Gallo

First multi-year muography of Etna Volcano

PhD thesis

Supervisor:
Prof. D. Lo Presti

---

academic year 2018/2019

Contents

Introduction

The muon was discovered in 1936 by American physicists C. D. Anderson and S. Neddermeyer during their extensive cloud-chamber experiments at the California Institute of Technology for the purpose of studying the energy lost by cosmic rays in matter. From their results, they concluded that "there exist particles of unit charge, but with a mass larger than that of a normal free electron and much smaller than that of a proton" [1]. For this reason, Anderson initially gave it the name of *mesotron*. In 1937 J. C. Street and E.C. Stevenson, while working at Harvard University, established beyond any doubt the existence of this new particle and provided a fairly estimate of about 200 electron masses for its mass [2]. Since that moment, the history of muon science began.

The idea of using muons as a probe to inspect the internal structure of large size objects dates back to 1955 with the pioneer work of E.P. George [3]. He measured the muon flux inside and outside a tunnel to calculate the transmission rate and measured an areal density of overburden rock consistent with the result of drilling and sampling at the same site. He took this measurement with a Geiger counter and, therefore, he wasn't able to image the density structure. A milestone in the development of *muography* - or muon radiography - is the famous experiment of L. Alvarez in 1970 [4]. He attempted to use spark chambers with digital readout units inside the Chephren's pyramid in Egypt to search for hidden chambers. Although the collaboration did not succeeded in this goal, they demonstrated that the areal density of the pyramid was measured with a precision of 2% over a muon path of 100 m of limestone rock.

The high visibility and historical importance of the target, had given a big resonance to the work of Alvarez. The same thing happened almost fifty years later, in 2017, after that a secret chamber was discovered inside the 4500 years old Great Pyramid in Giza, Egypt, by means of muon radiography [5]. But in the last fifteen years, we are witnessing the return of muon-based imaging and the plethora of application fields requiring penetrating probes is continuously expanding. Archaeology, geology, mining, civil engineering and civil protection are all fields where muon imaging is applied as an inspection method complementary to traditional techniques, with the aim to overcome their limitations or to access information otherwise unachievable.

Here, the results of the first multi-year muography experiment at Etna Volcano is presented. The Muography of Etna Volcano (MEV) project started in 2016 and the candidate took part in all activities since the beginning, as will be explained in the following. The collaboration involves physicists and engineers belonging to Department of Physics and Astronomy "E. Majorana", University of Catania, National Institute for Nuclear Physics (INFN) - Catania division and Southern National Laboratory (LNS), and National Institute for Astrophysics (INAF) - Catania Astrophysical Observatory, geophysicists and volcanologists from both Department of Biological, Geological and Environmental Sciences, University of Catania, and from National Institute for Geophysics and Volcanology (INGV) - Etna Observatory [6].

Volcanic activity is regulated by complex coupled phenomena occurring in the plumbing system, from shallow depths to several kilometers below the ground surface. In persistently active volcanoes (like Etna), paroxysmal activity occurs when the system is driven out of its dynamical equilibrium state [7]. Mitigation of volcanic hazards relies on the capability of interpreting surface observation in terms of subsurface processes that may tip a volcano out of its equilibrium state. Monitoring of active volcanoes and also the investigation of their internal structure is presently based on the study of ground deformation, seismicity, gas emission and gravity, in particular to determine the density distribution inside the structures [8, 9]. Despite great improvements, gravity surveying remains a challenging, costly and difficult method, especially under harsh environmental conditions and in presence of very uneven topogra-

phy [10]. Furthermore, conventional gravity measurements may quickly reach their limits in applications where high resolution is required to monitor density changes [11]. Get access to high resolution density maps of lava domes and plumbing systems subject to high hydrothermal variations is of primary importance to better constrain hazard models. This blind spot represents a vulnerability of volcano monitoring systems exclusively based on traditional techniques. Nevertheless, they allow to get reliable information about processes that occur at greater depth and on the whole density structure. Instead, muon radiography is limited to the shallow levels of volcanic edifice and gives information only on portions of the structure crossed by these particles. The just exposed differences between the two methods stress the importance to elaborate muon transmission data to improve also gravity surveying.

For the benefit of readers that are approaching for the first time to muon radiography and for the sake of completeness, the second part of this introduction is spent to remind principles underlying muon radiography. In the end, the history of muon imaging applications to volcanoes is summarized. Readers already familiar with this arguments may skip these lines and go to the first chapter for the design of the first muon telescope detector built within the MEV project. The second chapter describes procedures implemented to reconstruct muon tracks from raw data and characterize telescope performance. Third chapter, in conclusion, shows the preliminary muography results obtained until now with the first detector prototype operating on the slope of Etna North-East Crater.

Muon imaging principles

Cosmic-ray muon flux

Today we know that cosmic-ray muons are continuously irradiating everything on the Earth surface. At sea level, the integral intensity of vertical muons is approximately $70\,\mathrm{m}^{-2}\mathrm{s}^{-1}\mathrm{sr}^{-1}$, with a rough $\cos^2(\theta)$ dependence, where θ is the zenith angle measured from the vertical axis [12]. Primary cosmic rays arriving at the top of the atmosphere are composed

of about 98% of protons and ions, while the remaining 2% of electrons. The first group consists of 87% of protons, 12% of Helium nuclei (alpha particles) and the last 1% of heavier nuclei. The interaction of primary cosmic-ray protons with nuclei like N, O, and others in air, produces a large quantity of pions (π) and kaons (K), as well as nucleons. These particles, referred as "secondaries", have sufficient energy to continue the cascade multiplication until energy per nucleon goes below threshold for pion production, about 1 GeV [13]. Protons lose energy by ionization and the major part of them with energy lower than 1 GeV stops in the atmosphere. Neutral pi mesons (π^0) with their short lifetime, 8.52×10^{-17}s, decay in two γ-rays, each of which initiates an electromagnetic shower. Muons in the atmosphere are favourable produced mainly by the decay of charged mesons. The most important decay channels with their respective branching ratio are:

$$\left.\begin{aligned}\pi^- &\to \mu^- + \overline{\nu}_\mu \\ \pi^+ &\to \mu^+ + \nu_\mu\end{aligned}\right\} \quad (\sim 100\%)\,, \qquad \left.\begin{aligned}K^- &\to \mu^- + \overline{\nu}_\mu \\ K^+ &\to \mu^+ + \nu_\mu\end{aligned}\right\} \quad (\sim 63.5\%)\,.$$

In turn, low energy muons decay into electron or positron and electron and muon neutrinos:

$$\left.\begin{aligned}\mu^- &\to e^- + \overline{\nu}_e + \nu_\mu \\ \mu^+ &\to e^+ + \nu_e + \overline{\nu}_\mu\end{aligned}\right\} \quad (\sim 100\%)\,.$$

Figure 1 shows the vertical fluxes of principal cosmic-ray components in atmosphere in the energy region where particles are most numerous (except for the electrons, which are most numerous near their critical energy, which is about 81 MeV in air).

The fundamental properties of muons and also their interactions with other particles are the basis for muography, as for each research using these particles. In one sentence, they can be depicted as follows:

> Muons are unstable elementary particles of two charge types (positive μ^+ and negative μ^-) having a spin of 1/2, an usual mass of 105.6 MeV/c^2 and 2.2 µs lifetime.

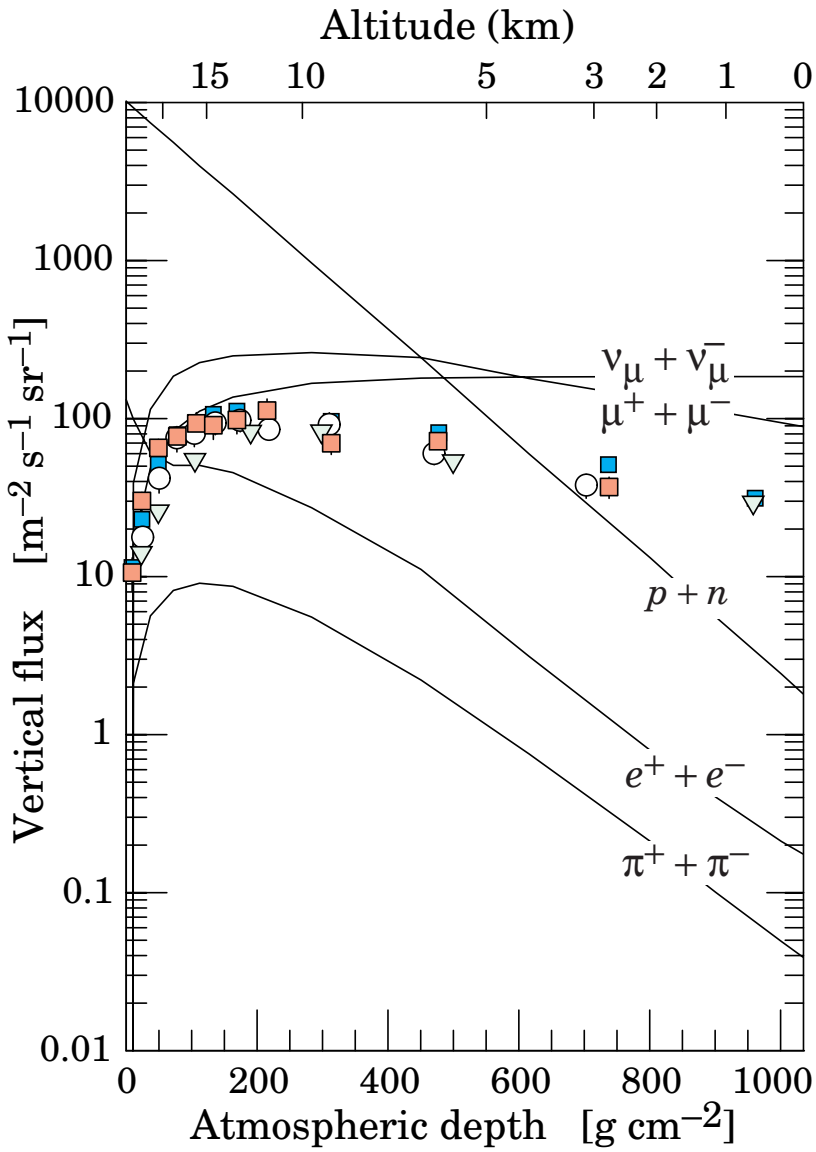

Figure 1: Vertical fluxes of cosmic rays particles (except photons) as a function of the depth in the atmosphere, taken from [12]. Points are measurements for negative muons above 1 GeV [14–19].

These properties explain why muons weakly interact with matter and dominates by more than one order of magnitude the flux of other cosmic particle at sea level. With their large mass compared to electron ($m_\mu \approx 207\, m_e$), muon energy loss by Bremsstrahlung is 40000 times smaller than that of electrons with the same energy, being proportional to $1/m^2$. Ionization and excitation, therefore, dominate the muon energy loss up to energies of about 500 GeV.

Muons produced in the interaction of high energy primary cosmic rays have high β, consequently, and are extremely penetrating, because they have virtually no nuclear interaction and their ionization losses are small. To an external observer, they decay with a lifetime of $2.2 \times 10^{-6}\gamma$ s because of relativistic time dilatation, where γ is the Lorentz factor, $\gamma = \left(1 - v^2/c^2\right)^{-1/2}$. This lifetime translate into a long mean decay length L in air, given by $L\,[\mathrm{km}] = 6200 \times E\,[\mathrm{TeV}]$ [13]. Because muons are created at an altitude of about 10 km, the ones with energy $E \geq 2\,\mathrm{GeV}\,[\gamma \geq 20]$ suffer little decay during the time required to observe them at Earth surface. At larger θ, i.e. near the horizontal, muon path in the atmosphere becomes longer and this favours the decay of low energy muons, resulting in a increased mean energy. Figure 2 shows the muon energy spectrum at sea level for four angles.

A semi-empirical extrapolation formula for the mean flux at sea level, valid when muon decay is negligible ($E > 100\,\mathrm{GeV}/\cos\theta$) and the Earth spherical shape can be neglected ($\theta < 70^\circ$), is:

$$\frac{dN}{dEd\Omega} \approx A\frac{0.14E^{-\gamma}}{\mathrm{cm}^2\,\mathrm{s}\,\mathrm{sr}\,\mathrm{GeV}} \times \left(\frac{1}{1 + \frac{a_0\tilde{E}\cos\theta^\star}{E_\pi}} + \frac{B}{1 + \frac{a_1\tilde{E}\cos\theta^\star}{E_K}} + r_c\right), \qquad (1)$$

where the two terms represents the contribution of pions and kaons to muon yield. The parameters A, γ and r_c refer to the overall scale factor, spectrum index and ratio of the prompt muons to pions, respectively [32]. The original equation of the spectrum was proposed by T. K. Gaisser with $A = 1$, $B = 0.054$, $\gamma = 2.7$, $\theta = \theta^\star$, $\tilde{E} = E$, $E_\pi = 115\,\mathrm{GeV}$, $E_K = 850\,\mathrm{GeV}$ and $a_0 = a_1 = 1.1$ [20]. The new variable $\theta^\star$ represents the angle of incoming primary cosmic ray respect to the normal to upper atmospheric layer. It is introduced to distinguish it from the zenith angle θ measured on the ground surface and take into account the spherical geometry of

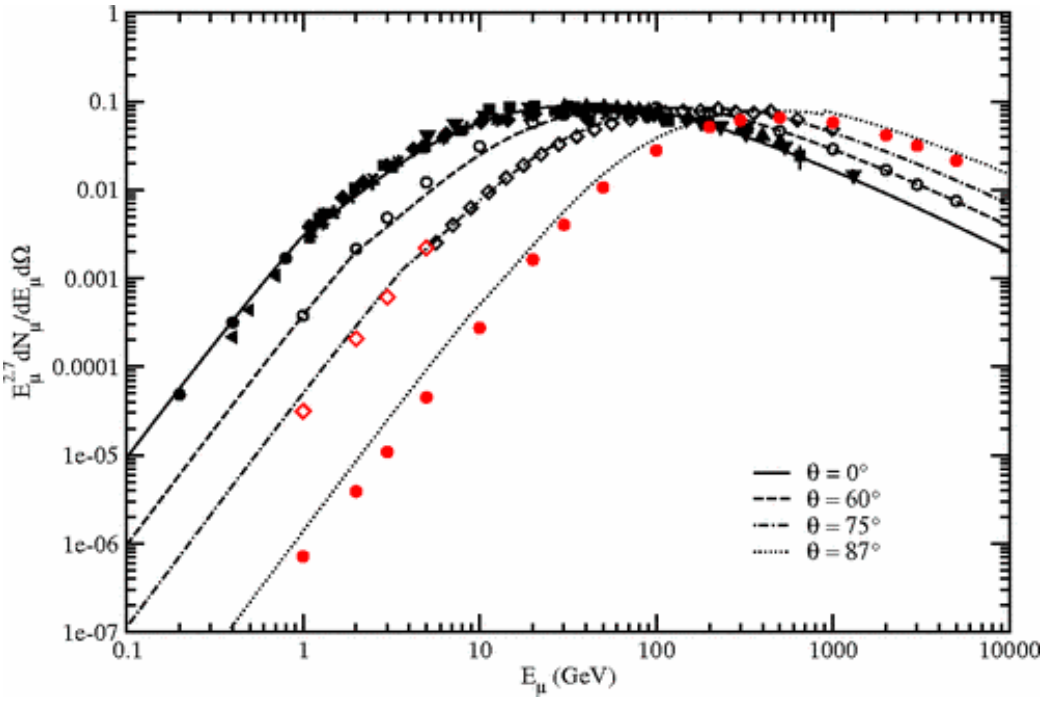

Figure 2: Spectrum of muons at $\theta = 0°$, $\theta = 60°$, $\theta = 75°$ and $\theta = 87°$. Experimental data are taken from [20], [21–31]. The line plots represents the fits of the modified Gaisser parameterization to experimental data in the low energy regime by Eqs. (1), (2) and (3). Reprinted figure with permission from [32], Copyright (2019) by the American Physical Society.

the Earth. This correction is important at large angles ($\theta > 70^\circ$), at which particles have to traverse greater thickness of atmospheric layer. In low energy limit, the original Gaisser parametrization is significantly higher than the observed values. In addition, E needs to be slightly modified by the energy loss through the atmosphere (Δ). To take into account all these requirements, the following adjustments are adopted for $E < 100\,\mathrm{GeV}/\cos\theta$:

$$r_c = 10^{-4}, \tag{2a}$$

$$\tilde{E} = E + \Delta, \quad \text{with} \quad \Delta = 2.06 \times 10^{-3} \left(\frac{950}{\cos\theta^\star} - 90 \right), \tag{2b}$$

$$A = 1.1 \left(\frac{90\sqrt{\cos\theta + 0.001}}{1030} \right)^{\left(\frac{4.5}{E \cos\theta^\star,} \right)}, \tag{2c}$$

$$\cos\theta^\star = \sqrt{\frac{x^2 + p_1^2 + p_2 x^{p_3} + p_4 x^{p5}}{1 + p_1^2 + p_2 + p_4}}, \tag{2d}$$

where $x \equiv \cos\theta$, $p_1 = 0.102573$, $p_2 = -0.068287$, $p_3 = 0.958633$, $p_4 = 0.0407253$, and $p_5 = 0.817285$. It should be noted that $\cos\theta$ inside the square root in Eq. (2c) doesn't have a star. In the lowest energy region ($E \leq 1\,\mathrm{GeV}/\cos\theta^\star$), the modifications by Eqs. (2) are not sufficient to fit the data. The substitution

$$E \to \frac{3E + 7\sec\theta^\star}{10} \tag{3}$$

is made before E is passed to Eqs. (2). The complete set of Eqs. (1–3) is based on the world data set. The modified Gaisser formula strongly departs from data only at very large angle ($\theta > 85^\circ$) and the worst disagreement reaches 40%, but it occurs only at low energy ($E_{\mu 0} < 10\,\mathrm{GeV}$). Hence, the integrated spectrum is dominated by the accurate parts of the parameterization at small angles.

Cosmic muon flux may be considered stable at first approximation, but, in fact, there are some factors that can induce variations both in space and time. The list of possible agents which affect muon flux includes:

- altitude: as can be seen in Fig. 1, muon flux intensity and composition depends on altitude, i.e on the path between air shower cores and observation point;
- latitude: Earth's magnetic field acts as a filter against low energy primary cosmic ray, when they travel through magnetosphere before reaching the atmosphere. Close to the equator particles need to have a minimum rigidity to reach the atmosphere, resulting in a lower flux compared to the regions near geomagnetic poles;
- solar activity: variations in the solar wind velocity modulate the low energy spectrum of cosmic ray particles in the atmosphere;
- atmospheric conditions (e.g. temperature, density, pressure) change the characteristic of cosmic rays interactions in air and, thus, in muon production.

Among these factors, altitude is the most relevant for muon imaging. It can determine time-independent effects which produce a significant discrepancy between measured and modelled or simulated muon flux, if the latter refer to sea level. Other effects could be disregarded, except for seasonal atmospheric fluctuations that should be taken into account if experiments are repeated at different times. Long term measurements by means of underground detectors (MACRO detector, in the Gran Sasso Laboratory, Italy, and IceCube Observatory, deep in the Antarctic ice) found a seasonal fluctuation in high energy muon rate between $\pm 5\%$ and $\pm 10\%$ [33,34]. In both cases, a high correlation between temperature variation in the atmosphere above observation points and fluctuation in muon integral intensity was found. Values reported in literature for correlation coefficient between pressure changes and muon intensity is of the order of -0.5% per mbar for energies around $10\,\mathrm{GeV}$, that implies negligible muon intensity fluctuations for typical pressure variations of a few tens of mbar.

Muon interaction in matter

The interaction of muons with atoms of matter they cross results in a loss of energy and in a deviation from their initial direction (scattering), as for

every charged particle. It is possible to distinguish two kinds of muon imaging, according to which effect of interaction they are based on.

Deviation muography relies on the tracking of the scattering angle of individual muons in order to produce a density map of the object in study. According to Moliere theory, the angular deviation due to the addition of many small interactions roughly follows a Gaussian distribution of zero mean value and standard deviation θ_M:

$$\theta_M = \frac{13.6\,\mathrm{MeV}}{\beta c p} Q \sqrt{\frac{x}{X_0}} \left(1 + 0.038 \ln\left(x/X_0\right)\right), \tag{4}$$

where p is the particle momentum in MeVc^{-1}, β is the relativistic factor, Q is the absolute charge of muon, x is the material thickness and X_0 is the radiation length typical of the medium. X_0 decreases rapidly as the atomic number of the material grows up, and θ_M increases consequently. However, target maximum size is limited by the requirement of tracking muons both before and after traversing it. Furthermore, this technique is valid only for scattering centres confined in such a way that it is possible to assume that a single main diffusion event takes place. The Muon Portal Project is an application of deviation muography for container inspection from outside, in which the candidate was involved during the last part of commissioning phase [35].

Here, we consider the usage of muons to inspect the internal structure of gigantic objects according to the well-known concept of *radiography*. The most popular radiography is the X-ray image of the human body. In general, it is possible to consider the following definition:

> Radiography is an imaging technique using energetic particles to reveal the opacity, i.e density times length, of an object. A certain amount of particles projected to the object is absorbed, depending on its density distribution. Particles that pass through the object are captured by a detector behind it.

In the previous lines are summarized the key elements to produce a radiography: a source of energetic particles and a detector. As depicted in Table 1, among various particles, muons are the most suited for very large-size object such a mountain.

Muon energy loss in matter depends on the material density ρ and on

Particle	Basic interaction	Penetration characteristics
Electron, X-ray	Electromagnetic	A few meters or less for conversion
Proton, neutron, pion	Strong and electromagnetic	$\sim$10 m for absorption
Neutrino	Weak	Earth-size and difficult to detect
Muon	Electromagnetic and weak	$10^2 - 10^3$ m and easy to detect

Table 1: Scale of radiography by various particles, taken from [36].

its size. It is possible to formally define a new quantity, the *opacity* ϱ, as

$$\varrho\left(L\right) = \int_L \rho\left(x\right) dx, \tag{5}$$

where x is the muon path measured along particle trajectory L. In other words, opacity is the density integrated over the path length. Cosmic-ray muons are relativistic particles which weakly interact with matter, mainly through ionization. The loss of energy can be written as:

$$-\frac{dE}{d\varrho} = a\left(E\right) + b\left(E\right), \tag{6}$$

where a and b are functions depending on the properties of the traversed material. The a function describes the energy loss due to ionization, while b summarizes the contribution of all other processes, i.e. Bremsstrahlung, nuclear interactions and e^+e^- pair production. In the approximation that these slowly-varying functions are constant, the mean range $\overline{\varrho}_0$ $\left(\mathrm{g\,cm^{-2}}\right)$ of a muon with initial energy E_0 is given by

$$\overline{\varrho}_0 \approx \frac{1}{b} \ln\left(1 + \frac{E_0}{E_{\mu c}}\right), \tag{7}$$

where $E_{\mu c} = a/b$ is the "muon critical energy", i.e energy at which ionization and radiative losses are equal. Particle Data Group (PDG) provides

numerical values for a and b for a variety of materials and a wide range of energies.

Now it is possible to establish a relationship between mean range and intensity of penetrating cosmic-ray muons. Once that $\bar{\varrho}_0$ is given, the minimum energy E_μ^{min} required to penetrate through a given thickness can be extrapolated from PDG tables in continuous slowing down approximation (CSDA); integrating Eq. (1) from E_μ^{min} gives the expected muon flux $N_\mu(E_\mu^{min}, \theta)$. Figure 3 shows the penetrating muon flux at different zenith angles θ as a function of standard rock thickness, as defined in [37].

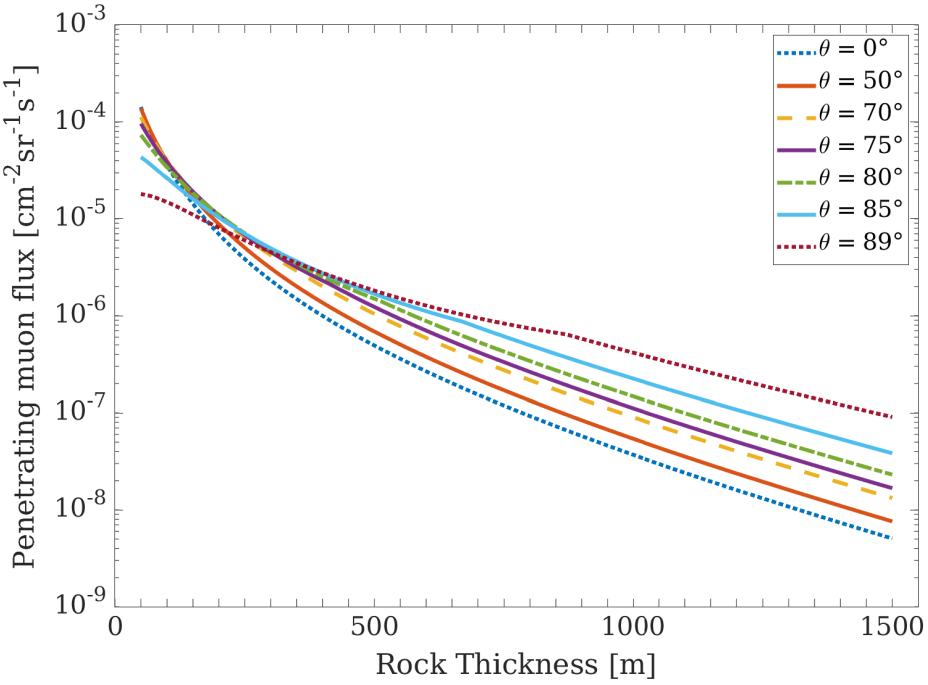

Figure 3: Muon intensity versus standard rock thickness. Plot is obtained by (i) fitting energy and CSDA range values from PDG table in [37] with Eq. (7) to get a and b and calculate E_{min} required to traverse a given thickness. This value is used for integrating Eq. (1) and retrieve the flux at certain depth. Calculation and plot were made with MATLAB.

The probability of a muon to cross a certain amount of matter depends on its initial energy and on the energy loss in traversing the medium. As shown in Fig. 2, getting closer to the horizontal, muon flux has a lower

mean intensity, but the number of particles with energy higher than few GeV increases. In order to inspect the inner part of geophysical-scale object, near horizontal muons are the best candidates because both flux and probability to pass the target are reasonably high (see Fig. 3). Measuring the fraction of muons passing through an object along different directions from a fixed point of view gives access to the target opacity integrated along these directions. If the traversed thickness through the object is known, opacity map can be transformed in density map.

This technique is usually referred as transmission muography, because the image appears while crossing muons add-up. Compared to deviation muography, transmission mode requires only one particle detection apparatus (commonly called *telescope*), which reconstructs muon trajectory in order to infer its path through the studied object. A fundamental assumption in this context is that muons follow a straight path traversing the object, i.e. Multiple Coulomb Scattering (MCS) can be neglected and the particle trajectory can be back-projected to reconstruct the linear path of muons inside the target, at least in first approximation.

Muon imaging application to volcanoes

The renewed interest in muon imaging originated in Japan for the application to volcanoes. The first proposal of studying the inner structure of a volcano using muons as a probe belongs to K. Nagamine in 1995 [38]. In 2003, H. Tanaka produced the first muon radiography of a volcano in which the structure of the central crater was recognized [39]. This experiment was the proof that muography can obtain results to complement measurements by micro-gravimetry and resistivity. Since that moment, many successful applications of muon imaging by Japanese group followed [40–43].

At the beginning of 2008, the collaboration between three French institutes (Institut de Physique du Globe de Paris, Institut de Physique Nucleaire de Lyon and Geosciences Rennes) initiated the DIAPHANE project to promote muon tomography in the French Earth Science and Particle Physics communities [44]. It was the first European project of muography applied to volcanoes. They performed an independent and original

development of the method after building several scintillator-based detectors and they set many theoretical limits for muon imaging, in particular the feasibility study formula to define the application domain of this analysis [45]. The French collaboration accomplished many long-term measurements in several volcanic sites (Italy, Philippines, Guadeloupe), including Etna [46, 47]. Later, they recognized for the first time, and corrected, that the density estimated with muography in some configurations is biased by the presence of an upward muon flux, entering the telescope from rear to front, which mimic the signal of downward going particles coming from the target [48].

In 2014 Tanaka team and DIAPHANE collaboration developed independently two different methods to join muon radiography and gravity data, showing the advantage in resolving small-scale density variations [11, 49]. In recent years, both groups showed evidence of integrated muon flux variations directly related to surface activities of theirs volcanoes, i.e. fumarole appearance and magma dynamics in the conduit, respectively. These results have reinforced the hope that in the future muon radiography can represent an alert system for potential eruption risk and not only an useful method to fully understand volcano structure and constrain hazard models.

The potential impact of muon imaging has led new emerging collaborations to build their telescopes and equip other volcanoes with muon instrumentation, often experimenting with techniques different from those previously used. TOMUVOL is a collaboration initiated in 2009, joining other three French laboratories. Its reference site is Puy de Dôme, an extinct volcanic dome near Clermont-Ferrand, France. They performed a muon radiography in 2013 [50] and a comparison between different technologies [51]. Subsequently they repeated the measurement at Puy de Dôme together, but as two independent experiments, with the MU-RAY collaboration and its telescope [52]. MU-RAY was the first Italian-based muon imaging project, started in 2010, and it involved researchers mainly from INFN - Naples division, and INGV - Osservatorio Vesuviano [53]. In 2012 they acquired first muon transmission data through Mount Vesuvio [54]. The experience acquired with the MU-RAY detector prototype represents the basis of the new MURAVES project, led by INGV and INFN and funded by the Italian Ministry of University and

Research (MIUR) [55].

In 2012, a Hungarian group from the Wigner Research Center (WRC) for Physics, Budapest, also started research on muon imaging. Initially, they focused on the development of portable detector for cosmic muon radiography of underground cavities [56, 57]. In recent years, the group from WRC and the Japanese group led by Tanaka started a collaboration and produced a muon radiography of the Sakurajima Volcano, Japan, with the highest resolution yet achieved [58].

Between 2011 and 2012 a muon transmission data tracking campaign was performed at Stromboli volcano, Italy, by a group of researchers including also people from some of the aforementioned collaborations. The results of this measurement were published only recently and displayed the first muographic image of this large strato-volcano [59].

Chapter 1

MEV muon-tracking detector

The cornerstone of every transmission muography experiment is a detector able to track particles inside its field of view (FOV), in such a way that it is possible to reconstruct their incoming direction and measure their flux. In the field of muon-radiography applications, such an apparatus is usually referred as muon *telescope*, independently of the charged particle detection technique it is based on. In order that the telescope works properly in transmission mode, it is necessary that no other macroscopic object lies behind the target so that it will remain the unique cause of muon flux attenuation.

It was already mentioned in the Introduction that the targets of muon imaging span from a pyramid to a volcano, passing through nuclear waste monitoring and glacier bedrock. As a consequence, the requirements of each telescope can be very specific and heterogeneous. However, some common characteristics may be found. Muography of large size objects is an out-of-laboratory experiment, so the detector need to be rugged and waterproof to face every climatic condition. Furthermore, the telescope could be placed far from a power network and, in this case, it is necessary to equip it with an independent power supply system, except if it employs nuclear emulsions to detect particles. Transmission muography usually deals with a very low or even tiny particle flux, that is an advantage from the point of view of the electronic data acquisition chain because it doesn't have to manage high signal rate. On the other hand, background noise can easily overcome muon signals and a strategy to prevent (e.g.

lead walls) or reject it (by time-of-flight measurement) is a crucial point.

This chapter will give a detailed description of the muon-tracking telescope designed and built for the MEV project. The detector construction was the main activity of the candidate during the first months of doctorate period. A brief overview of other detectors for muography of volcanoes is included for comparison. Before moving on, it is appropriate to clarify that there is not a unique detection technique for muon imaging applied to volcanoes or geophysical objects in general, and, at the same time, a solution that is better than the others in every aspect has not been found yet. Instead, it is possible to say that exists the best solution according to the main goal of the measurement.

1.1 Mechanical construction and power source

The first telescope developed for the MEV project was built at the Department of Physics and Astronomy of the University of Catania. The detector was designed to meet all the requirements of a long-term measurement campaign at the summit zone of the Etna Volcano. It is based on three X-Y position-sensitive (PS) planes, with a sensitive area of $1\,m^2$. The tracking modules are enclosed in a cubic box with external side of about 1.5 m, made with panels constituted by a double metallic cover and an inner isolating filling of polyurethane. A view of the open box, with the PS planes inside it, is shown in Figure 1.1. The external box has been tested to be watertight and working as a dark box.

Two solar panels (size: $150\,cm \times 80\,cm$; weight: 40 kg; peak power: 260 W; output voltage: 12 V) are mounted on the upper side of the box and charge two batteries (12 V, 205 A h; weight: 70 kg) housed inside the box. The box is mounted on a modular frame made with scaffolding pipes which facilitate the transportation of the structure using a truck with a mechanical arm. In this way it is possible to move the telescope already mounted to the measurement site. The weight of the box is about 300 kg. However, the internal aluminum structure which holds the PS planes is modular and can be assembled in field. Each sensitive module weighs less than 50 kg and can be carried by hand together with the electronics. For a short campaign during summer, the external box is not

Figure 1.1: Assembly phase of the telescope. It is possible to see the three sensitive planes fixed vertically on an aluminum frame to keep the alignment inside the external box.

necessary. The frame lies on adjustable legs to cope with uneven terrain. Figure 1.2 shows the telescope installed at the measurement site at about 3100 m a.s.l. at Etna North-East crater. The mechanical and power design of the detector makes it able to work out of the laboratory with no need of external power.

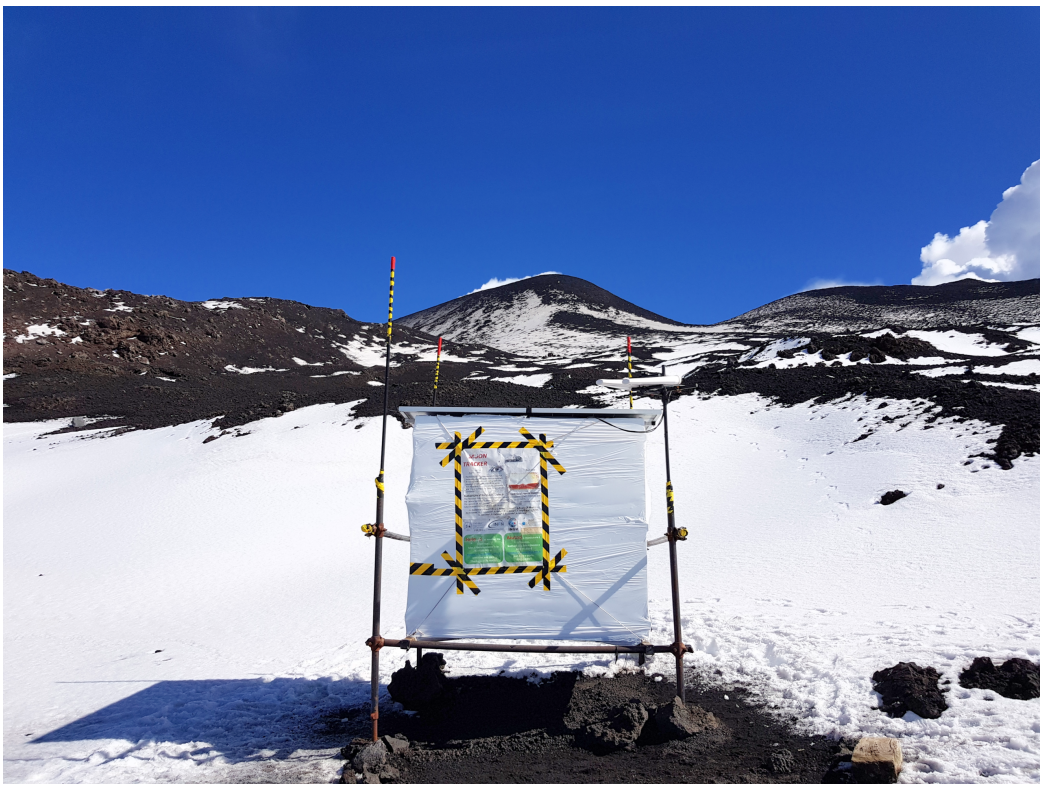

Figure 1.2: The telescope placed on the slope of Etna North-East crater in October 2018 during the second year of data taking campaign.

1.2 Tracking modules

The telescope can be thought as an imaginary parallelepiped where two PS planes are placed on two opposite faces and the third detection matrix lies parallel in the middle. Each sensitive module consists of two layers of 99 extruded plastic scintillator bars made by Fermilab [60] (nom-

inally $1 \times 1 \times 100$ cm^3) with a central 2.5 mm hole inside through which two 1 mm Wavelength Shifting (WLS) fibres (Saint-Gobain BCF-92) [61] are embedded to transport the photons to a multianode photomultiplier (MAPMT). The plastic scintillator is coated with a white reflector on each external side. Figure 1.3 shows some photos taken during the telescope assembly.

Each PS plane, therefore, is a matrix of $N \times N$ pixels, with $N = 99$. Let $f_{i,j}$ and $b_{k,l}$ be the pixels of front and back matrices, respectively, with i, j, k and l ranging from 1 to 99. The combination of all possible pixel pairs of outer matrices defines a set of $(2N-1)^2$ discrete directions of sight $\mathbf{r}_{m,n}$, with $m = i - k$, $n = j - l$. The direction $r_{0,0}$ is normal to the PS planes and is parallel to telescope axis, oriented from back (open-sky side) to front (target object side) and passing through its center. The total solid angle covered by the telescope and its angular resolution depend on the number of pixels, their size p and the distance D separating front and back matrices. Figure 1.4(a) shows the angular resolution $\delta\Omega(\mathbf{r}_{m,n})$ of MEV telescope with $p = 100/N$ cm and $D = 97$ cm. The angular aperture is about $\pm 45^\circ$ and the resolution does not exceed 4.3×10^{-4} sr, approximately. The detection area depends on number of pixel pairs which share the same direction and on p. The geometric characteristics of the telescope are summarized by the acceptance function $\mathcal{T}(\mathbf{r}_{m,n})$, given in cm^2 sr as defined in [45], and shown in Figure 1.4(b). The maximum acceptance, corresponding to the normal direction, reaches about 1.1 cm^2 sr. It must be specified that this value and the plot of theoretical acceptance (Fig. 1.4(b)) are referred to an ideal telescope having 100% detection efficiency. In fact, acceptance is modulated by the efficiency of each bar, which accounts for scintillation and light transportation efficiency in scintillating bars and WLS, photon detection efficiency (PDE) of the light sensor and, eventually, data acquisition (DAQ) chain performance.

1.2.1 Channel reduction system

Each PS plane, therefore, has $2 \times N$ intersecting strips and $4 \times N$ optical channels, one for each WLS. The number of corresponding front-end channels was minimized by means of a channel reduction system, already employed in other detectors, such as [35, 62], which is particularly conve-

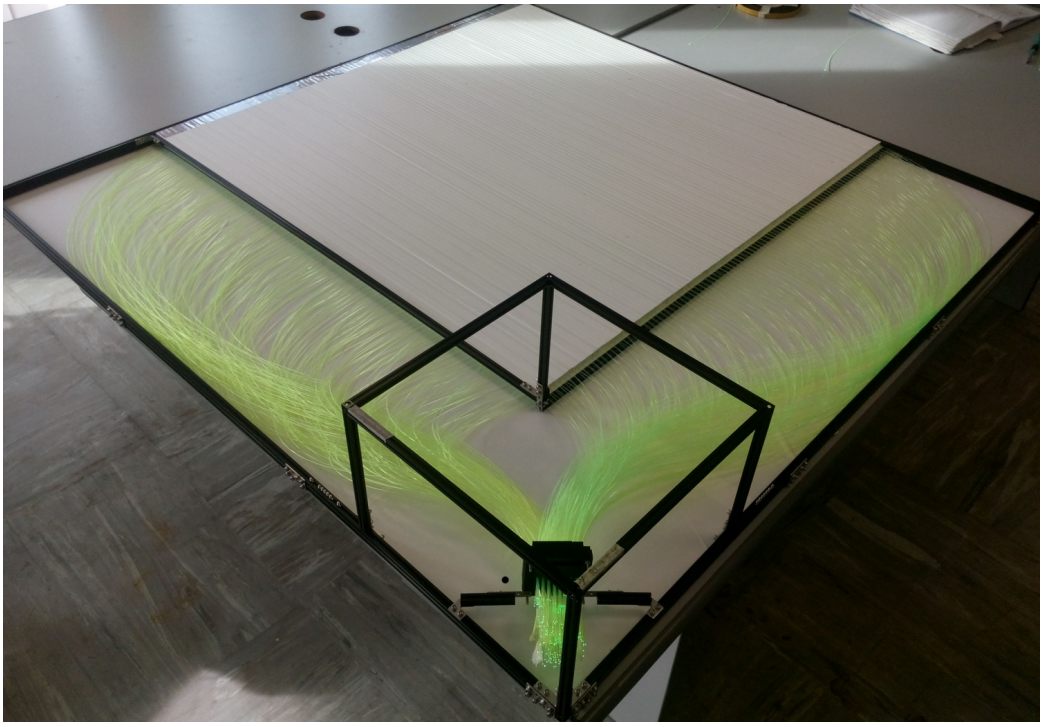

(a)

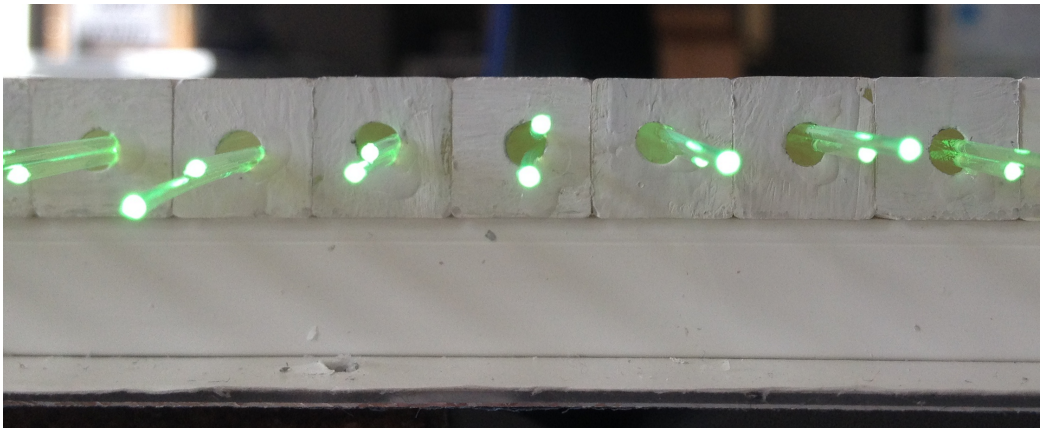

(b)

Figure 1.3: Assembly of a telescope sensitive plane. In 1.3(a) it is possible to see the two layers of extruded plastic scintillator bars of a plane enclosed in a frame of aluminum; 1.3(b) shows details of the two WLS fibres embedded inside each bar.

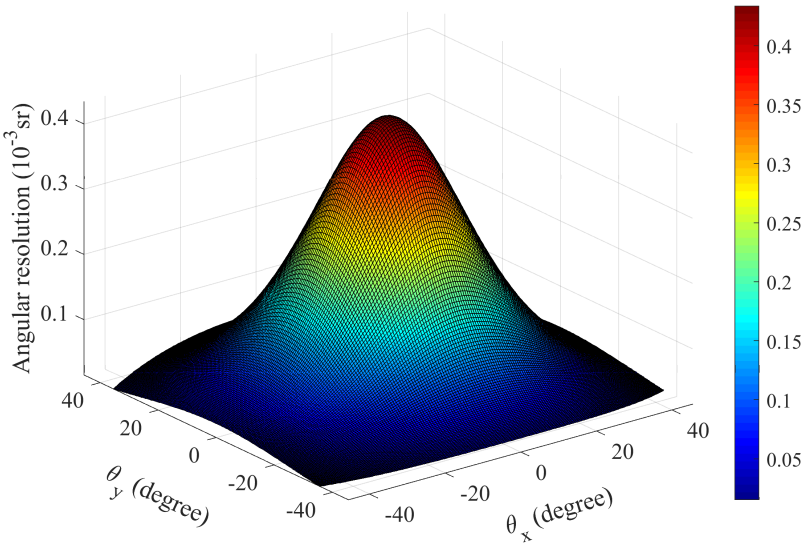

(a)

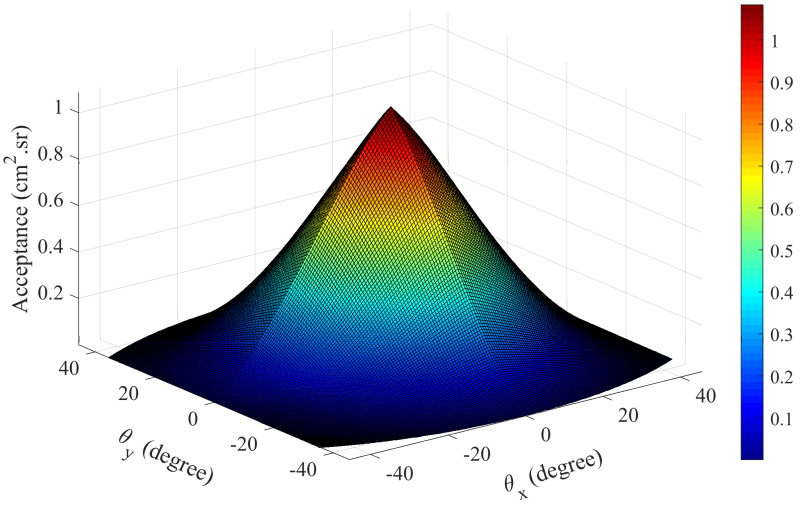

(b)

Figure 1.4: Distribution of the angular resolution $\delta\Omega$ (a) and the Acceptance $\mathcal{T}$ (b) for each discrete direction of sight of a telescope with three 99×99 matrices, $p \simeq 1.01\,\text{cm}$ and $D = 97\,\text{cm}$. Both quantities are displayed as functions of azimuth, θ_x, and zenith angle θ_y. The telescope axis corresponds to $\theta_x = 0$, $\theta_y = 0$. The drawings were obtained using the software MATLAB.

nient for tracking applications with high segmentation. Briefly, the two WLS fibers of each strip are differently routed: one WLS is coupled with those of the same *Group*-set, while the other one is coupled with fibers of the corresponding *Strip*-set, i.e. the *i-th* fiber for each *Group*-set. Figure 1.5 shows an example diagram of channel reduction system usage for a position sensitive module composed of 16 by 16 strips. In the MEV telescope each *Group* is composed by $n = 10$ strips, but this number can be adapted for the specific application. Combining the information of *Group*-set and *Strip*-set, the hit strip can be uniquely reconstructed, without any loss of information, and the required total number of readout channels is equal to 40 for each LP. The channel reduction system makes possible to couple the WLS fibers with a single 64 channel MAPMT, lowering the power consumption of the detector.

Equation 1.1 gives the crossing point of the particle depending on which *Group*-set and *Strip*-set are fired:

$$Strip_{hit} = (i - 1) \times n + j \tag{1.1}$$

where i corresponds to the i-th *Group*-set and j stands for the j-th *Strip*-set fired, respectively. This formula is valid when *Group*-set numbering starts from 1; if $i \geq 0$ the *Group*-set index does not need to be lowered by one unit.

1.3 Front-End and Read-Out electronics

The electronic chain is fully custom-designed for the purpose of MEV project in order to have low power consumption. It can be divided in two main parts, the Front-End (FE) and the Read-Out (RO) electronics. The FE consists of three boards, one for each PS module. Each FE board houses a Hamamatsu H8500 MAPMT with 64 channels [63] and a MAROC3 chip [64]. In the pre-processing phase, the chip pre-amplifies and shapes the analog signal from the MAPMT with a peak time of about 20 ns and compares all the signals to a common threshold, giving a digital time-over threshold signal for each channel. A photo of a FE board is shown in figure 1.6(a). At the time when the telescope was built and in sight of the final measurement site on the top of Etna volcano, MAPMT, due to

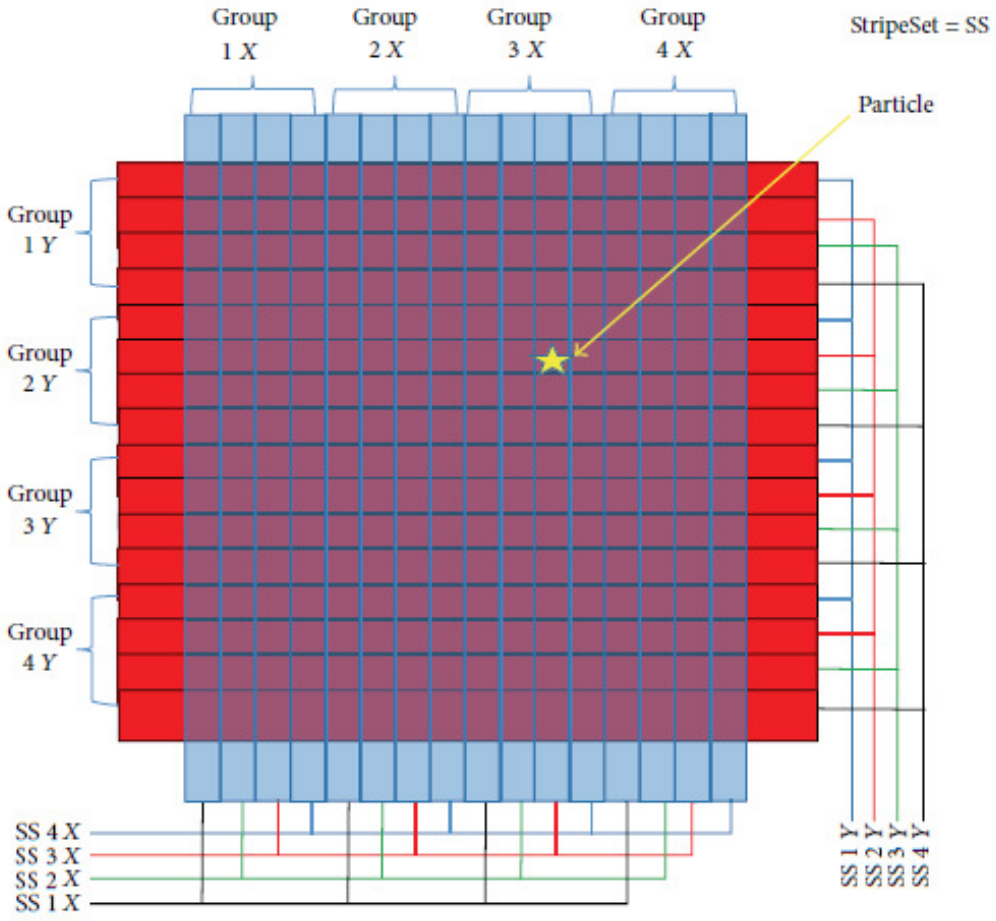

Figure 1.5: Diagram of the channel reduction system for a strip based position sensitive detector. The star represents the crossing point of a particle in the sensitive area.

its very low dark current rate, was a preferable choice respect to silicon-photomultiplier (SiPM). However, also the latest generation of SiPM has a very low dark current which makes it a good option for this kind of application. Nevertheless, for an usage at high altitude, as it is intended for the MEV telescope, a temperature compensating power supply must be included to take into account high daily and seasonal temperature fluctuations and keep the sensors operating point constant.

The output from each FE board is then acquired, filtered and processed by a National Instrument SOM (System-on-Module) [65] mounted on a single RO board (see Fig. 1.6(b)), which also houses the sensing components for temperature and movement (accelerometer). A scheme of the complete electronic chain is sketched in figure 1.7. The SOM allows a graphical approach for programming its FPGA with LabVIEW. A dedicated User Interface (UI) has been developed to manage and control all the parameters of the system.

Data are stored in a local SD card memory. The acquisition chain is set to write a bunch of data in a separate file every 5 minutes (ten during 2017 campaigns). The system is equipped with a 4G LTE wireless router. When the network signal is available, the data are sent to a cloud storage at the Department of Physics at a rate depending on signal strength.

At the end of summer 2018, before interruption of the second year of data acquisition campaign, a module to measure particles time of flight (TOF) between the external tracking planes was installed. It consists of an additional electronics board which is used after a delay line driver, monostable and digital level translator for the OR signal output of MAROC3 chips in the FE boards; the monostable, when triggered, remains in a stable high state for a period of 250 ns. In the end, the output of the three aforementioned mentioned circuits, suitably delayed, are sent to a time-to-digital converter (TDC) with picosecond resolution [66].

The purpose of this measurement is the correct discrimination of near-horizontal tracks. As will be evident in the following discussing the results, muography experiments applied to very large structure deals with very tiny muon flux and in order to retrieve density variations inside the target we search for fluctuation of this flux. This means that even little noise source can overcome signal of muons which passed through the target. A main source of noise comes from multiple particles which si-

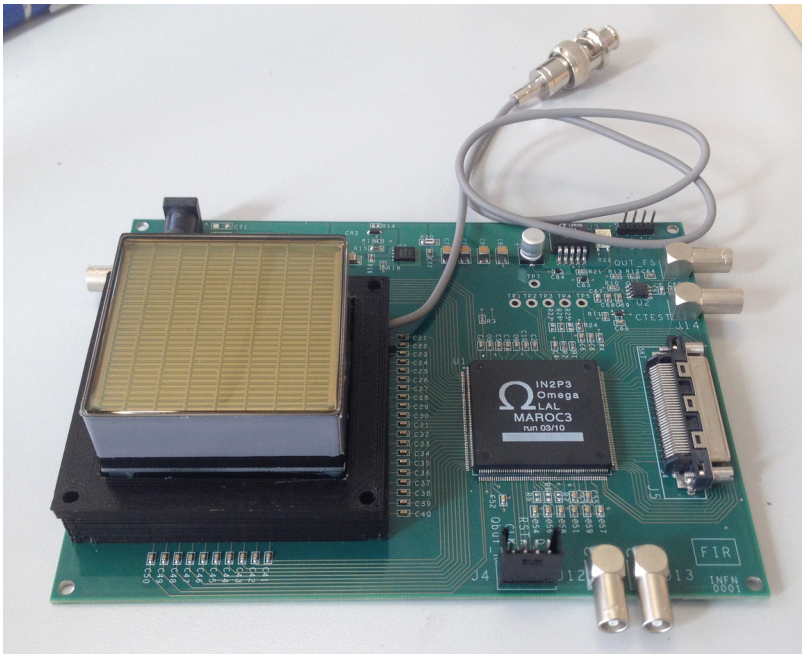

(a)

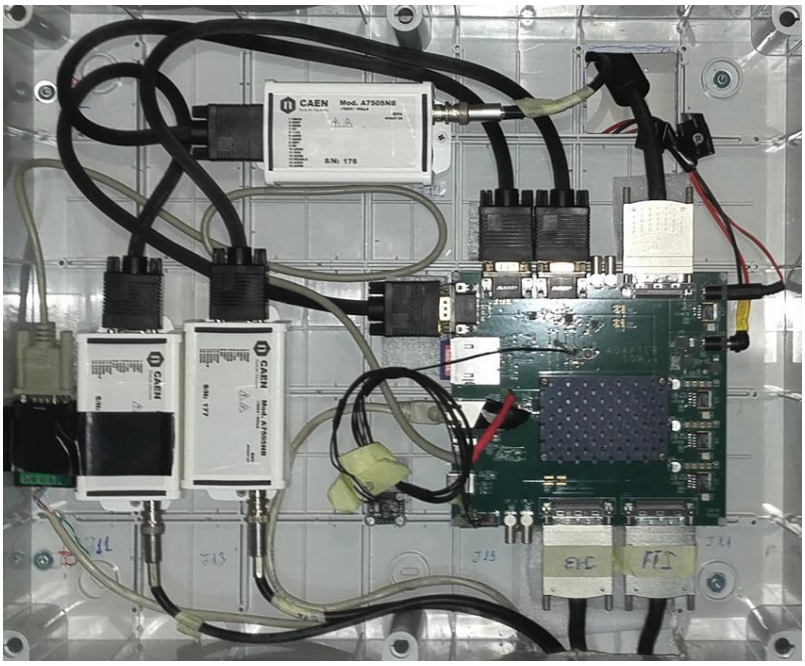

(b)

Figure 1.6: (a) A front-end (FE) board equipped with a Hamamatsu H8500 64 channel MAPMT. (b) A photo of the read-out (RO) board placed inside a plastic box with the modules for MAPMTs power supply.

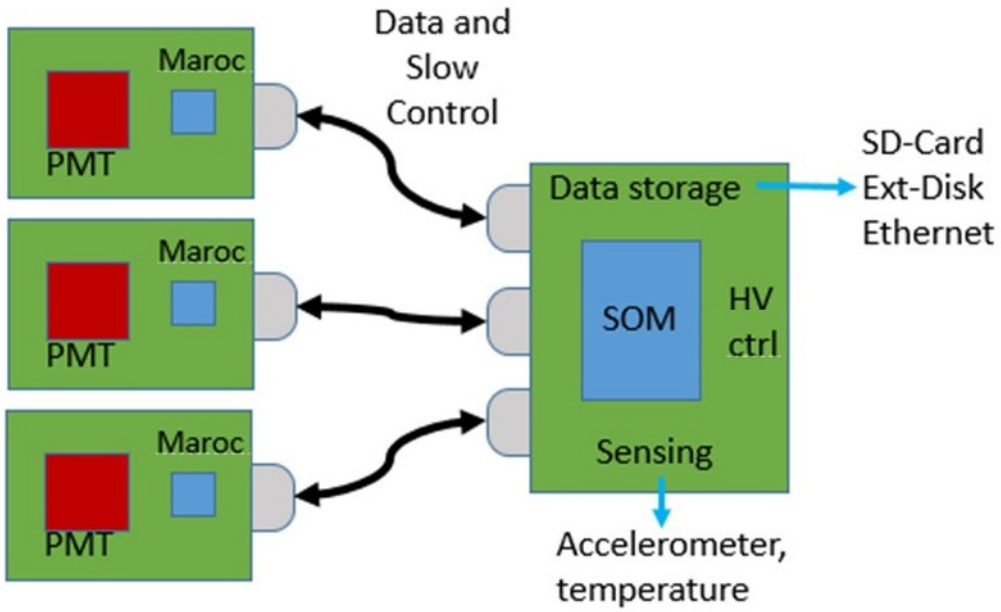

Figure 1.7: Diagram of the electronic chain of the telescope.

multaneously hit the telescope tracking modules and could be wrongly reconstructed as the track of a unique particle traversing the whole detector. As discussed in [36], this phenomenon can be almost completely avoided by using at least three detection planes spatially apart, as we did. Another source of noise that pollutes data especially in the region near horizontal direction, i.e. at angles at which the muon flux is further reduced, comes from upward muon flux. It deals with muons which seems to come from below the horizontal plane before passing through the telescope, so that they perfectly mimic particles which come downwards in the opposite direction. If such an event passes successfully all geometric conditions to reject background noise, it will be indistinguishable from a downward muon event and it will produce a wrong increase of flux measured. In order to remove this noise, it is required a non-geometric criterion to distinguish particles coming from the front of the detector from those which enter it from back side. A possible solution is a time-of-flight (TOF) measurement between telescope extreme planes.

The power consumption of the whole telescope is about 25 W, includ-

ing the data transmission system and TDC.

1.4 Signal processing and data acquisition

The MAROC3 chip compares each pre-processed signal per channel (i.e. after pre-amplification and shaping) to a remotely settable threshold, producing at its output an encoded digital representation of the detector response to the passage of a particle. A periodic calibration procedure is included in order to adjust the gain of each channel and compensate MAPMT non uniformity, by means of an 8-bit coded variable gain preamplifier, in such a way that dark current signal rate is roughly the same for the whole light sensor. While the gain of each pixel may differ, the dark rate is related mainly to the photocathode which is made as uniform as possible by the manufacturer.

Another advantage of the channel reduction system is that it makes possible to use a single SOM and, in this manner, the synchronization of the data coming from each FE board is ensured. The SOM simultaneously samples at 200 MHz all 120 channels, corresponding to the response of all three planes of the detector.

A crucial point for data acquisition strategy is the trigger condition to start the record of an event. During the initial test phase, a not-too strict trigger condition was chosen in order to fully understand the detector response, postponing the track recognition in the offline analysis. In particular, the acquisition of an event was triggered when two *Group*-set, one for each coordinate, have a high signal (greater than threshold) in at least two PS modules within a time coincidence window of 80 ns. This condition determines a trigger rate of about 100 Hz which produces a binary file of about 10 MB for ten minutes of acquisition. The SOM can easily handle a signal rate of the order of kHz, it was established to not change the trigger condition after the test phase and it has remained the same until the end of the first measurement campaign at Etna North-East crater (summer 2017).

The introduction of TDC module has required some modifications in MAROC3 chip operating mode. In order to achieve the best time resolution, the bipolar fast shaper chain was chosen, which has lower signal

rise time respect to unipolar fast shaper chain. However, this operating mode reduces the amplitude of the signal in such a way that the MAROC3 threshold can be adjusted within a limited range. Considering that MAX961 fast comparator and monostable in the TDC chain have a measured propagation-delay time jitter of 0.3 ns, typical transit-time spread (tts) of Hamamatsu H8500 MAPMT is equal to 0.4 ns, trapping and re-emission time spread together with different light path lengths along WLS fibers produce an estimated light propagation time jitter of about 0.8 ns at most and including time resolution of TDC and MAROC3 chips, the nominal time resolution per channel of the TOF module is estimated as:

$$\sigma_t = \sqrt{\Delta t_{FC}^2 + \Delta t_{MAPMT}^2 + \Delta t_{WLS}^2 + \sigma_{t,MAROC3}^2 + \sigma_{t,TDC}^2} \simeq 1\,\text{ns}. \quad (1.2)$$

Because the TOF is intended to measure the time difference between the crossing instant of particle in telescope external planes, the real time resolution $\sigma_{\Delta t}$ must be multiplied by a factor $\sqrt{2}$. Table 1.1 resumes all contributions to σ_t with the corresponding symbols used in Eq. (1.2).

Component	Time jitter
MAX961 fast comparator & monostable (Δt_{FC})	0.3 ns (measured)
Hamamatsu H8500 MAPMT tts (Δt_{MAPMT})	0.4 ns (declared)
WLS light path induced time jitter (Δt_{WLS})	0.8 ns (measured)
MAROC3 chip time resolution ($\sigma_{t,MAROC3}$)	0.4 ns (measured)
TDC-GPX2 time resolution ($\sigma_{t,TDC}$)	20 ps (declared)

Table 1.1: Contributions to TOF module time resolution. MAX961 fast comparator, monostable and MAROC3 chip time resolutions were measured in our laboratory; for a detailed description on WLS time jitter estimation see ref. [67].

The trigger condition has remained the same during 2018 acquisition campaign, but after the introduction of TDC module some issue arose. In particular, trigger rate resulted too high to guarantee the synchronization between tracking and timing data. Hence, from the beginning of the

data acquisition campaign of 2019 the condition to start the record of an event become more stringent and requires a high signal from at least two *Group*-set, always one for each coordinate, in all three planes. The tracking efficiency is not reduced by the new trigger condition because, as will be extensively explained in the next chapter, only particles tracks reconstructed from three points, one for each tracking module, have to be considered in order to avoid including spurious coincidences.

1.5 Muon detection systems for volcanoes

Last section of this chapter is an overview on other detection mechanisms used for transmission muography of big size objects such as a volcano. In introducing the description of MEV telescope, some of the common features of this kind of detectors have been already cited (rugged construction, independent power supply and electronics for low signal rate). Another characteristic shared by all detectors under discussion is their size. They are essentially constituted by a series of position sensitive elements with an active area of the order of one square meter. Anyway, their size is much more little respect to the object they scan, so that the detectors could be considered as a point respect to the target. In addition, all muon telescopes do not have the ability to measure the momentum of each particle and, besides muons, they are sensitive to all other charged particles.

Muography application to volcanoes is based on tracking, so every detector designed for this purpose have at least two position sensitive modules, at a certain distance between each other, able to reconstruct the crossing point of the particle in order to retrieve its trajectory. Here it is possible to find the main feature that distinguish a muon telescope from another, i.e. the physical principle for particle detection. A muon telescope could be based on scintillation or nuclear emulsion sensitive modules or gaseous detector.

Since the renaissance of muon-radiography experiments by Japanese research group, plastic scintillators have represented the best compromise for these applications. They allow to construct robust detectors which require not much maintenance of the sensitive components and can be eas-

ily read out by means of PMTs or, even more conveniently, with SiPMs as discussed before, with a not too high number of channel required. Power consumption, which includes light sensitive sensors and electronics power supply, is not critical for this kind of detector and, hence, they have all required characteristics to operate in harsh environments. On the contrary, some issue could rise from the light sensors which performance is very influenced by temperature variations in the case of SiPMs.

Plastic scintillators layout is highly customizable and, in fact, it is possible to find muon telescopes which employ square, rectangular [46, 68] or triangular section scintillator bars [54] arranged to constitute a position sensitive module. Shape, disposition and size of each module determine the spatial resolution on position measurement and the required algorithm to reconstruct it. Fixed X-Y spatial resolution, angular resolution depends mainly on the distance between the two external tracking modules. Increasing this space allows to restrict the telescope field of view on the target object, but at the same time lowers detector solid angle of view and the muon flux intensity that can be tracked in the same time interval. These considerations about angular resolution regard all telescope based on multiple independent tracking planes.

Nuclear emulsions represent actually the best technology from the point of view of spatial resolution which is roughly equal to the grain size, i.e. of the order of microns. A muon telescope based on nuclear emulsion can be very compact because its very high spatial resolution allows to place many tracking modules at a short distance between each other [59]. This detection technique is completely passive, i.e. it not needs power supply and electronics. In fact, nuclear emulsion foils must be analyzed at the end of the measurement by an optical system. Here the drawbacks of this technology come out: the time information is completely inaccessible and the plates can not be power on or off at the beginning or at the end of the measurement, respectively. So, they should be assembled just before to start the measure and read immediately after the end. All tracks recorded in the meanwhile, despite any possible shielding, may not be distinguished from those acquired during the measurement. In conclusion, nuclear emulsions are well suited only for not-dynamic objects. A very successful application of nuclear emulsion, combined with other techniques, is the already cited muon-radiography of Great Pyramid in

Giza, Egypt, by the ScanPyramids project [5].

Gaseous detectors represent a very well suited solution for applications where angular resolution is a key-parameter. A gaseous tracking module can be realized with different techniques, such as close cathode chambers, multi-wire proportional chambers or drift chambers, all based on the same principle of collecting, by means of an electric field, electrons and ions generated by a charged particle along its trajectory within the gas volume. Whatever it is the technology, resolution up to 100 microns is easily achievable. Successful examples of gaseous detectors application for muography are the studies on Puy De Dome complex, France [50], and Sakurajima volcano, Japan [58], but despite many advantages, which include relatively simple construction and electronics, there are also some issue that become even more crucial for experiments outside of a controlled room. A continuous gas flux is often required, that means a system whit power supply and many gas bottles for refill, in particular for detectors of large area. In addition some mixtures include explosive gases that pose strict security limits. The performances are strongly dependent on the precise control of the applied electric field and, briefly, it is possible to say that gaseous detectors need to be constantly monitored. These features are not very well suited for experiments in a hostile and accessible site.

Another characteristic which allows to classify muon telescopes is the presence of a background rejection system. Low energy muons, electrons and protons are the main source of background noise for muography, especially in the case study of large size object that absorb the major part of cosmic muon flux which impinges on them. A validated solution to overcome this issue consists in one or more lead walls with a suitable thickness in order to stop background particles before reaching at least one sensitive module. This solution, however, has the drawback of introducing additional scattering centers for high energy muons and could deflect them while traversing the detector. When adopting lead wall shielding, it is necessary that the telescope has a high tracking resolution to recognize deflections which happen inside the detector and avoid to reject good muon tracks also. It is estimated that a suitable energy cut for muography of volcanoes is of the order of 5 GeV and it requires tons of lead. Besides being expensive, this solution sets important constraints to the

mechanical design of the detector.

Considering the relatively small size of a muon telescope and that particle to be tracked have a relativistic factor β very near to 1, a TOF measurement is not very useful for an energy cut. However, it is appropriate to distinguish the incoming direction of near horizontal particles. In conclusion, these two technique are complementary one to another.

Chapter 2

Event reconstruction methods

The core of the PhD activity concerns the research about events reconstruction methods directed towards the most significant muon imaging reconstruction. Several strategies have been explored by investigating the relation between constraints on acceptable data and number of retrieved particle tracks. The code by means of which data bit-stream is converted into spatial information of the interaction points of particles in the sensitive tracking modules was implemented from scratch in MATLAB language and, also, in C++ to speed-up calculation of heavier tasks. The same also applies to the code user for data clustering, when needed, and to compute the trajectory of each particle. Data plots are mainly made with MATLAB. In the following, in order to keep the text clear and readable without getting lost in code syntax, the workflow of the procedures defined is written as generic pseudo-code.

2.1 Signal height filtering

First of all, in the off-line analysis, data sent by the telescope are filtered according to the pulse signal height. The reader should remember from the previous chapter that data were digitized by MAROC3 chip. Then, the offline analysis is performed on bit-stream of digital data. As a consequence of digitization, the original height translates into number of clock cycle with an high bit, i.e. a representation of time-over-threshold (ToT).

Before going deeper in describing this first stage of data analysis and to better understand what in the following, it is necessary to give the details of position data structure produced by the telescope acquisition system.

Data sent by the telescope to cloud storage hosted at Department of Physics and Astronomy in Catania consist of binary files which contain a header of two 32-bit integers, respectively, number of rows N_r and columns N_c in the file, followed by a $N_r \times N_c$ array of 64-bit words. N_c is equal to the number of tracking modules, i.e. $N_c = 3$, while N_r is related to how many events were registered during a data acquisition time window for every file (five or ten minutes). At each clock cycle (i.e. every 5 ns) three 64-bit sequences are written in a row of the file, describing the output of each MAROC3 chip. A 64-bit sequence can be decomposed in:

- 10-bit corresponding to the state of *Group*-set X;
- 10-bit corresponding to the state of *Strip*-set X;
- 12-bit empty (equal to 0 - low state);
- 10-bit corresponding to the state of *Group*-set Y;
- 10-bit corresponding to the state of *Strip*-set Y;
- 12-bit unsigned integer (evID).

The value of evID is a progressive event counter which resets its value to zero every $2^{12} (= 4096)$ events. Because the time coincidence window was set equal to 80 ns, the record of an event consists of 16 consecutive rows in the file, which have the same event counter value, in fact. An example of the bit-stream corresponding to the *Group*-set X data recorded for an event is reported in Table 2.1. For the same bit-index, i.e. along a column, the number of high states is proportional to ToT of the starting analogue signal.

In reducing the 16 lines recorded for a single event, it is possible to introduce a threshold for signal height, setting a lower limit for the minimum number of clock cycle at which a signal over threshold was sampled. In order to prevent the contamination by electronic noise (bit-flipping), a minimum number of two consecutive clock cycles with a registered high state is required in order to evaluate the corresponding channel fired. The

result of this first analysis step is reported in the last row of Table 2.1 and corresponds to the logical AND operation ($\wedge$) performed along each column of the table which contains the minimum required number of high values.

The algorithm in Pseudo-code 1 resumes the method just exposed for event synthesis from data stream, with signal height filtering.

Pseudo-code 1: Algorithm for event synthesis with signal height filtering.

Input: *bitset*64$[N, 3]$
1 **for** *i=0; i<N; i=+16* **do**
2 **foreach** *bitset64* **do**
3 disperse into:
  – group-x of class *bitset*10;
  – strip-x of class *bitset*10;
  – empty-value of class *bitset*12;
  – group-y of class *bitset*10;
  – strip-y of class *bitset*10;
  – evID of class *bitset*12;
4 **end**
  Output: a matrix with 16 rows for each variable.
5 **foreach** *matrix column* **do**
6 **if** *sum(column) > minN_high* **then**
  Output: $\wedge$ along column;
7 **else**
  Output: 0;
8 **end**
9 **end**
10 **end**
Result: *Group*-set X$[N/16, 3]$, *Strip*-set X$[N/16, 3]$, *Group*-set Y$[N/16, 3]$, *Strip*-set Y$[N/16, 3]$, evID$[N/16, 3]$.

The output of first analysis stage are stored in three files per day, one for each tracking module, which consist of four columns, *Group*- and *Strip*-set for both X and Y coordinates, and a number of lines equal to the number of detected events.

Group-set X

0	1	2	3	4	5	6	7	8	9
0	0	0	0	0	0	1	0	0	0
0	0	0	0	0	0	0	0	0	0
0	0	0	0	0	0	0	0	0	0
0	0	0	0	0	0	0	0	0	0
0	0	0	0	0	0	0	0	0	0
0	0	0	0	0	0	0	0	0	0
0	1	0	0	0	0	0	0	0	0
0	1	0	0	0	0	0	0	0	0
0	1	1	0	0	0	0	0	0	0
0	1	1	0	0	0	0	0	0	0
0	1	1	0	0	0	0	0	0	0
0	0	1	0	0	0	0	0	0	0
0	0	1	0	0	0	0	0	0	0
0	0	1	0	0	0	0	0	0	0
0	0	1	0	0	0	0	0	0	0
0	0	1	0	0	0	0	0	0	0
0	1	1	0	0	0	0	0	0	0

Table 2.1: Example of bitstream data within an event (16 lines) only for *Group*-set X. First alphanumeric row represents the bit-indexes; last row reports the results of the $\wedge$ (logical AND) operation performed along each column, taking into account the lower threshold for high states number to consider the corresponding channel as fired.

2.2 Track reconstruction

The content of the files produced at the end of first offline analysis stage represents the input argument to particle impact point reconstruction method. It is based on Equation 1.1 for decoding the channels reduction system information into particle impact point coordinate.

Before going ahead, it is useful to classify the results of coordinates reconstruction procedure into three categories:

a) no X[Y] retrieved: this happens when no group- and/or no strip-channel has a high bit for a coordinate;

b) *single-hit*, i.e. a unique X[Y] reconstructed, that is the result produced when a single bit is high in both *Group*- and *Strip*-set for the evaluated coordinate;

c) *multiple-hit*, i.e. more than one X[Y] reconstructed, that are the outcome of multiple high bits in *Group*- and/or *Strip*-set.

The output of position reconstruction method can be of type (a) because the trigger condition required for the acquisition of an event requires that at least two *Group*-set (or three from 2019) have a high signal, while no condition is set on number of *Strip*-set with a high state. In addition, signal height filtering procedure can switch off group- and/or strip channel which does not satisfy it.

Extending the position reconstruction to all tracking modules, for each event it is possible to have:

A) no track retrievable when condition (a) happens for at least one coordinate in a sensitive plane;

B) a single-hit for all six coordinates (X-Y for three tracking modules);

C) at least one multiple-hit for the same event, produced by condition (c) for one or more coordinates.

In case A, the event is discarded; in case B, the three X-Y point coordinates are ready to be passed as input for the next step of the analysis, i.e. alignment check by means a of 3D linear fit; case C opens more then

one strategy for the reduction of all possible combinations between single point for every plane. In particular, a clustering procedure is introduced in order to group reconstructed points in each tracking module in order to compress the information on every point group to the coordinate of its centre. The adopted clustering procedure is described right now.

2.2.1 Data clustering

The word *clustering* refers to a machine learning technique for the partition of data points into groups. Usually, data points are assigned to a specific group according to some common features which distinguish them from the points belonging to other groups.

For the problem under consideration a slightly modified version of the Density-Based Spatial Clustering of Application with Noise (DBSCAN) was implemented. Standard DBSCAN method proceeds through the following steps:

1. The search for a cluster begins with an arbitrary point that has not been already visited. The distance between this point and the others is calculated and the neighbours within a distance ε are extracted.

2. If there are a sufficient number of point in neighbourhood, according to an established parameter `minPoints`, the starting data point is assigned to a new cluster and the procedure to identify the other points of the same cluster begins. Otherwise, the starting point is labelled as noise. In either case the it is marked as "visited".

3. Points within distance ε from the first point also become part of the same cluster. The procedure of grouping all points within distance ε into the same cluster is repeated for all the new points just included in the group.

4. The procedure of step 2 and 3 is repeated until all the points belonging to the cluster are labelled, i.e. all the points that have at least `minPoints` neighbours within distance ε have been retrieved and marked as visited.

5. Once that no other point can be assigned to the cluster, the procedure is ready to start again from step 1. This process repeats until all data points are labelled as visited and assigned to a cluster or marked as noise.

In order to understand the modifications introduced with respect to standard DBSCAN method, it is convenient to imagine which can be the result of a charged particle interacting with the scintillating bars of a X-Y tracking module such that included in the MEV telescope. The simplest scenario is when a single bar for each coordinate was hit by the particle and position reconstruction procedure outcome is of kind (b). On the other hand, the telescope geometry makes possible that particles entering the detector tilted respect to its axis can cross two adjacent bars in one or both directions. If struck bars belong to the same *Group*-set, the result is a single high bit for the *Group*-set and two high bits for the Strip-set in X and/or Y. Combining the reconstructed impact points, we expect a cluster with size equal to 2×1 or 2×2 strips, at most. The maximum distance within points of this cluster is equal to $\sqrt{p}$, where p is the width of a scintillating bar, as defined in Chapter 1.

The worst scenario is when a particle hit the tracking module at the intersection between two adjacent *Group*-set in both direction: in this case the results is two contiguous high bits in the *Group*-set and two high bits in the *Strip*-set, i.e. bit 0 and bit 9. Applying the position reconstruction procedure to this case and referring to Equation 1.1, we have i and $(i+1)$ for the *Group*-set indices and $j = 0, 9$ for the *Strip*-set indices, which correspond to:

$$Strip_{hit} = \begin{cases} i \times n \\ i \times n + 9 \\ (i+1) \times n \\ (i+1) \times n + 9 \end{cases} \tag{2.1}$$

where n is the number of strips belonging to the same *Group*-set. If the same scenario is valid for both coordinates, the results are four X and four Y strips hit that, coupled to retrieve the possible impact points gives 16 combinations. An example of such a case is shown in Figure 2.1, with $i = 1$. It is clear that, only one cluster correspond to the real particle impact point, i.e. the central cluster with size 2×2.

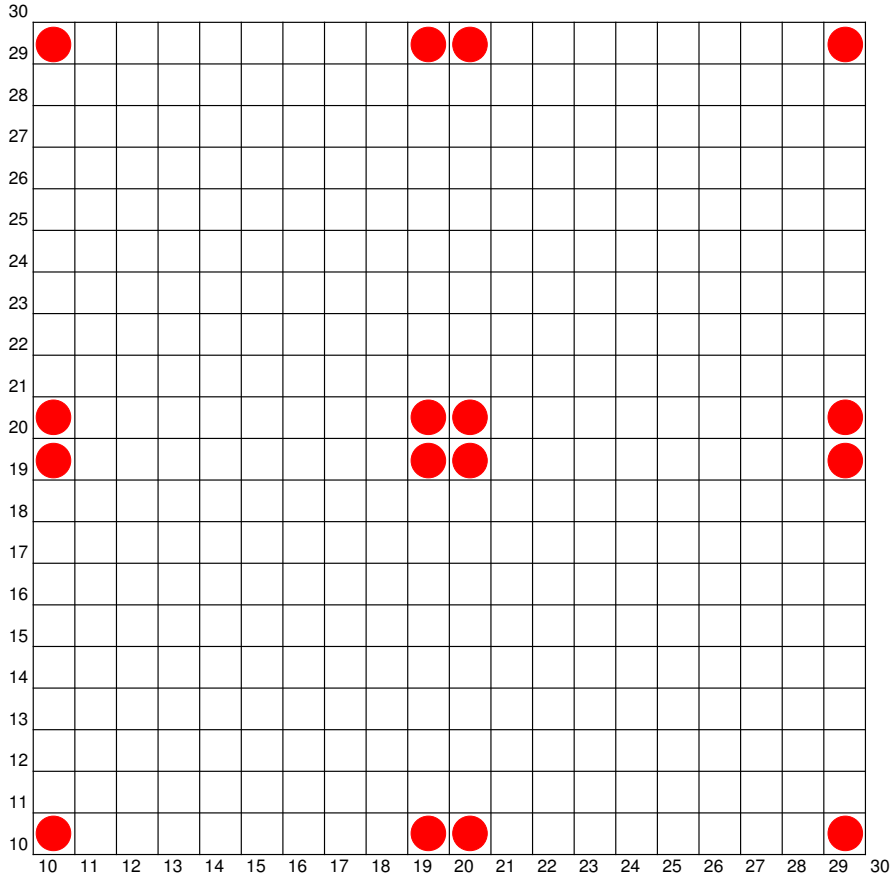

Figure 2.1: Drawing of the data point reconstructed for a tracking module when a particle hit two adjacent group in both coordinate. In this example *Group*-set indices $i = (1, 2)$, with numbering starting from 0.

In any case, now it should be clear that, for the problem of point grouping for MEV telescope data, it is required a threshold for the maximum number of points belonging to the same cluster, i.e. `maxPoints` $= 2 \times 2$, while a single point without any other point in its neighbourhood is also a cluster produced by scenario (b) for both coordinates. Instead, if the modified DBSCAN algorithm find a cluster with size greater than `maxPoints`, it will be labelled as noise. The complete modified DBSCAN procedure is reported in Pseudo-code 2.

Once point clustering procedure is completed, a list of data point

Pseudo-code 2: Modified DBSCAN procedure.

```
   Input: datapoints
1  while there is a non-visited data point do
2  |  find ramdomly a non-visited data point;
3  |  calculate distance between this point and the others;
4  |  extract neighbours within distance ε from the starting point;
5  |  foreach neighbours do
6  |  |  if is not visited then
7  |  |  |  mark it as visited;
8  |  |  end
9  |  |  add it to current cluster;
10 |  |  calculate distance within this neighbour and other
   |  |   points;
11 |  |  if there are points within ε then
12 |  |  |  add them to neighbours;
13 |  |  end
14 |  end
15 |  if cluster size > maxPoints then
16 |  |  mark this cluster as noise.
17 |  end
18 end
   Result: list of clusters with corresponding noise marker.
```

groups is obtained with corresponding noise/not-noise labels. For clusters not marked as noise, it is possible to calculate X-Y coordinates of the cluster centre which will be passed to the next stage of track reconstruction procedure.

2.2.2 Particle trajectory reconstruction

At this stage of track reconstruction, it is possible to have a unique combination of points, i.e. one point for each plane, or a set of combinations given by the Cartesian product between the point-sets retrieved for each tracking module, i.e. T_1, T_3, T_2, respectively:

$$\begin{gathered} T_1 \times T_3 \times T_2 := \\ \{((x_1, y_1, z_1), (x_3, y_3, z_3), (x_2, y_2, z_2)) : (x_i, y_i, z_i) \in T_i \; \forall i = 1, 3, 2\}. \end{gathered} \tag{2.2}$$

In previous equation the coordinate z is introduced for first time; if $\hat{x}$ and $\hat{y}$ are the unit vectors which represent the spatial directions on a tracking module, $\hat{z}$ is the remaining component of the orthonormal basis that defines a Cartesian coordinate reference system, with $\hat{z}$ aligned along the telescope axis. Furthermore, the order in which the tracking module are cited is not accidental, but corresponds to the real plane arrangement inside the telescope box, with the module labelled *T3* in middle. The goal of this last step of analysis procedure is to check if a point combination is aligned along a line, so that it is possible to get back to trajectory of the corresponding particle.

The 3D linear-fit procedure implemented always allows to retrieve the best-fit line corresponding to every point combination. Then, it is possible to establish if the points are aligned in space according to a condition related to the distance within each point and the best-fit line. In the scenario C, i.e. when point reconstruction procedure has retrieved more points for al least one T_i, a different best-fit line corresponds to each combination computed by Eq. 2.2. Among retrieved lines, the method search for the one with the smallest sum of squared residuals and, if it also satisfies the alignment condition, it is admitted as a good event track.

The method implemented for 3D linear fit is based on Principal Component Analysis (PCA), a dimensionality-reduction method used to lower the dimensionality of large data sets $\{A\}$. This means that a p-dimensional

space, where p is the number of variables which describe the data set, is reduced to a smaller one, i.e. a k-dimensional data set, with $k < p$, while preserving as much information as possible. In fact, lowering the number of variable data set usually comes at the expense of accuracy, but smaller data set are easier to explore and faster to analyse. If we have a series of n observations, original data set A can be arranged as a matrix $n \times p$; with regard to the problem of 3D linear fit, $n = 3$ because the data set consists of three observation, i.e. one point for each plane, and $p = 3$ because each point is described by three variables (x, y, z). Here is a step by step explanation of PCA, leaving aside involved mathematical formalism.

1. Standardization: prior to starting, it is critical to perform standardization of the data set because PCA is quite sensitive to the variances of initial variables. Standardization is the process of transforming data set in order to have zero mean and unit variance. Mathematically, this can be done by subtracting the mean (μ) and dividing every value by the corresponding variable standard deviation (σ):

$$\{A_m\} = \frac{(x_i, y_i, z_i) - (\mu_x, \mu_y, \mu_z)}{(\sigma_x, \sigma_y, \sigma_z)} \tag{2.3}$$

   where $\{A_m\}$ is the data set after standardization.

2. Covariance matrix computation: this step allows to understand if there is any relationship among variables within the input data set. In particular, the key parameter is the sign of covariance because, if it positive, this means that two variables increase or decrease together, while if covariance is negative one increases when the other decrease and vice versa (inversely correlated).

3. Compute eigenvectors and eigenvalues of the covariance matrix and identify principal components. In order to understand why we need to calculate eigenvectors and eigenvalues, it is better to explain what is intended as *principal components* (PCs). They are new variables constructed in such a way that they are linear combinations of the starting variables, uncorrelated and that the first components contain the major part of information about starting variables. This means also that a p-dimensional space has p PCs. Discarding the

components with less information allows to reduce dimensionality, at expenses of a little part of information. At this point, it is important to point out that the components which carry the large variance are those that preserve more information. For example, consider the scatter plot of a data set shown in Figure 2.2. Within the family of intersecting lines that pass through the centre of our data set, it should be simple to guess that the first PC is the line that matches magenta marks (line segments of the best-fit line), because it is the line that maximizes the variance, i.e. the average distance from projections of data points on the line (red dots) to the origin. Second PC must be uncorrelated with the first, so, within this example, it is obviously a line perpendicular to the first one and it accounts for the next highest variance. Now, it should be clear that the importance of covariance matrix eigenvectors is that they correspond to the directions of axes which carry on maximum variances and it is why we identify them as PCs. The corresponding eigenvalues, i.e. the coefficients attached to each eigenvector, are directly related to the amount of variance in each PC. So, the eigenvector with highest eigenvalue is the first principal component and so on.

4. Feature vector. Once retrieved the PCs, it is possible to choose whether to keep all them or discard those with less information and construct with the remaining ones a matrix of vectors usually named *feature vector*. It is a matrix, V, whose columns are the eigenvectors of PCs we decided to keep. This is the first step towards dimensionality reduction, because keeping only k eigenvectors from p (dimensions of the starting data set), the final data set will have k dimensions and V will be a $p \times k$ matrix. The best fit line we are searching for corresponds to the direction of the first PC, i.e. the eigenvector $\vec{\mathbf{v}}_1$ with the highest eigenvalue λ_1 (multiplied by σ to get back to the original data axes), and pass through the centre of the data set, (μ_x, μ_y, μ_z). By defining the position vector of the point P_0, $\vec{\mathbf{p}}_0 = (\mu_x, \mu_y, \mu_z)$, and the direction vector $\vec{\mathbf{d}} = (v_{1x}\sigma_x, v_{1y}\sigma_y, v_{1z}\sigma_z)$, the parametric equation of the best-fit line can be written as:

$$\vec{\mathbf{p}} = \vec{\mathbf{p}}_0 + t\vec{\mathbf{d}}. \tag{2.4}$$

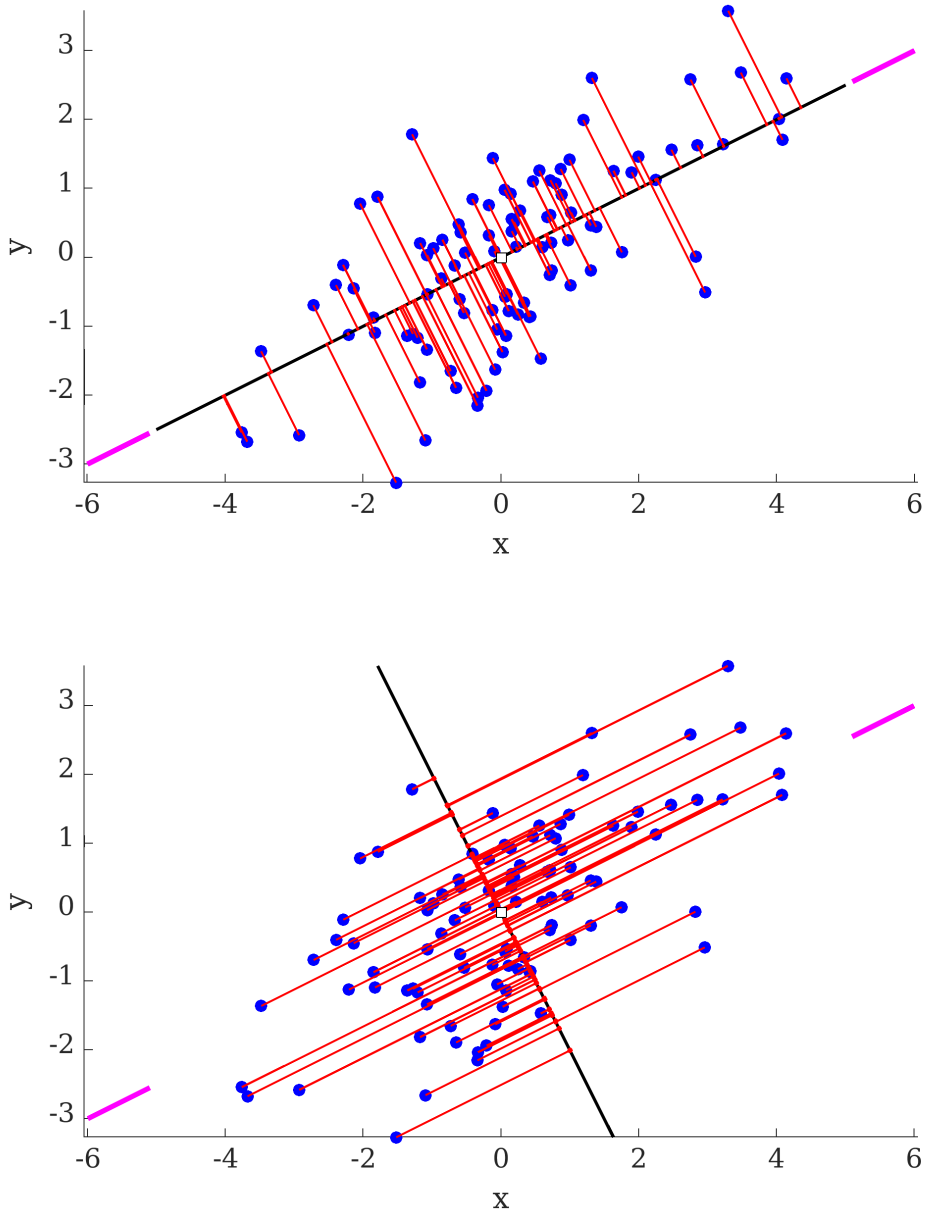

Figure 2.2: Blue circles are an example of two-dimensional data set ($p = 2$). In the top panel is shown the line corresponding to first principal component $\vec{\mathbf{v}}_1$ (black line) together with two segment of best-fit line (magenta marks). Bottom panel represent the second principal component, orthogonal to $\vec{\mathbf{v}}_1$, for the same data set. Red segments are the projections of each data point on the principal component sketched in corresponding plot.

5. Recast data along principal components axes. Till now, starting data, apart standardization, remain always in term of the original axes. In this last step the approximation S_m to original data can be constructed by reorienting them to the principal components, which means simply:
$$S_m = V^\intercal A_m^\intercal. \tag{2.5}$$

Both C++ and MATLAB have libraries which take as input the data set arranged as matrix A and return principal components in descending order.

Going back to our goal, it remains to introduce a stage to check if the distance between each point of A is within the distance threshold from line $\vec{\mathbf{p}}$, but this is a simple linear algebra problem. Pseudo-code 3 describes the full procedure for alignment check. In the end, we retrieve for each combination (x_i, y_i, z_i) the corresponding line equation, given by $\vec{\mathbf{p}}_{0i}$ and $\vec{\mathbf{d}}_i$, a truth table, which reports if each point of the combination satisfies alignment condition, and the sum of squared residuals that, in case of multiple aligned combinations, allows to establish the better one, i.e. the one that can be associated to a particle event.

2.2.3 Events classification

In accordance to what exposed until now, reconstructed tracks which satisfy the alignment check, so that they can be associated to a particle event, can be properly divided into the following groups:

- *gold-events*, which are events coming from six single-hit (a couple X-Y for each tracking module) aligned along a line;
- *silver-events*, i.e. aligned tracks which comes from five single-hit and a multiple-hit (that can generate one or more clusters);
- *generic-events*, which include all other possibility outside the first two categories.

It is important to underline that the procedure previously described for track reconstruction and event selection is based on the assumption that

Pseudo-code 3: Alignment check procedure (MATLAB-like).

Input: A (3×3 matrix), *dist_thr*

```
// Step 1:
/* Compute mean of data along first dimension                    */
avg = mean(A,1) ;                                  // (μ_x, μ_y, μ_z)
/* Compute standard deviation of data along first dimension      */
st = std(A,1) ;                                    // (σ_x, σ_y, σ_z)
/* Standardization                                               */
xyz = (A .- avg) ./ st;

// Steps 2, 3 and 4:
/* Get feature vector                                            */
V = pca(xyz); /* Extract first PC                                 */
v_1 = V[ : , 1] ;                                  // left-most column
/* Find the line:  p = p_0 .+ t*d                                */
p_0 = avg; d = (v_1)^T .* st;

// Last step:
truth_tab = (false, false, false);
squared_res_sum = 0;
for i = 1 : n_col(A) do
    dist = norm(cross(v_1, avg-A(i,:))) / norm(v_1); if dist <
     dist_thr then
        inline(i) = true;
        squared_res_sum += dist^2;
    end
    else
        squared_res_sum = DBL_MAX;
        return ;                    // alignment condition not satisfied
    end
end
```

Result: p_0, d, truth_tab, squared_res_sum.

```
// Operators preceded by a full stop describe element-wise
   operations, i.e.  operations element by element.
```

just one particle interacts with the detector within a coincidence time window. In fact, it has been explained that when there are multiple aligned tracks reconstructed within the same event, only one is chosen as a true particle event. Multi-track events reconstruction, related to the almost simultaneous detection of two or more particles, is not straightforward, due to reduction channel system employed. Fake hits due to noise could mimic the effects of a multi-track event, i.e. at least two cluster on each plane. A detailed analysis about this kind of events can be found in [69] and it shows that an average ratio of the order of 10^{-5} was estimated for multi-track with respect to single-track events. Hence, until now, it is established to exclude multi-track events from muography analysis.

Gold and silver-events correspond obviously to unambiguous tracks so they are considered more reliable than generic-events, because former come from raw data that can include noise effects in at most one coordinate for only one plane.

2.3 Detector characterization

Once established the procedure to get the trajectory of each particle whose interaction has been detected by the telescope, some other preliminary operations remain to be performed in order to fully characterize the detector performance.

2.3.1 Compensation of residual misalignment

Besides the tracking modules have been mechanically aligned during telescope assembly, a further check on possible residual misalignment was made as further step towards muon imaging. The quantities investigated are the:

$$\delta x = x_1 - 2x_3 + x_2, \tag{2.6}$$

$$\delta y = y_1 - 2y_3 + y_2. \tag{2.7}$$

In fact, by assuming that tracking module T_3 is exactly in the middle between the others, i.e. $\|z_1 - z_2\| = D$ and $\|z_1 - z_3\| = \|z_3 - z_2\| = D/2$, it is easy to deduce that the relationships $x_1 - x_2 = x_2 - x_3$ and

$y_1 - y_2 = y_2 - y_3$ apply for three point belonging to the same line. As a consequence, the residuals introduced in Eqs. 2.6 and 2.7 account for misalignment with respect to the best-fit line.

Figure 2.3 shows the distribution of δx and δy, without any compensation of misalignment, calculated for the data set of gold-events acquired during the first measurement campaign at North-East Etna crater in 2017.

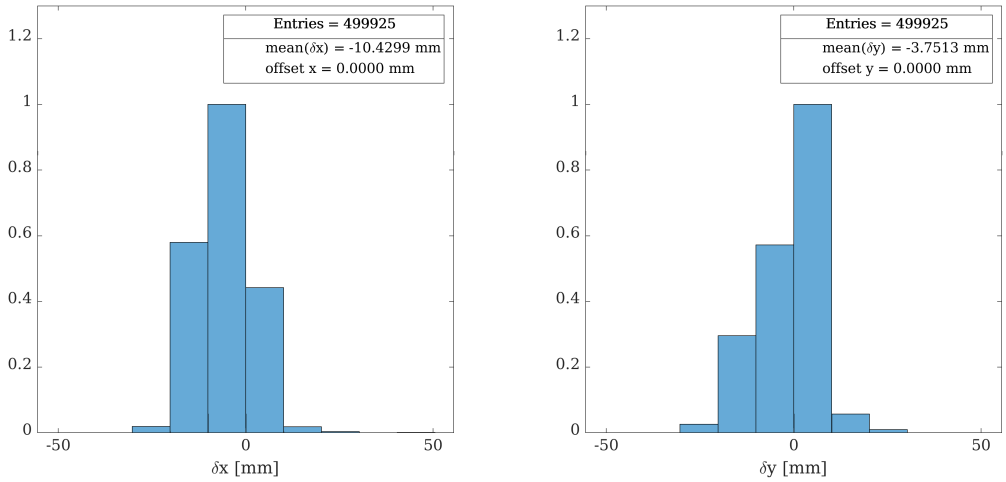

Figure 2.3: Normalized histograms of δx and δy computed for gold-event tracks reconstructed without any offset for the data acquired at NE Etna Crater in 2017.

The residuals can be minimized by fixing two of three coordinate for each direction X and Y while shifting the latter by an offset. Among the possible combinations, we considered several offsets for (x_3, y_3) in order to minimize the average residuals and maximize the number of reconstructed tracks which fulfil the alignment condition. Figure 2.4 shows the residual distribution obtained by shifting $x_3 \to x_3 - 5.215\,\text{mm}$, $y_3 \to y_3 - 1.876\,\text{mm}$. The number of reconstructed gold-events increases from 499925 to 506594, i.e. by roughly 1.3%.

In Figure 2.5 the number of reconstructed gold-events is reported as a function of the different trial offsets evaluated, while Figures 2.6 shows trend of residual averages according to the respective offsets.

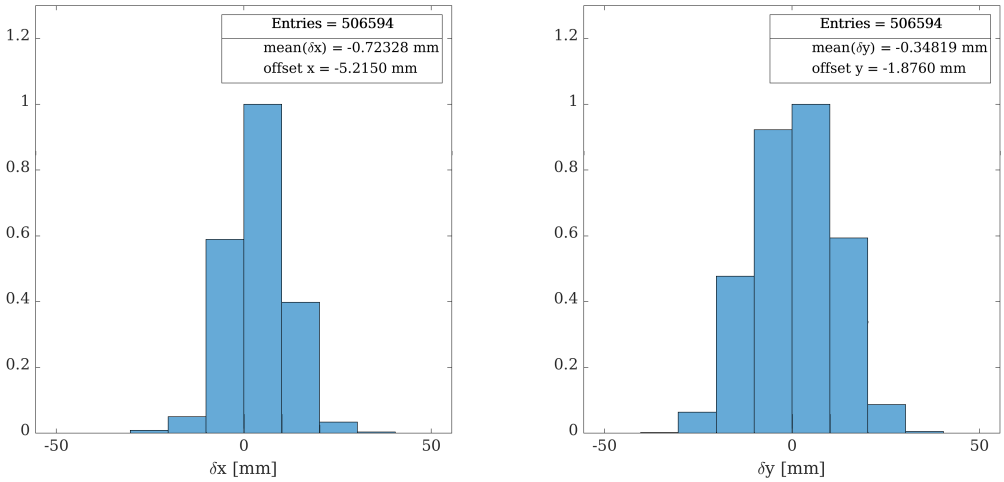

Figure 2.4: Normalized histograms of δx and δy computed for gold-event tracks reconstructed with $x_3 \rightarrow x_3 - 5.215\,\text{mm}$, $y_3 \rightarrow y_3 - 1.876\,\text{mm}$ for the same data set of Figure 2.3.

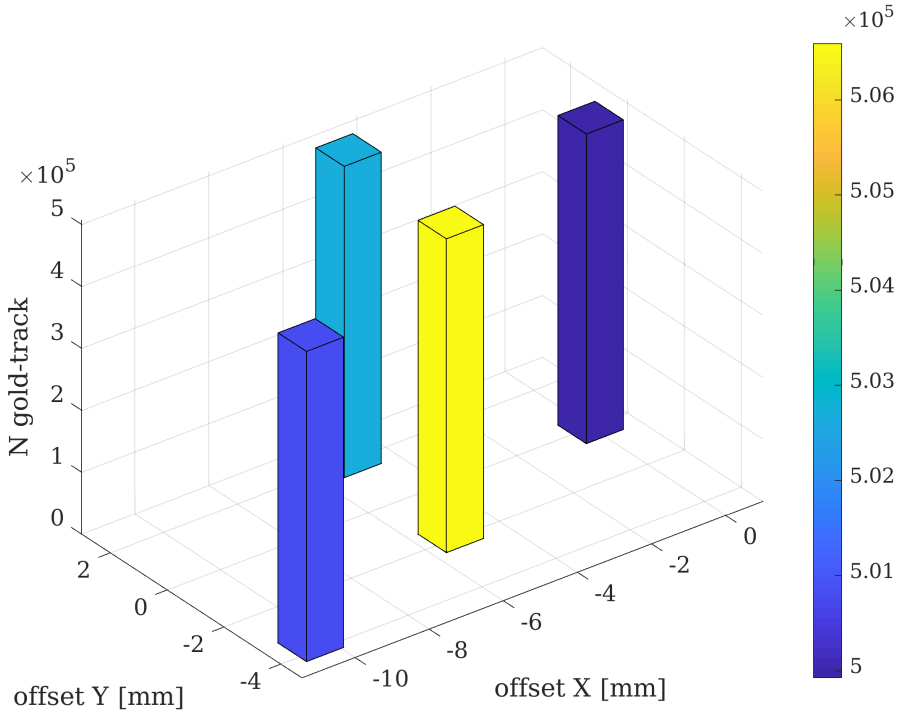

Figure 2.5: Number of reconstructed gold-events as a function of X- and Y-offsets applied to x_3 and y_3, respectively.

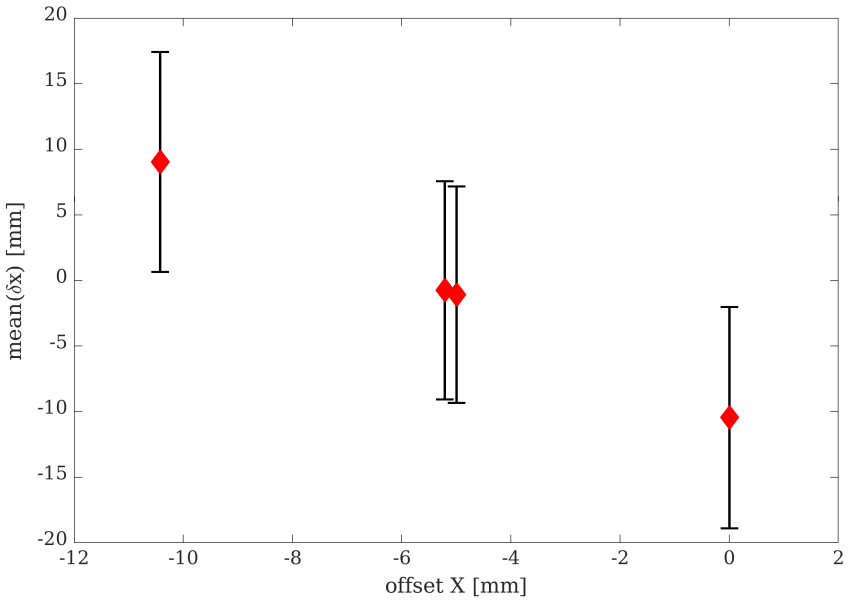

(a)

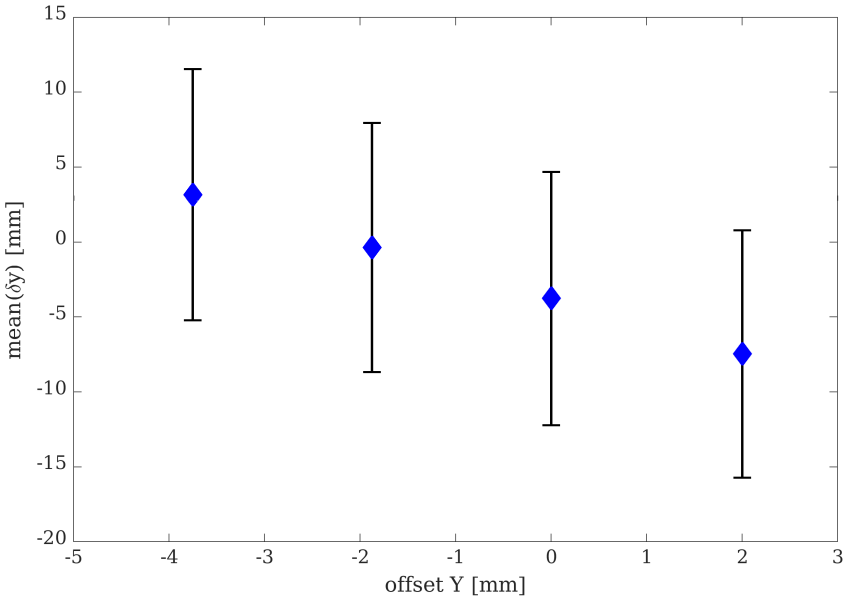

(b)

Figure 2.6: Panel (a) and (b) show the mean of δx and δy, respectively, for the various offsets explored while checking for residual misalignment of tracking modules.

Therefore, residual misalignment of few millimetres in both directions and the slight increase of reconstructed events number confirm the good mechanical alignment achieved while assembling the telescope.

2.3.2 Self-consistent efficiency estimation

A procedure to estimate the detector efficiency was developed, independently of any reference measurement made with other detectors. The procedure is based on the n-tuple of six coordinates $(x_1, y_1, x_3, y_3, x_2, y_2)$ which are candidate to became a gold- or silver-event. For example, consider the case where you want to compute the efficiency of strip layer T_2^y. The procedure searches for the n-tuples which have a single-hit for the first five coordinates $(x_1, y_1, x_3, y_3, x_2)$. For y_2 there are the following possibilities:

1. it is the result of a single-hit or, among the possible y_2 reconstructed from a multiple-hit, there is one which gives an aligned n-tuple.

2. no y_2 corresponds to an aligned n-tuple. Now it is possible to distinguish two sub-cases:

   2a. along the orthogonal coordinate, (x_1, x_3, x_2) are aligned and it is possible to trace back to which y_2 would give an aligned track;

   2b. otherwise, the n-tuple is discarded.

N-tuples corresponding to case 1 are counted in $n_{c,k}$ for each $y_{2,k}$ strip, with $1 \leq k \leq N$, while, each time 2a happens, the number of *expected* n-tuple with $y_{2,k}$, $n_{e,k}$, is increased by one. The detection efficiency of the $y_{2,k}$ strip can be defined as the ratio between latter introduced quantities:

$$\varepsilon_{i,k}^{x_j} = \frac{n_{c,i,k}^{x_j}}{n_{e,i,k}^{x_j}}, \tag{2.8}$$

where i indicates the tracking module T_i and $x_j = x, y$.

Figure 2.7 shows an example of how efficiency for each strip of $T_{1,x}$ is computed: in Fig. 2.7(a) there are the histograms of counted, $n_{c,k}$, and expected, $n_{e,k}$, tracks for each strip; Fig. 2.7(b), instead, shows the

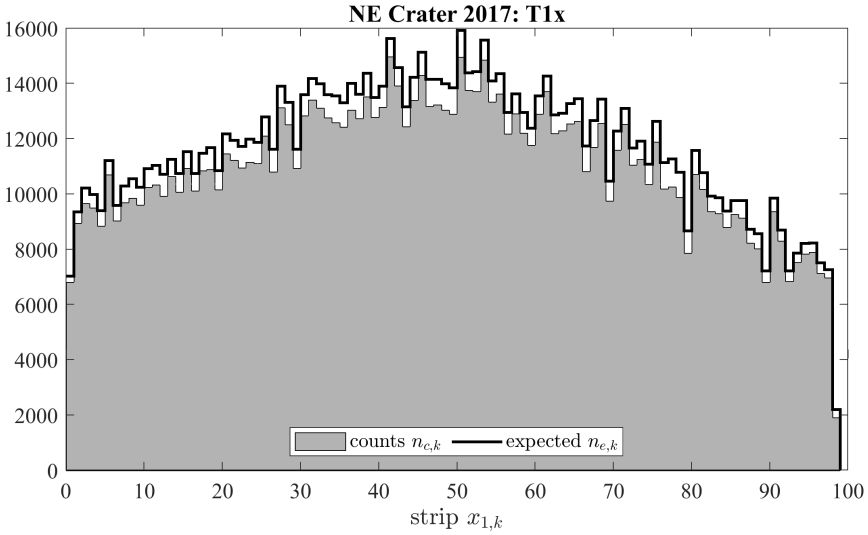

(a)

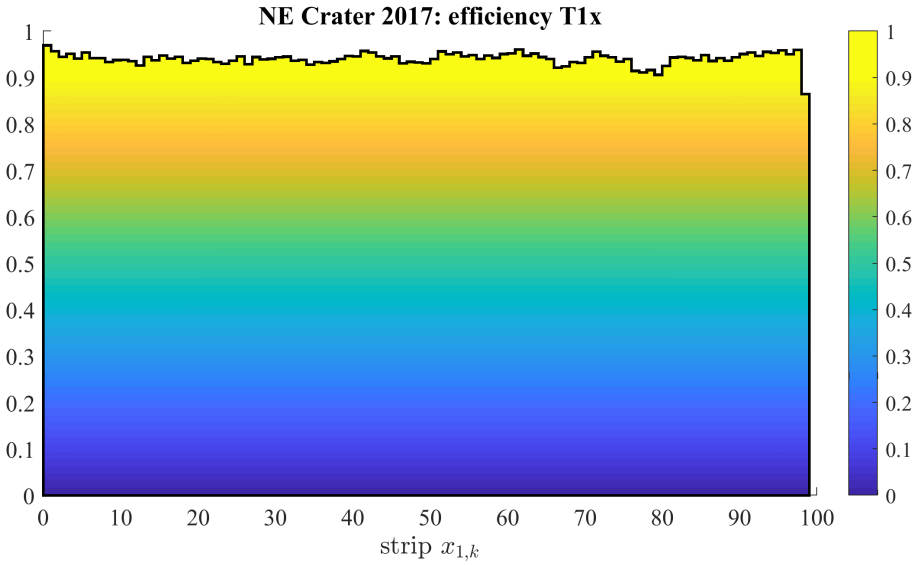

(b)

Figure 2.7: 2.7(a) shows the number of counted and expected tracks, respectively grey patch- and black stairs-plot. 2.7(b) represents the efficiency values calculates according to Equation 2.8 for each strip. Both plots refer to the detection layer X of tracking module T_1 and are relative to the data set acquired during 2017 campaign at NE Etna Crater, as shown in the titles.

	2017	2018	2019
$\bar{\varepsilon}_1^x$	(94.08 ± 1.14) %	(78.18 ± 7.28) %	(89.21 ± 3.58) %
$\bar{\varepsilon}_1^y$	(89.72 ± 3.76) %	(71.83 ± 15.01) %	(87.33 ± 4.50) %
$\bar{\varepsilon}_3^x$	(78.42 ± 12.79) %	(56.13 ± 24.05) %	(85.04 ± 7.16) %
$\bar{\varepsilon}_3^y$	(77.42 ± 13.26) %	(52.96 ± 25.22) %	(73.79 ± 22.78) %
$\bar{\varepsilon}_2^x$	(93.83 ± 1.20) %	(70.40 ± 11.28) %	(86.46 ± 3.81) %
$\bar{\varepsilon}_2^y$	(89.03 ± 3.88) %	(65.01 ± 15.62) %	(85.91 ± 5.54) %

Table 2.2: Mean efficiencies $\bar{\varepsilon}_i^{x_j}$ computed for every year of data taking campaign at North-East Etna Crater.

efficiency $\varepsilon_{1,k}^x$ calculated from Eq. 2.8. This example plots refer to data set acquired during 2017 at NE Etna Crater.

The procedure for computing $\varepsilon_{i,k}^{x_j}$ was performed on each data set acquired at NE Etna Crater and the mean X-Y efficiency for each detection plane are reported in Table 2.2. The complete plot list of counts, $n_{c,k}$, and expected, $n_{e,k}$, tracks histograms with respective efficiencies for each strip of every plane is included in Appendix A.

2.3.3 Real angular acceptance

The coefficients $\varepsilon_{i,k}^{x_j}$ allow to retrieve the real angular acceptance $\mathcal{T}$ of the detector for each data taking campaign. For each direction of sight (θ_x, θ_y) within the telescope field of view, it is necessary to consider all the n-tuples $(x_1, y_1, x_3, y_3, x_2, y_2)$ aligned along this direction and compute their overall efficiency:

$$\varepsilon\left(\theta_x, \theta_y\right) = \prod_{i=1}^{3} \prod_{x_j = x,y} \varepsilon_i^{x_j}. \tag{2.9}$$

The mean of all $\varepsilon\left(\theta_x, \theta_y\right)$ gives the coefficient $\bar{\varepsilon}\left(\theta_x, \theta_y\right)$ that, multiplied by the theoretical acceptance for the same direction $\mathcal{T}\left(\theta_x, \theta_y\right)$, returns the real or *corrected* acceptance $\mathcal{T}\left(\theta_x, \theta_y, \bar{\varepsilon}\right)$. Figure 2.8 shows a comparison between theoretical and corrected acceptance distribution for

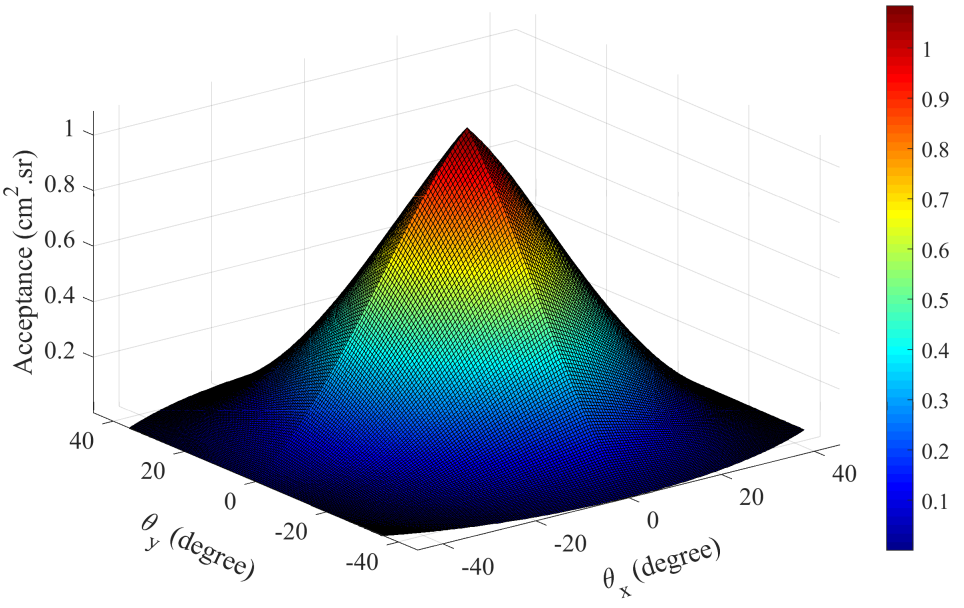

(a)

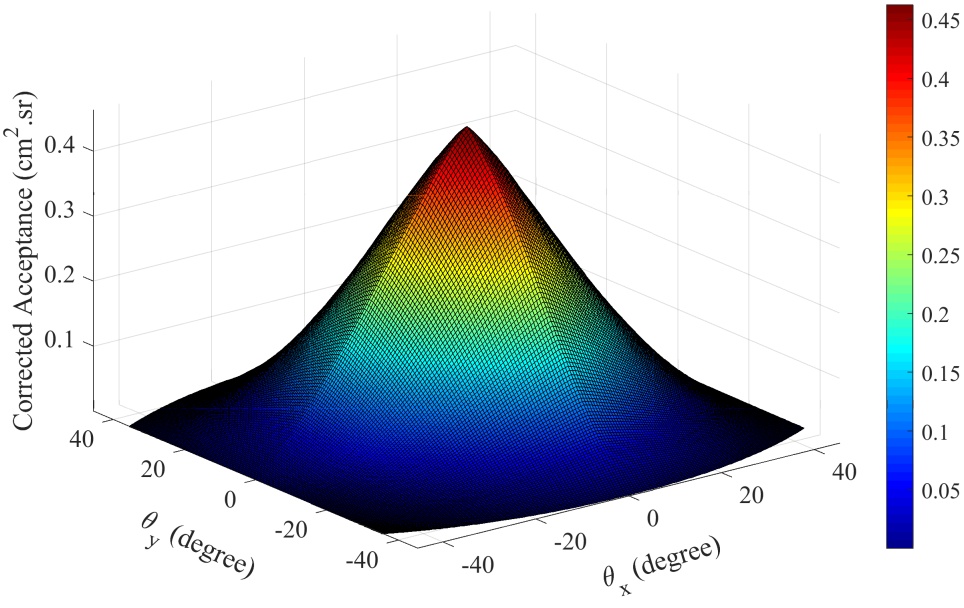

(b)

Figure 2.8: Comparison between theoretical $\mathcal{T}$ (top panel) and corrected acceptance $\mathcal{T}(\bar{\varepsilon})$ (bottom panel) distributions, for each direction of sight of the MEV telescope. The $\mathcal{T}(\bar{\varepsilon})$ distribution refers to the measurement campaign of 2017 at North-East Etna crater.

the telescope during 2017 measurement campaign. In this case, it is possible to see that, besides two distributions slightly differs in shape, the main difference is the peak value, which is reduced by a factor greater than two. It is possible to think that it is as if efficiency reduced the real detection area of the telescope.

To see the $\mathcal{T}(\bar{\varepsilon})$ for other data sets (2018 and 2019), also from other perspective point of views, the reader is request to refer to Appendix B. However, an important evidence of how much the correction by efficiency affects angular acceptance can be given by the maximum of the distribution, reported in Table 2.3.

	2017	2018	2019	Theoretical
$\max(\mathcal{T}(\bar{\varepsilon}))$ $\left[\mathrm{cm}^2\mathrm{sr}\right]$	0.4627	0.0814	0.3905	1.0843

Table 2.3: Maximum of corrected acceptance distribution $\mathcal{T}(\bar{\varepsilon})$, computed for every year of data taking campaign at North-East Etna Crater. Last column of the right reports the maximum of theoretical distribution $\mathcal{T}$.

From Tables 2.2 and 2.3 it is clearly evident that 2018 measurement campaign was afflicted by low efficiency conditions. It is appropriate to remind that particle detection by MEV telescope is a threshold mechanism, as explained in the previous chapter. This means that if the signal level is sufficiently higher than threshold, possible fluctuations of MAPMT gain, which can occur among different devices or distinct anodes of the same detector, are negligible. The 2017 measurement campaign was carried on with optimal MAPMT gain and threshold conditions, which were previously found during the commissioning stage in laboratory and, later, at the INGV facility in Nicolosi [6]. Since 2018, the TOF module was included in the detector and this required some modifications of the set-up, such as switching from unipolar to bipolar fast shaper chain in the MAROC3 chip. Obviously, it was necessary to move the threshold level. But without an easy access to the telescope at North East crater, there were long data taking periods when acquisition conditions were not optimal because threshold and signal levels were too close. At the beginning of 2019, MAPMT high voltage power supply has been suitably increased, allowing the restore a better signal-to-noise ratio.

Chapter 3

Muography results

This chapter reports the preliminary results of three measurement campaigns at Etna Volcano. As mentioned earlier, the MEV telescope was installed at 3100 m a.s.l. on the slope of North East crater since 1st August 2017, after the conclusion of the test phase. First data taking campaign lasted until snow covered solar panels and the electronics turned off within a few days, when the battery pack discharged. The detector remained buried under a huge snow coverage during all winter and only at the end of July 2018 it was possible to restore the power supply and start a new acquisition. Again, with the incoming winter, the telescope shut down after the solar panels were covered. The design of the detector has demonstrated to be able to overcome exceptional weather conditions during winters at high altitude without detriments to electronics and tracking modules. Only the components outside of the box were partially damaged, i.e. solar panels and antennas for data transmission over LTE network. Third data taking campaign is currently ongoing (September 2019) since July, after the substitution of the damaged external elements. However, this work includes data acquired until August 25, 2019. Table 3.1 shows the time statistics for every measurement campaign referred by year. The effective acquisition time, reported in the rows below the number of days for which each measurement campaign lasted, takes into account short periods of interruption due to telescope maintenance.

Results reported in the following refers to events reconstructed with

	2017	2018	2019
Days of acquisition	57	95	34
Seconds of effective acq.	4691447	8081590	2811325
Effective days	54.30	93.54	32.54
Duty cycle	95.26%	98.46%	95.70%

Table 3.1: Nominal and effective acquisition time for each of three data taking campaign.

	2017	2018	2019
Total reconstructed events	22237352	1931467	1897242
% (gold- and silver-events)	25.86%	34.61%	23.73%

Table 3.2: Number of reconstructed events by means of modified DBSCAN procedure.

modified DBSCAN clustering algorithm (page 39) applied to each tracking module. In order to filter out electronics induced noise signals and according to what discussed describing the procedure, events with more than two group- or strip-set bits high for at least one plane were rejected. In addition, the condition on maximum number of points belonging to the same cluster was retained equal to four. Total number of events reconstructed is reported in Table 3.2, together with the percentage of gold- and silver-events gathered. This value can be considered as an index of clustering procedure effectiveness. In fact, a higher number of gold- and silver events means that events reconstructed from data in which one or more coordinate have multiple-hit constitute a smaller extent of the total. Values in Table 3.2 are the first evidence of the lower detection efficiency estimated for 2018 campaign with respect to the others.

Figures 3.1 to 3.3 show the plots of integral fluxes acquired during every measurement period. We follow the common practice to display muography data as a function of X and Y displacements, Δx and Δy, between entrance and exit coordinates of muon tracks in telescope external

Event rate [Hz]	2017	2018	2019
Raw data	2.18	0.24	0.66
After ε compensation	4.74	2.67	1.59

Table 3.3: Event rate for the three measurement campaign at Etna NE Crater.

planes. The convention $\Delta x\,[y] = x_1\,[y_1] - x_2\,[y_2]$ is adopted. This means that, if T_1 corresponds to tracking module closest to the target (front-side), $\Delta y > 0$ identifies particles coming from the detector front. On the contrary, $\Delta y < 0$ refers to particles entering the telescope from back-side, i.e. the side facing "open-sky", without any object which could absorb the muon flux in front of tracking module T_2. Into a $(\Delta x, \Delta y)$ bin of these two-dimensional histograms are counted all the particles which have a trajectory centred around the corresponding telescope direction of sight $r_{\Delta x,\Delta y}$, with a dispersion equal to the angular resolution $\delta\Omega(r_{\Delta x,\Delta y})$. This is not a simple convention to show muography data, but it corresponds to assume that the detector can be considered as a point-size object with respect to the target. The bottom steps of the colour scale is set in grey in order to make evident flux variations in the histogram bins corresponding to the target object location, approximately $0 < \Delta y < 40$, with respect to the flux acquired from the open-sky side at the same $|\Delta y|$. Counts increase around centres of upper ($\Delta y > 0$) and bottom ($\Delta y > 0$) half of the histograms comes from the combined effect of telescope acceptance and cosmic-ray muons flux dependence on zenith angle.

Next step in data processing is the compensation of integral flux directly measured by the telescope in order to take into account the non-uniformity of strip efficiency ε. The correction was achieved considering all tracks which pass through the same strip set $(x_1, y_1, x_3, y_3, x_2, y_2)$ and dividing by their overall efficiency computed with Equation 2.9. Further dividing by the effective acquisition time of each measurement campaign you get the event rate for each direction in the FOV of the telescope. This is shown in the top panel of Figures from 3.4 to 3.6, which display the results only for $\Delta y > 0$. Table 3.3 shows rate values of reconstructed

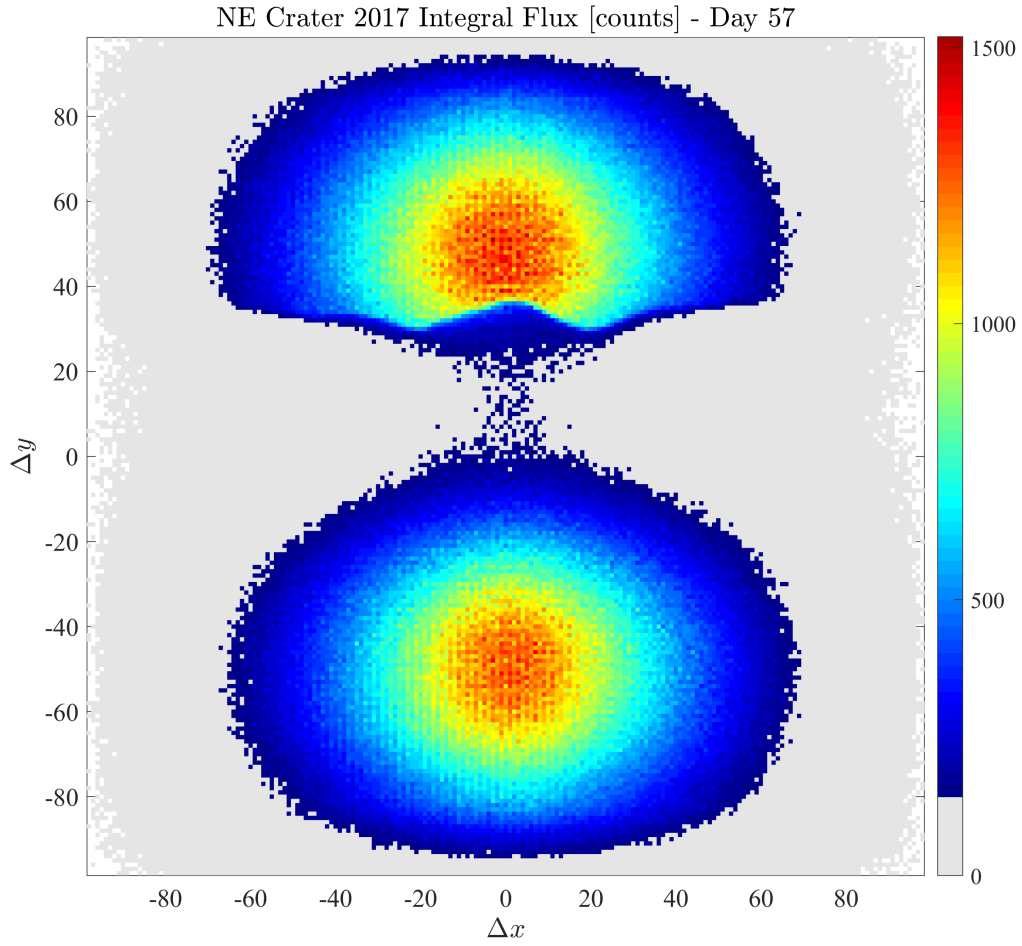

Figure 3.1: Plot of the integral flux acquired from 08/01/2017 to 06/10/2017. Colour bar represents counts per bin in two-dimensional histogram.

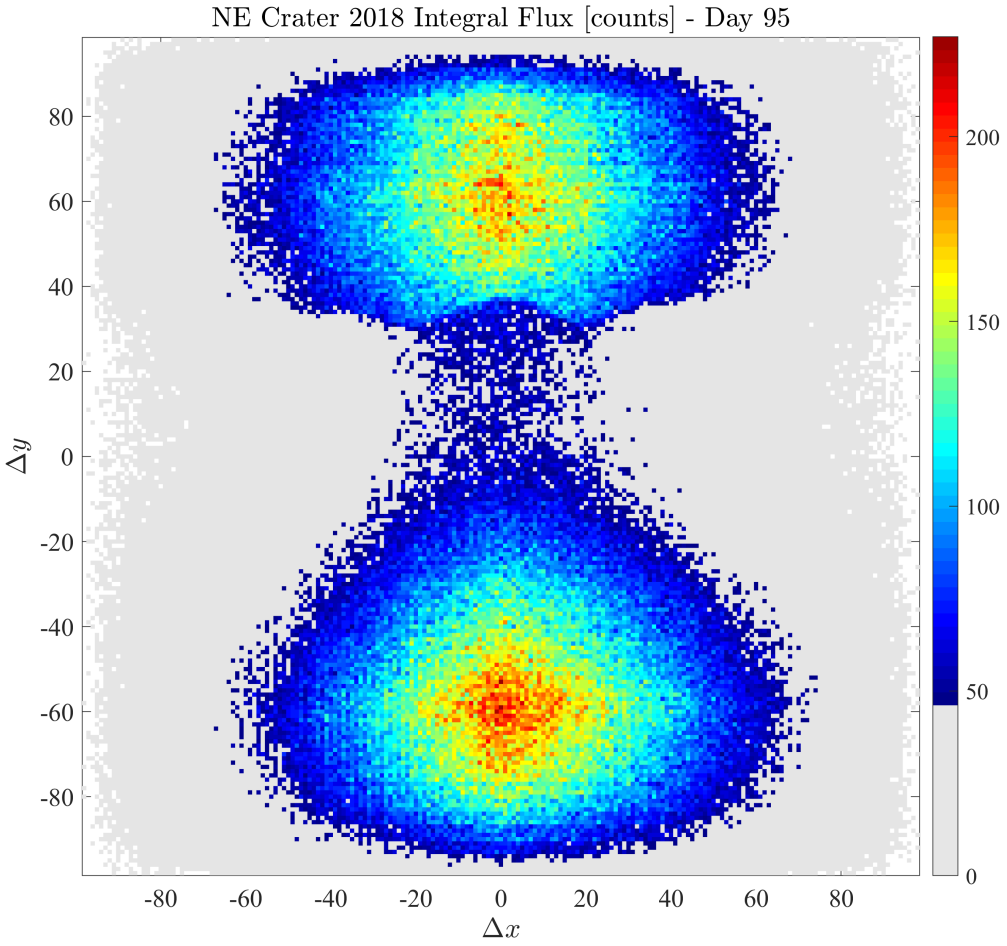

Figure 3.2: Plot of the integral flux acquired from 07/30/2018 to 11/01/2018. Colour bar represents counts per bin in two-dimensional histogram.

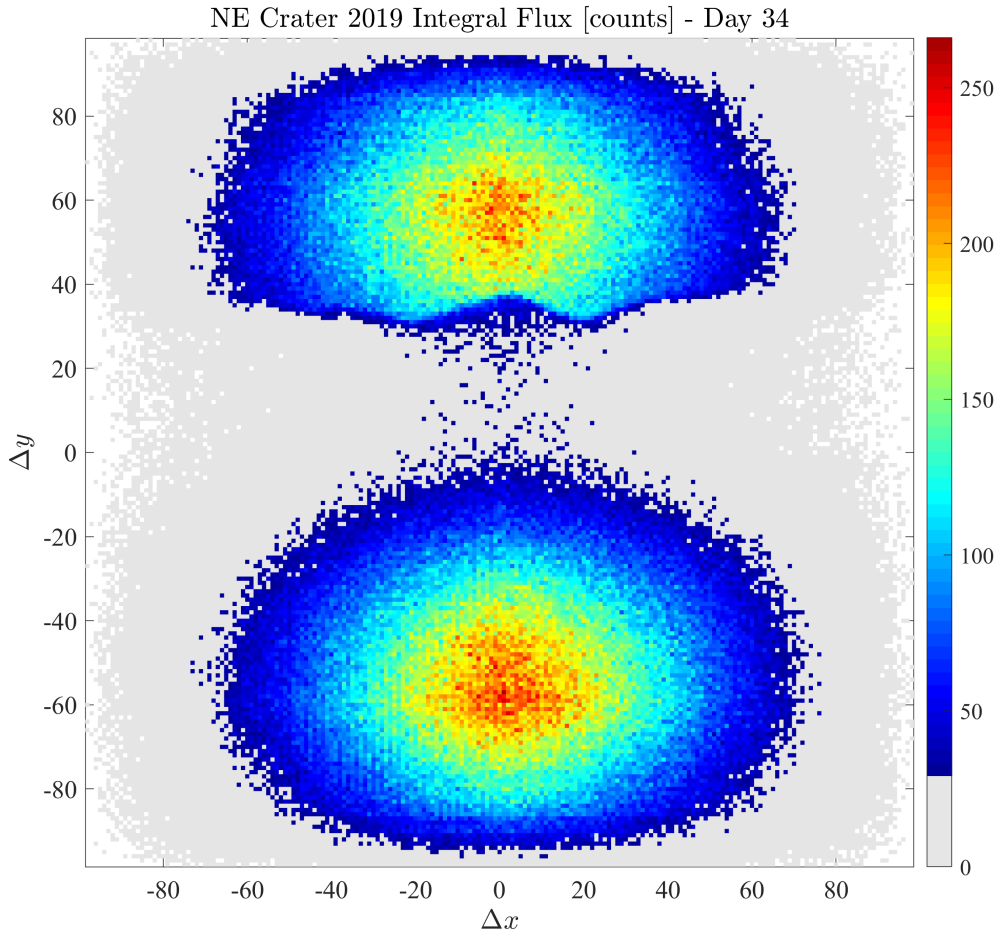

Figure 3.3: Plot of the integral flux acquired from 07/23/2019 to 08/25/2019. Colour bar represents counts per bin in two-dimensional histogram.

events for raw data and after efficiency compensation. Here is evident a decreasing trend in the rate of reconstructed events, also after correction for strip efficiencies. This can be explained as a consequence of multiple factors. First of all, the efficiencies estimated for each strip according to the procedure exposed in the previous chapter (subsection 2.3.2), which is a standard method in data analysis, are based on the number of particles that produced a detectable signal in at least five out of six detection layers. It is not referred to the real number of cosmic-ray muons that should be expected to measure in the corresponding solid angle. Furthermore, as previously explained, during 2018 data taking campaign, some issues arose in finding the best settings of threshold and signal level after the switch from unipolar to bipolar fast shaper chain of the FE chip. Since 2019, a more stringent trigger condition had been introduced and this, as expected, produced an additional lowering of event rate.

Bottom panels of these Figures represent the event rate angular distribution according to elevation angle θ_y before and after compensation for strip efficiencies. The two distributions are normalized in order to fit into the same vertical scale. Event rate attenuation due to Etna NE Crater is clearly evident in these plots by comparing the distribution in range $-0.3\,\text{rad} < \theta_y < 0.3\,\text{rad}$, which are noticeably suppressed for $\theta_y > 0$ with respect to rate at opposite elevation angle, i.e. coming from the open-sky side.

A method to automatically find target object profile from rate distribution was implemented. It scans each column of the rate two-dimensional histogram, i.e. at fixed θ_x, and performs a best-fit with an error function (erf):

$$f(\Delta y) = a + b\left(1 + \text{erf}\left(\frac{(\Delta y - \mu)}{\sqrt{2}}\right)\right), \tag{3.1}$$

$$\text{with} \quad \text{erf}(x) = \frac{1}{\sqrt{\pi}}\int_{-x}^{x} e^{t^2} dt = \frac{2}{\sqrt{\pi}}\int_{0}^{x} e^{t^2} dt. \tag{3.2}$$

In Equation 3.1 parameter a is an offset that shifts $f(\Delta y)$ along vertical axis, b is a constant normalization factor and μ is erf mean. Equation 3.2 is the definition of an error function for a random variable normally distributed with mean $\mu = 0$ and variance 0.5. We are interested in getting parameter μ from the fit, which corresponds to the inflection point of er-

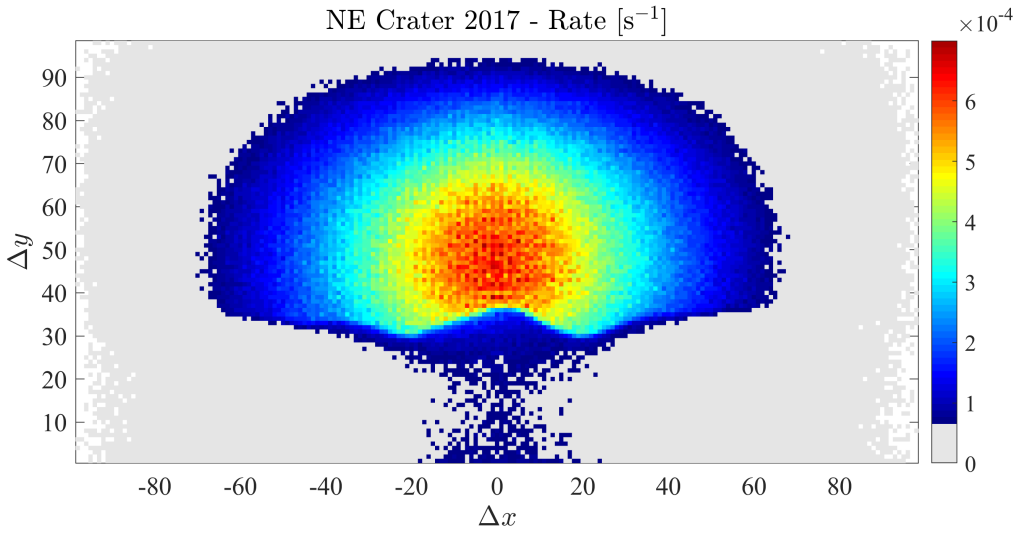

(a)

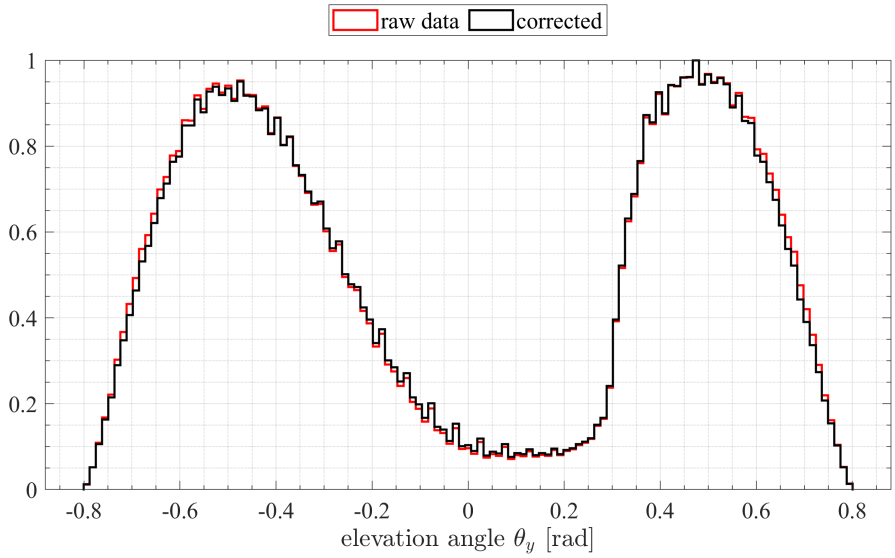

(b)

Figure 3.4: (a) Measurement campaign 2017: rate of events [Hz] coming from the front side of the detector, after correction for strip efficiencies. (b) Normalized rate distribution as a function of the elevation angle θ_y measured from the horizontal $(\theta_y = 0)$. Red stairs plot refers to raw data, i.e. integral flux, while black line shows the angular distribution after correction for efficiency. Normalization factor are equals to about 3.49×10^{-2} Hz and 7.62×10^{-2} Hz, respectively.

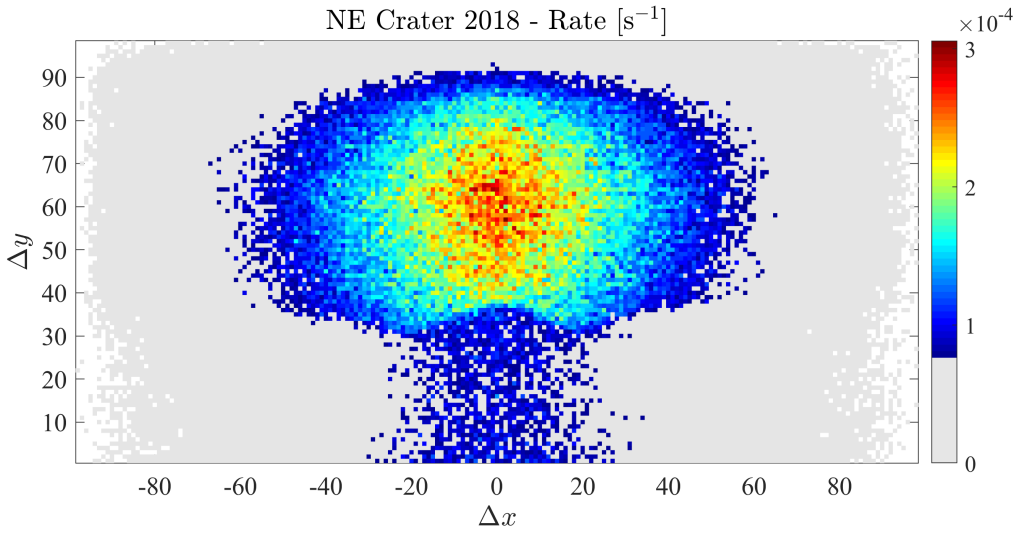

(a)

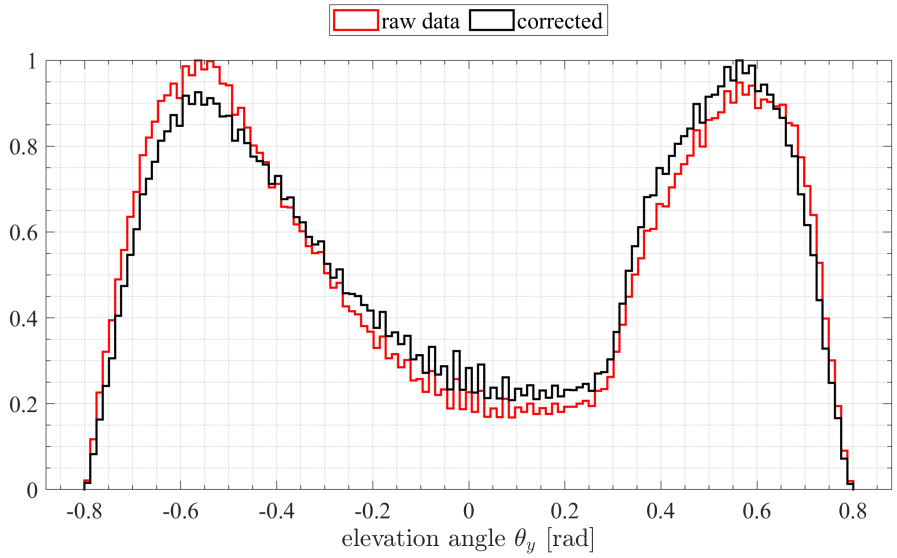

(b)

Figure 3.5: (a) Measurement campaign 2018: rate of events [Hz] coming from the front side of the detector, after correction for strip efficiencies. (b) Normalized rate distribution as a function of the elevation angle θ_y measured from the horizontal $(\theta_y = 0)$. Red stairs plot refers to raw data, i.e. integral flux, while black line shows the angular distribution after correction for efficiency. Normalization factor are equals to about 3.58×10^{-3} Hz and 3.95×10^{-2} Hz, respectively.

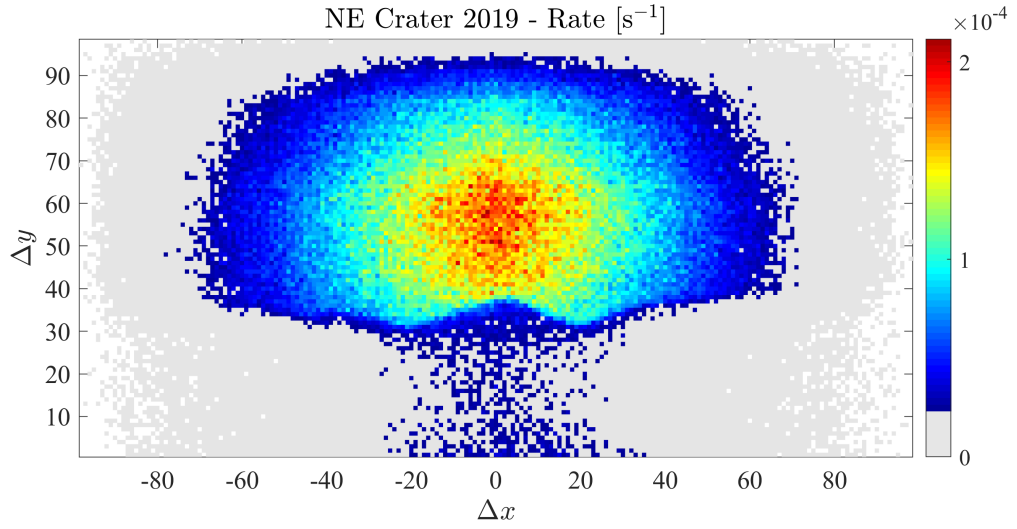

(a)

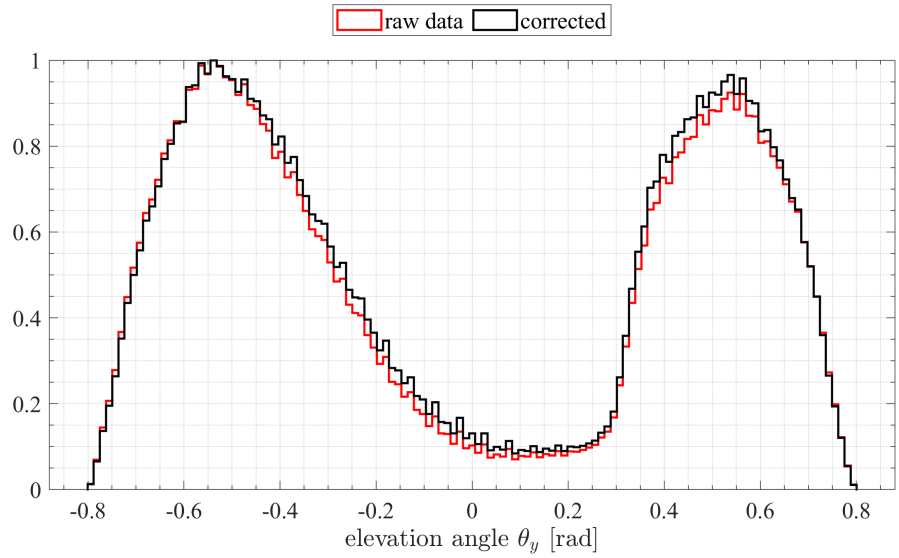

(b)

Figure 3.6: (a) Measurement campaign 2019: rate of events [Hz] coming from the front side of the detector, after correction for strip efficiencies. (b) Normalized rate distribution as a function of the elevation angle θ_y measured from the horizontal $(\theta_y = 0)$. Red stairs plot refers to raw data, i.e. integral flux, while black line shows the angular distribution after correction for efficiency. Normalization factor are equals to about 1.10×10^{-2} Hz and 2.54×10^{-2} Hz, respectively.

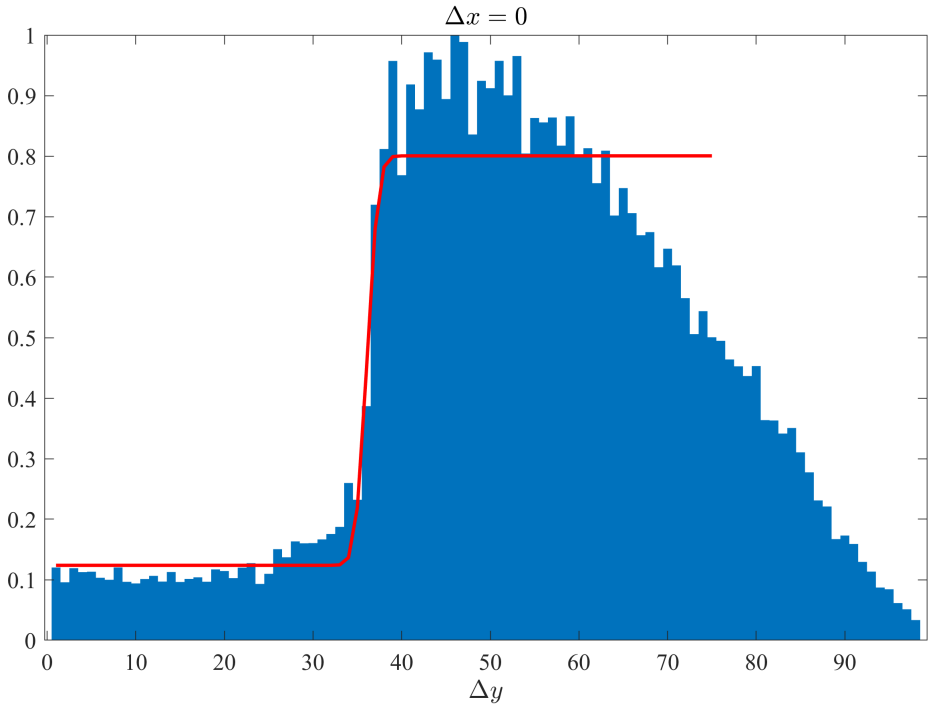

Figure 3.7: Example of the procedure to determine the target object profile by means of erf(x) fit function. The distribution here shown refers to normalized event rate for $\Delta x = 0$ and $\Delta y > 0$ for the 2017 measurement campaign in 3.4(a). Red line shows the best-fit function Eq. 3.1, with $a = 0.1238$, $b = 0.3383$ and $\mu = 36.0758$.

ror function with sigmoid shape. An example of the procedure is shown in Figure 3.7.

Events rate per bin $(\Delta x, \Delta y)$, obtained as just exposed, can be normalized dividing by the angular acceptance $\mathcal{T}(\Delta x, \Delta y)$. In this way, we obtain the event flux measured in counts per (cm^2 s^1 sr^1), which can be compared to the expected cosmic rays flux at the same zenith angle. Figure 3.8 reports the flux distribution computed from 2017 data, together with lines of equals zenith angle θ measured from the vertical, with $\theta = \pi/2 - \theta_y$, i.e. zenith and elevation angle θ_y are complementary angles. Figures from 3.9 to 3.11 show muon fluxes coming from the front side of the telescope for each data taking campaign. NE Crater pro-

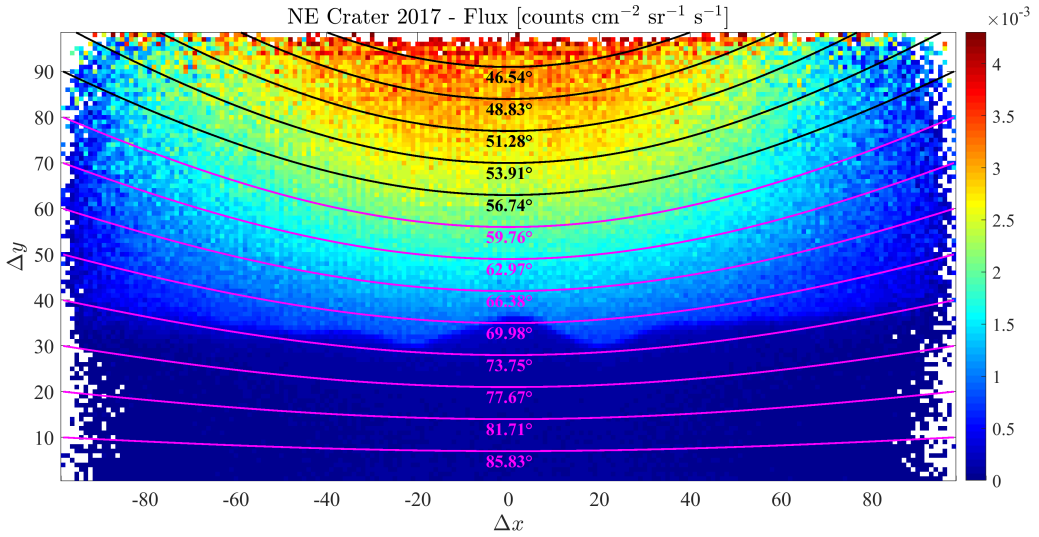

Figure 3.8: Particle flux computed from 2017 data. Magenta and black lines correspond to same zenith angles, reported on the plot, calculated at steps of 10 Δy. Different colours were chosen just to improve visibility.

file, retrieved with the procedure previously exposed is also displayed in each plot. Figures from 3.12 to 3.14, show the corresponding Y-Z profile of flux two-dimensional histograms in Figures 3.9-3.11, together with the expected cosmic-rays muon flux as a function of the zenith angle θ, according to the approximated distribution [70]:

$$\frac{dN}{d\Omega} \approx 0.83 \times 10^{-2} \cos\theta \quad [\text{muon cm}^{-2}\text{s}^{-1}\text{sr}^{-1}]. \tag{3.3}$$

Y-Z profiles pictures make even clearer the differences among the three measurement campaigns, as already discussed in respect of Table 3.3.

In order to further compensate the detector inefficiency, we computed the ratio between expected muon flux at zenith angle corresponding to each bin $(\Delta x, \Delta y)$ and open-sky measured flux, avoiding to include the effect of muon absorption due to NE Crater. In this way, a correction coefficient matrix was obtained and point-wise applied to the flux measured from detector front side. The effect of this latter correction to measured flux, performed independently for each data-set, is shown in Figures from 3.15 to 3.17.

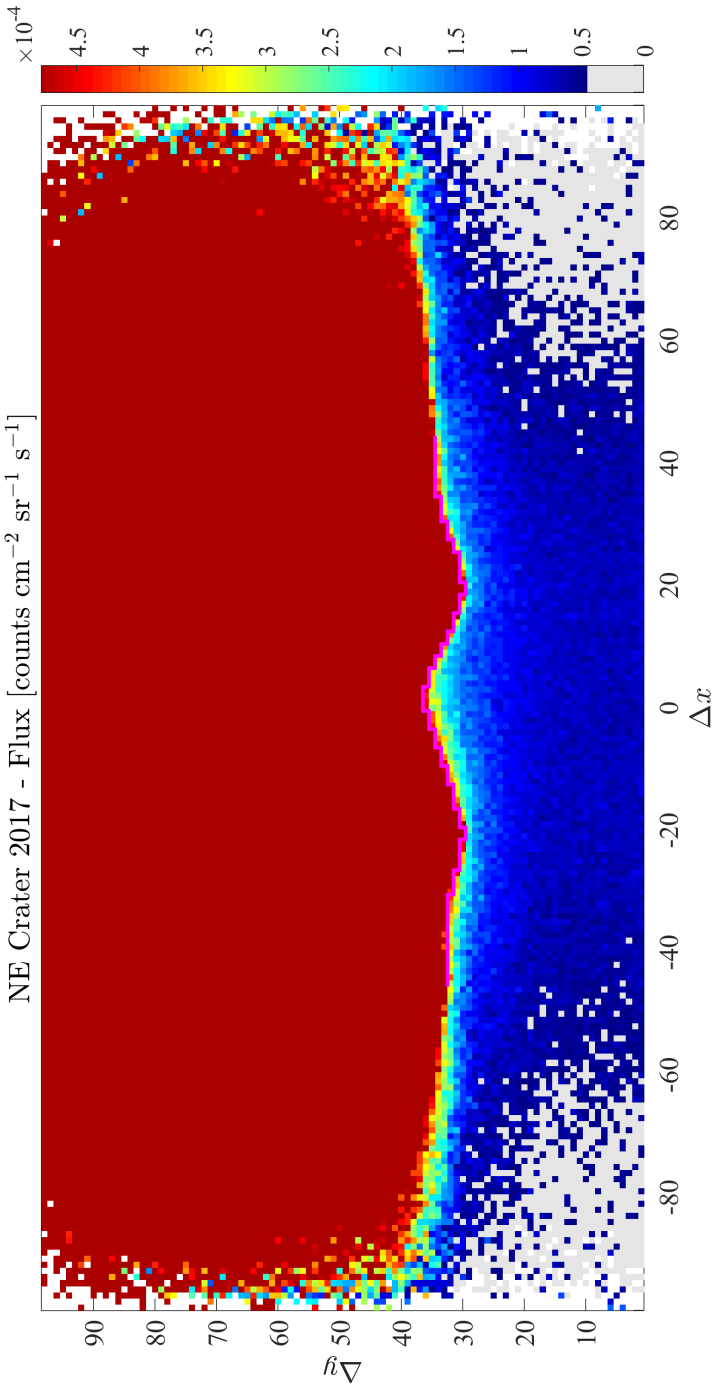

Figure 3.9: Particle flux computed from 2017 data. Colour scale is saturated at maximum flux value in the region of NE Crater. Magenta stairs line corresponds to the profile of reduced flux region retrieved by erf method.

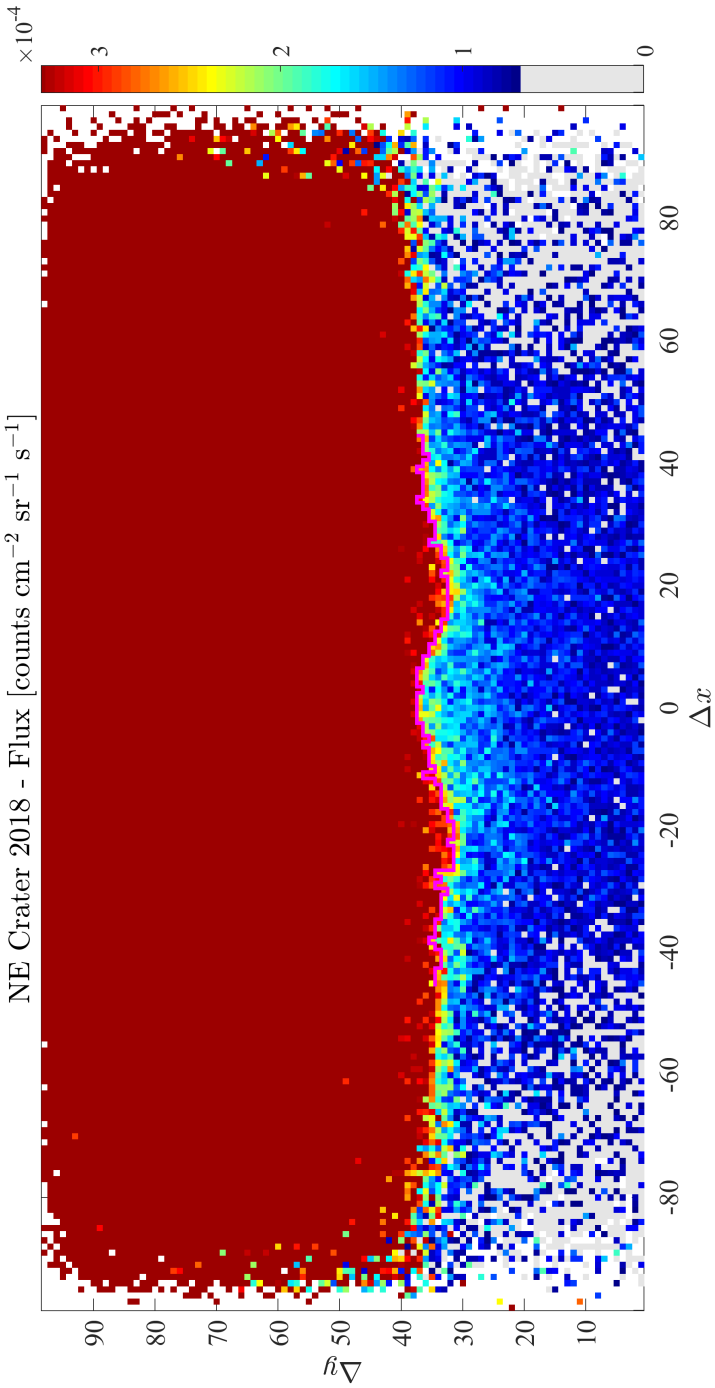

Figure 3.10: Particle flux computed from 2018 data. Colour scale is saturated at maximum flux value in the region of NE Crater. Magenta stairs line corresponds to the profile of reduced flux region retrieved by erf method.

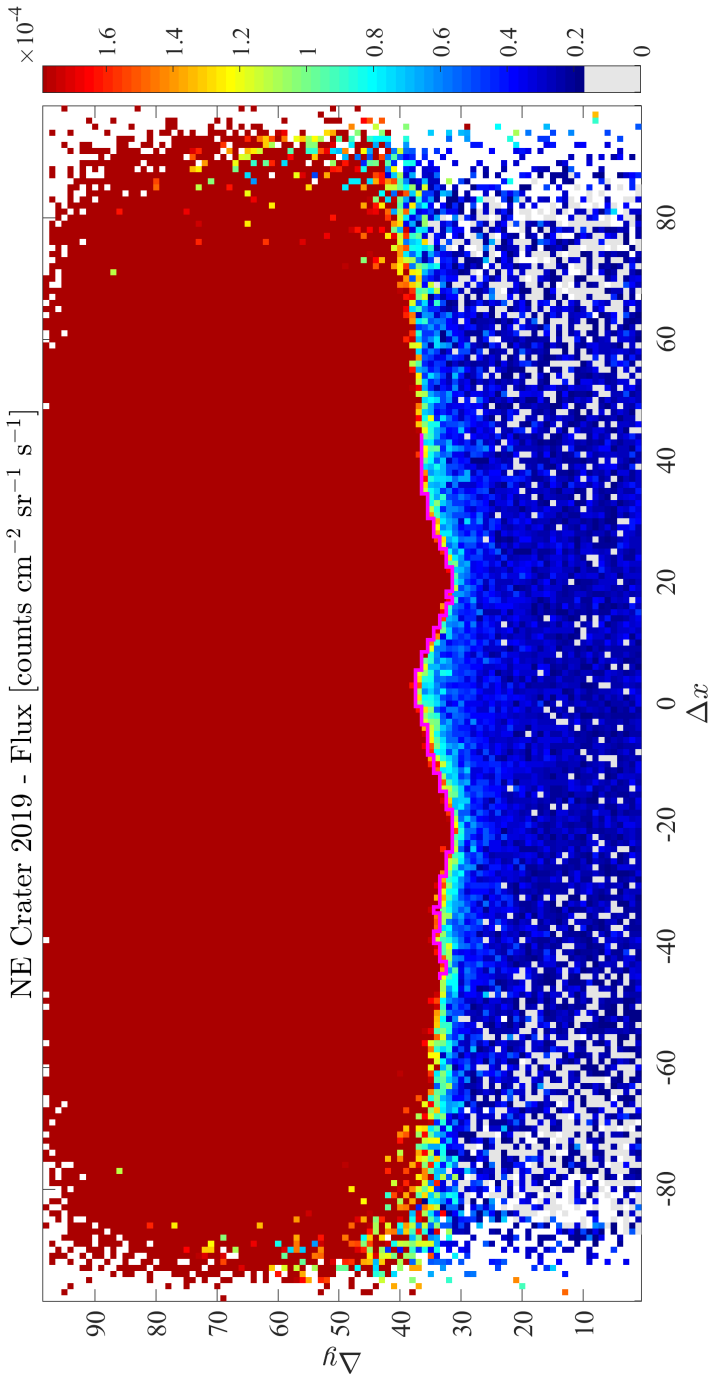

Figure 3.11: Particle flux computed from 2019 data. Colour scale is saturated at maximum flux value in the region of NE Crater. Magenta stairs line corresponds to the profile of reduced flux region retrieved by erf method.

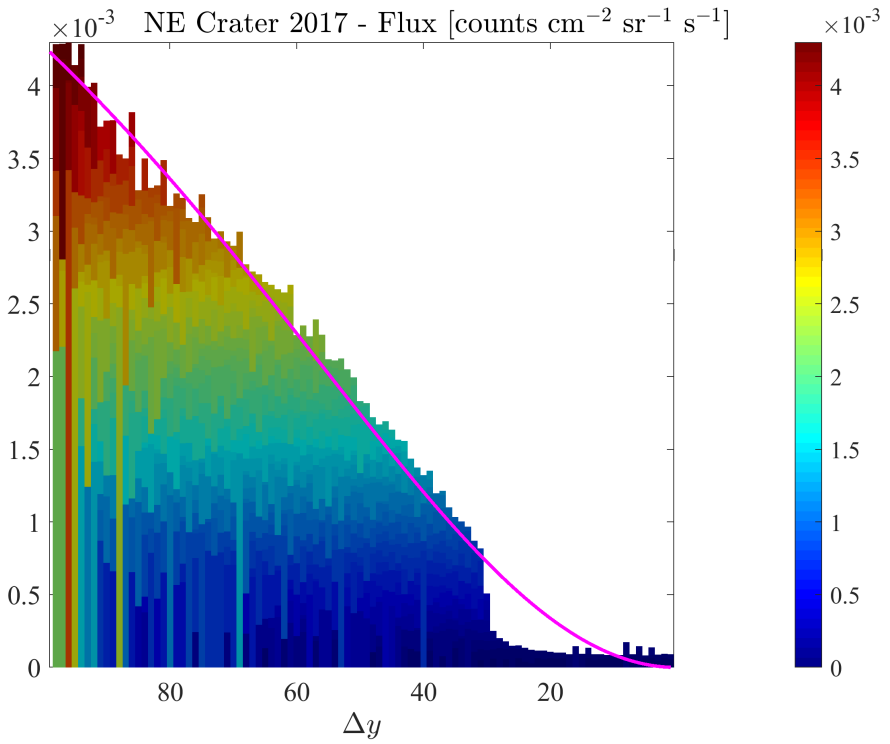

Figure 3.12: Y-Z profile of two dimensional histogram in Figure 3.9, without colour scale saturation. Magenta line represents the expected flux of cosmic-ray muons according to the approximated distribution of Eq. 3.3.

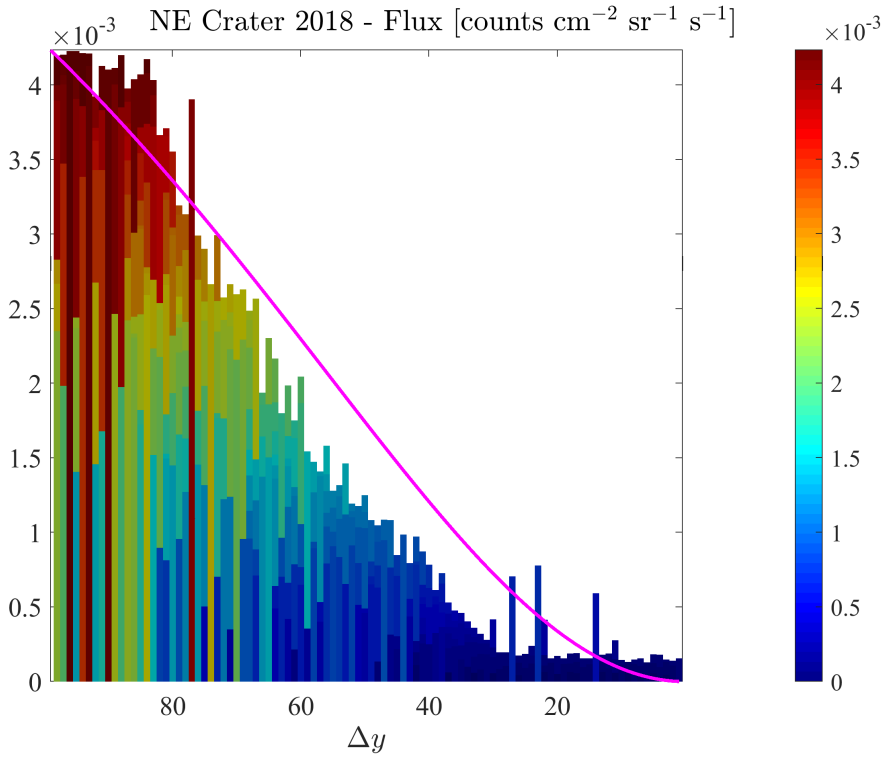

Figure 3.13: Y-Z profile of two dimensional histogram in Figure 3.10, without colour scale saturation. Magenta line represents the expected flux of cosmic-ray muons according to the approximated distribution of Eq. 3.3.

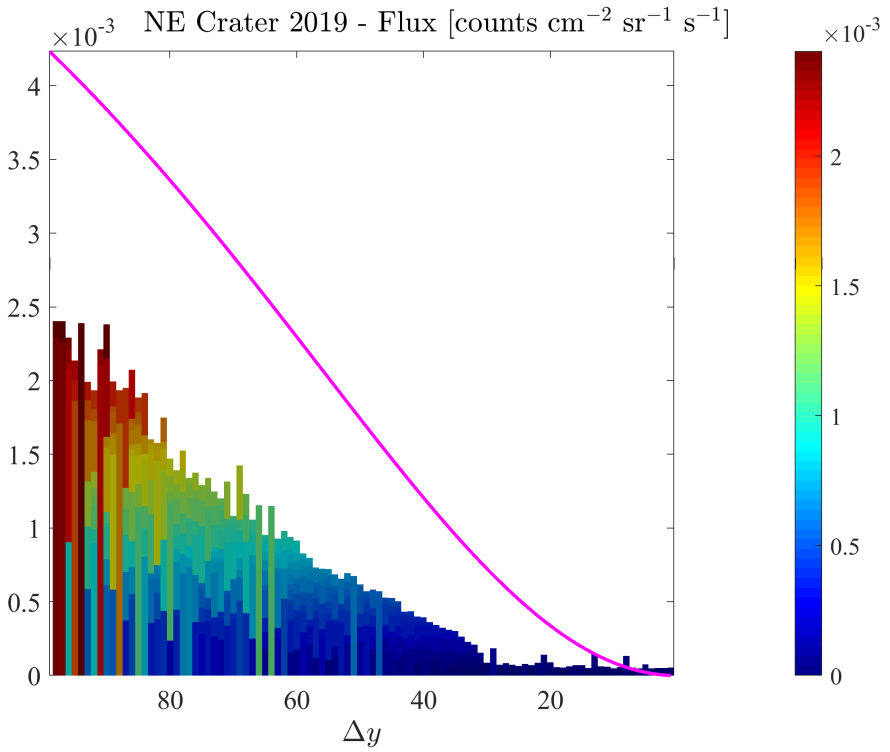

Figure 3.14: Y-Z profile of two dimensional histogram in Figure 3.11, without colour scale saturation. Magenta line represents the expected flux of cosmic-ray muons according to the approximated distribution of Eq. 3.3.

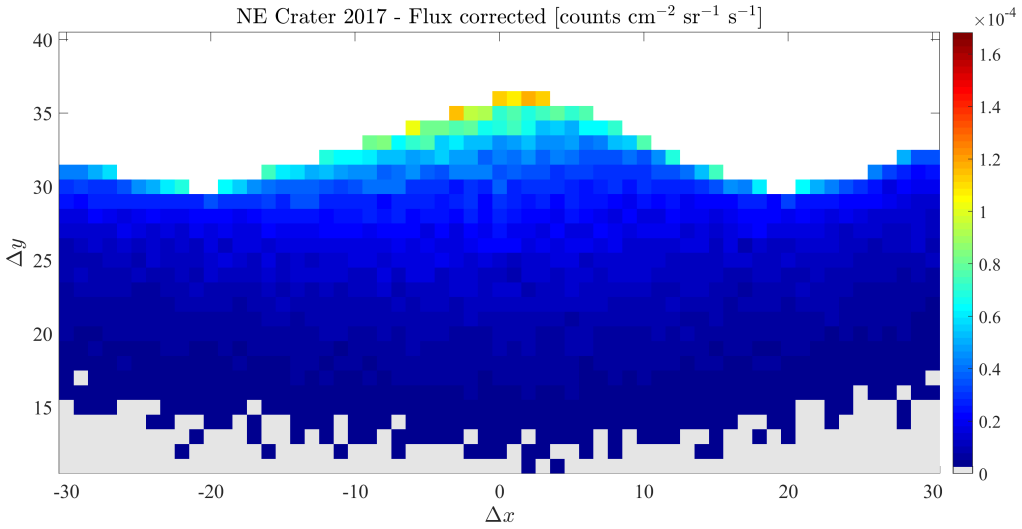

Figure 3.15: Flux corrected from 2017 data in the region of Etna NE Crater. Colour scale is set equal to the one in Figure 3.16, in order to easily compare flux values.

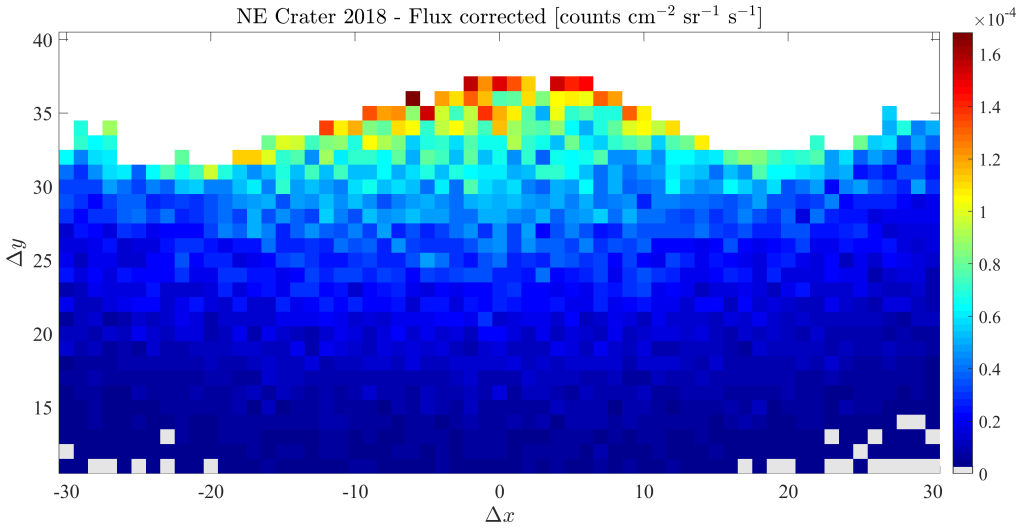

Figure 3.16: Flux corrected from 2018 data in the region of Etna NE Crater.

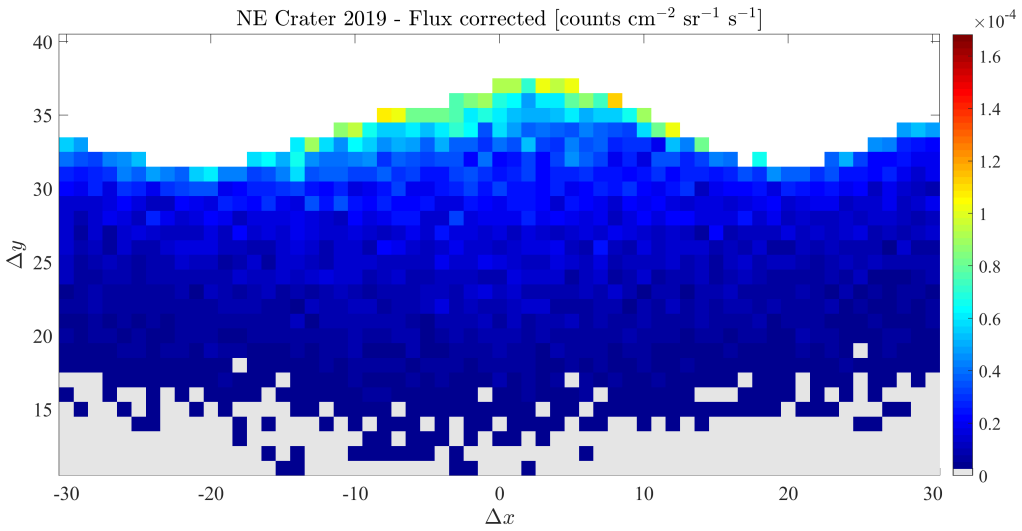

Figure 3.17: Flux corrected from 2019 data in the region of Etna NE Crater. Colour scale is set equal to the one in Figure 3.16, in order to easily compare flux values.

Regarding Figure 3.15 it is possible to notice the transition from flux values around 0.5 counts cm^{-2} s^{-1} sr^{-1} to values greater than 0.6 counts cm^{-2} s^{-1} sr^{-1} which corresponds to absorption effect due to the rear rim of the crater overlapping that of the front edge, as seen from the telescope location (see also Figure 1.2). Around $\Delta y \approx 30$ can be recognized another transition region which correspond to the crater roof. Figure 3.16 shows noticeable variations with respect to the former one: muon flux through the upper region of the crater is higher while for $\Delta y < 30$ the evidence of some conduits can be recognized. These effects can be directly reconnected to the collapse of the crater roof happened during the beginning of 2018, when the telescope was off. According to volcanologic explanation, the collapse was due to high temperature gases which had risen from the inner part of the volcano and corroded slowly the upper structure, until it fell down. Figure 3.17, instead, is quite similar to what obtained from 2017 measurement campaign. In fact, the inner part of an edge collapsed and the material settled down over the crater bottom, increasing the height of the new roof. The evolution of NE Crater as just exposed is confirmed by visual survey of the site, as shown in Figures from 3.18 to

3.20.

However, the last step remains to be accomplished in order to get target density from the measured flux. An extensive series of Monte Carlo simulation by means of Geant4 toolkit [71], MUSIC [72] or PUMAS [73] is required in order to produce a lookup table which will reports the muon flux transmitted through a given material thickness as a function of its density. In order to get valid results, it is necessary to perform this task by means of a simulation software which takes into account also the effect of multiple Coulomb scattering encountered by muons in traversing the material, unlike methods based on analytical approximation of flux absorption. This analysis could unveil density variations also in correspondence with regions of almost equal muon flux values, due to different thicknesses of traversed material through the Crater. In order to accomplish a simulation as close as possible to reality, it is necessary to get a precise Digital Elevation Model (DEM) of Etna summit zone which will allow to compute traversed thickness along each direction of sight of the MEV telescope at its location.

3.1 Background removing by TOF

As explained in section 1.3 and section 1.4, a module for Time of Flight (TOF) measurement was included in the acquisition system and it is correctly operating since the beginning of 2019 data taking campaign. If time-of-flight is defined as $\Delta t = t_{rear} - t_{front} = t_{T_2} - t_{T_1}$, the sign of this quantity allows to set apart front ($\Delta t > 0$) and rear muon fluxes ($\Delta t < 0$). Particles whose incoming trajectories were wrongly reconstructed, have Δy sign opposite with respect to that of Δt, i.e. upward going muons entering detector from the back side are characterized by $\Delta y > 0$ and $\Delta t < 0$, while those coming from the front side have $\Delta y < 0$ and $\Delta t > 0$.

Figure 3.21 shows measured overall TOF distribution (black stairs plot), that appears like a normal distribution with mean slightly shifted toward negative values from 0, due to the prevalence of particles coming from the open-sky with respect to the front flux which includes the target absorption effect. After removing events for which Δt and Δy signs are opposite, two distinct distributions appear (red stairs plot) as expected,

Figure 3.18: This picture shows an example of a long fracture through which hot gases rise from the inner part of Etna Volcano, melting and corroding rocks in fissure walls. Courtesy of Prof. Carmelo Ferlito, Department of Biological, Geological and Environmental Sciences, University of Catania.

Figure 3.19: Etna NE Crater edge before roof collapse happened after 2017 measurement campaign. Here two conduits with rising gas are clearly visible. The inner part of the crater shows initial signs of collapse as concentric rims. Courtesy of Prof. Carmelo Ferlito, Department of Biological, Geological and Environmental Sciences, University of Catania.

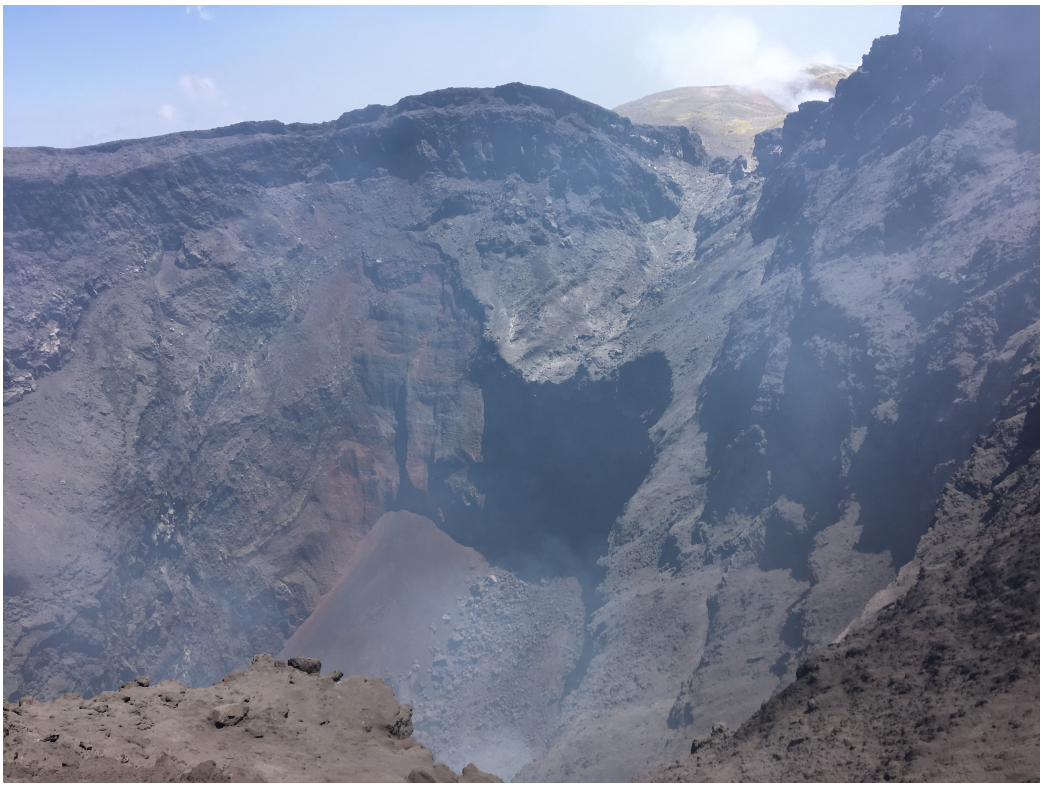

Figure 3.20: Inner of Etna NE Crater after roof collapse, pic taken in July 2018. Central cavity depth is greater than 50 m. Courtesy of Prof. Carmelo Ferlito, Department of Biological, Geological and Environmental Sciences, University of Catania.

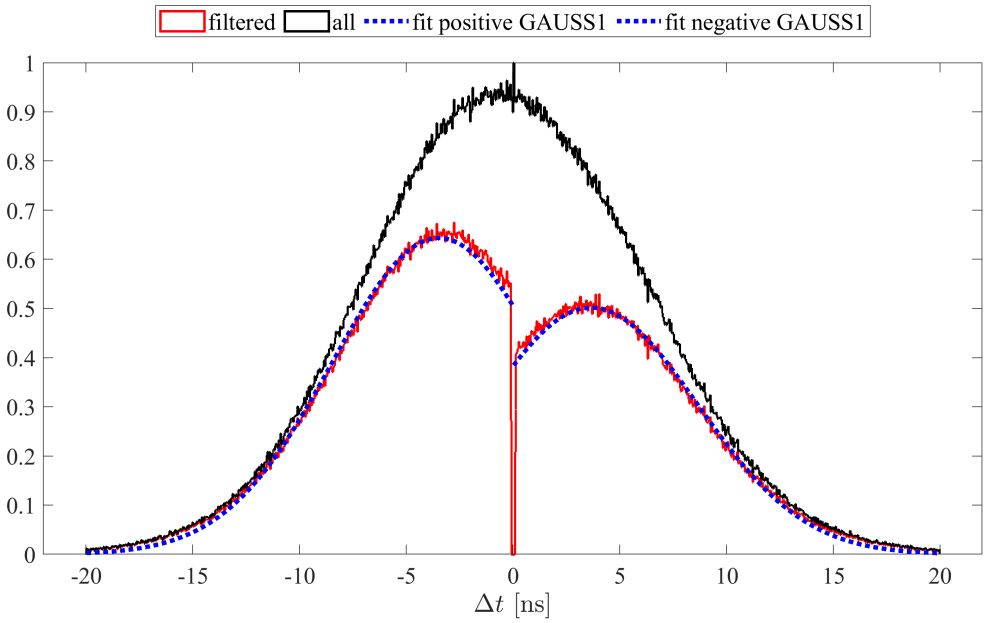

Figure 3.21: Overall (black) and filtered (red) Δt normalized distributions for data acquired during 2019. Blue dot-lines represent two Gaussian distribution used to fit independently filtered positive and negative Δt histograms.

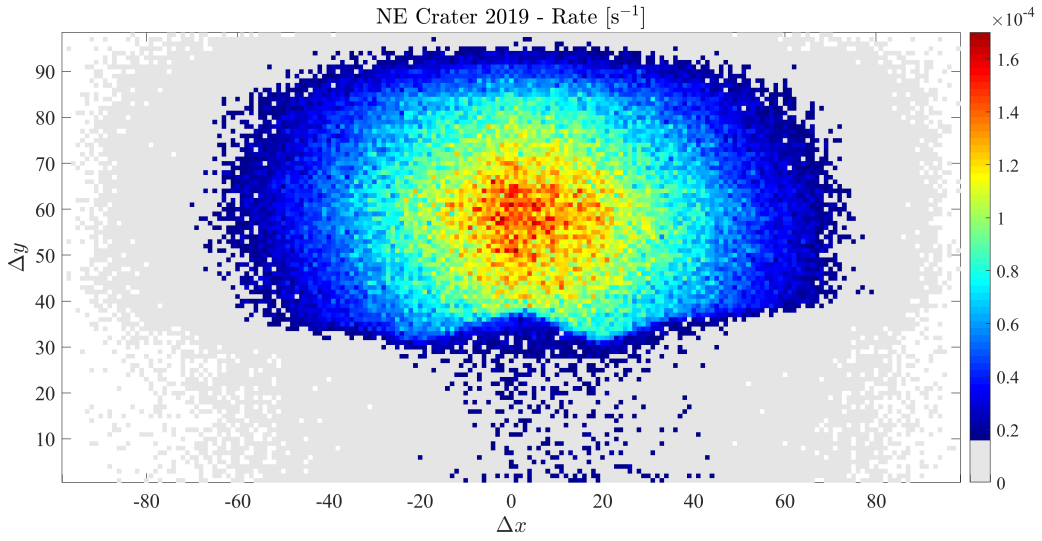

Figure 3.22: Measurement campaign 2019: rate of events [Hz] coming from the front side of the detector, after correction for strip efficiencies and removing upward-going tracks by TOF filtering.

which correspond to front and rear fluxes. TOF filtering procedure excludes also events with $|\Delta t| < 100\,\text{ps}$ and $|\Delta t| > 20\,\text{ns}$, which are well below time resolution of TOF module and over physically acceptable value, respectively. A curve fitting procedure was performed considering independently $\Delta t > 0$ and $\Delta t < 0$ distributions and using a truncated Gaussian function as model for each distribution (blue dotted lines). The two Gaussian have mean equal to $-3.48 \pm 0.087\,\text{ns}$ and $3.659 \pm 0.098\,\text{ns}$, respectively.

The effect of TOF filter are clearly visible also in Figure 3.22, in comparison to 3.6(a). It can be noticed that TOF filtering, besides lowering the overall front flux, removes wrongly reconstructed tracks which pollute the image in area under the crater, in correspondence with telescope maximum acceptance region. As obvious, measured integral flux is higher in this region, but also background noise is gathered here. Another useful quantity to understand how TOF filter acts is the ratio between excluded tracks and overall distribution as a function of the elevation angle θ_y, shown in Figure 3.23 together with the distribution before TOF filter. It is possible to notice two little bumps in the ratio distribution for θ_y ap-

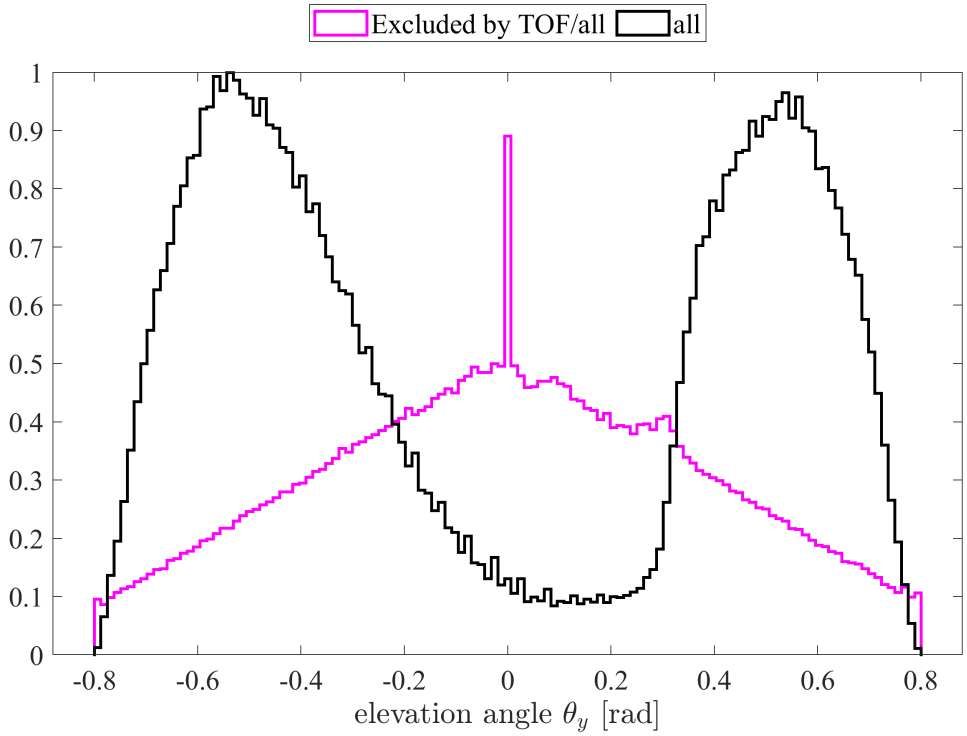

Figure 3.23: Measurement campaign 2019: magenta stairs plot represent the angular distribution of ratio between events discarded by TOF and overall distribution, that is the black stairs plot. Central peak in ratio stair plot is due to removed tracks with $|\Delta t| < 100\,\text{ps}$.

proximately equal to 0.08 rad and 0.3 rad. The first can be connected to removed tracks in the region under the crater, while the latter, at elevation angles corresponding to the transition from flux absorbed by the target to open-sky flux, can be due to low-energy muons scattered in the upper part of the crater. These particles, besides being scattered, lose energy in traversing the target and their TOF is outside acceptable range.

Conclusions

This work resumes the current status of research project for muography of Etna Volcano, within which the PhD candidate developed his activity. It was demonstrated how with ingenious solution it is possible to built a robust and sustainable telescope for muon radiography. Even if the project is still in R&D stage, remarkable results were achieved. In particular, the dynamic evolution of Etna North-East Crater was observed by means of muographic images, supported by volcanologic model that is believed to govern eruptive activity in the summit zone and visual evidences. Data analysis procedure for event reconstruction is now well established, but last step remain to be accomplished in order to get a density map of the target. The new trigger condition introduced since 2019 measurement campaign has been fundamental to ensure synchronization of TDC data with those of tracking modules, but it has lowered trigger rate. A compromise that allows to resume a trigger rate similar to those registered during 2017 and 2018 will be useful to reduce acquisition time. However, the contemporary flux measurement at open-sky enables to compensate reduced rate of event reconstructed in comparison with expected cosmic-ray muon flux.

Furthermore, in order to reconstruct an exhaustive density model of the investigated structure, we retain that it is fundamental to measure cosmic-ray muon flux absorption at the same time with at least two detectors from two distinct perspectives. In fact, the capability to recognize tiny structures, especially in the thicker region of the target, is limited by their orientation relative to telescope directions of sight. For example,

if a conduit develops along a telescope direction of sight, it will be more easily identified because it produce a significant flux increase through the mountain. Otherwise, if the conduit develops perpendicular to telescope direction of sight, flux variation will be very small to be recognized.

Results presented, even if preliminary, suggest to pursue in detector development in order to correct all issues emerged from the experience made with this prototype. A solution under discussion could be based on bars with bigger section that allows to increase the scintillating volume traversed by particles and, hence, light production efficiency. Angular resolution could be kept as current by extending space between telescope external tracking modules. This redesign of detector geometry will also relax TOF measurement that brings with it some challenges at present status. In fact, as shown while discussing it, actual time resolution of TOF module doesn't allow to completely separate front and rear fluxes according to their Δt. An uncertain remains for TOF values near time resolution of the system. In this regard, an innovative smart solution based on directionality of Cherenkov radiation emitted in a transparent solid medium was studied by means of simulations with Geant4 [74]. Preliminary tests with a handmade prototype confirm the working principle of this solution. However, a well engineered construction is fundamental in order to guarantee optical coupling between detector components and to eliminate air gaps which introduce internal reflection of Cherenkov light. Developments concerning TOF measurement and Cherenkov detector for incoming direction discrimination are fundamental to eliminate as much as possible data pollution by background particles.

Despite we are conscious about what is needed to make a better muon telescope, smart solutions included in the current prototype allowed to obtain important results which attracted attention from research community. First conference talk about MEV project results, that was delivered by the candidate in September 2018 at 104^{th} SIF (Italian Physical Society) National Congress, was awarded as best communication in section Geophysics and Environmental Physics [75]. In November 2018, we were invited to join for the first time Muographers annual meeting, which brings together all worldwide excellence in the field. An expression of interest about the project was made by Prof. Hiroyuki K. M. Tanaka from University of Tokyo - Muographix Institute. This has conducted to an

official trilateral academic agreement between the Hungarian, Italian and Japanese Institutes for cooperation between Wigner Research Centre for Physics, the University of Catania and University of Tokyo [76].

Appendices

Appendix A

Efficiency plots

In the following Figures, all the histograms of counts, $n_{c,k}$, and expected, $n_{e,k}$, tracks (top panel a) together with the corresponding efficiencies $\varepsilon_{i,k}^{x_j}$ (bottom panel b) are shown. In order to keep the efficiency plot as clear as possible, the error bar (red vertical line) was drawn only where the confidence interval is $2\sigma_\varepsilon > 0.1$. The title above each panel refers to the data set and detection plane corresponding to the relative plot. All data sets were acquired at North-East Etna crater and, in particular:

- Figures A.1 to A.6 are relative to 2017 measurement campaign;
- Figures A.7 to A.12 are relative to 2018 measurement campaign;
- Figures A.13 to A.18 are relative to 2019 measurement campaign.

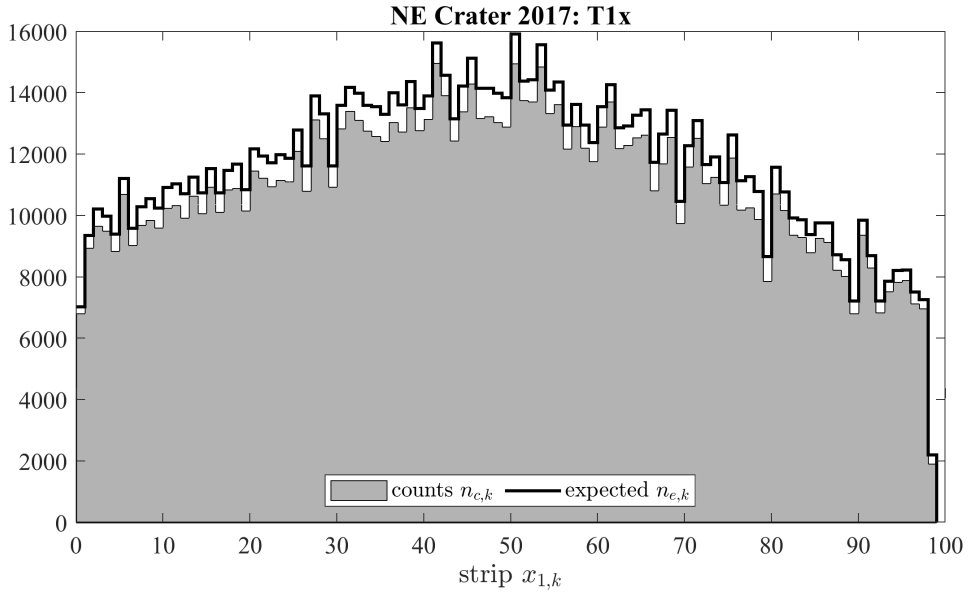
NE Crater 2017: T1x
16000
14000
12000
10000
8000
6000
4000
2000
0
counts $n_{c,k}$
expected $n_{e,k}$
0 10 20 30 40 50 60 70 80 90 100
strip $x_{1,k}$

(a)

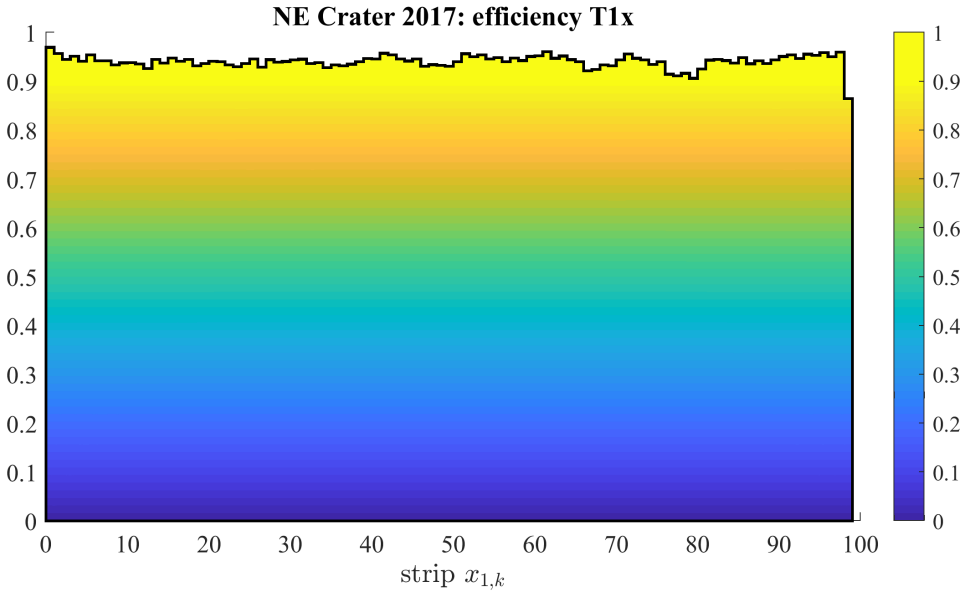
NE Crater 2017: efficiency T1x
1
0.9
0.8
0.7
0.6
0.5
0.4
0.3
0.2
0.1
0
0 10 20 30 40 50 60 70 80 90 100
strip $x_{1,k}$

(b)

Figure A.1

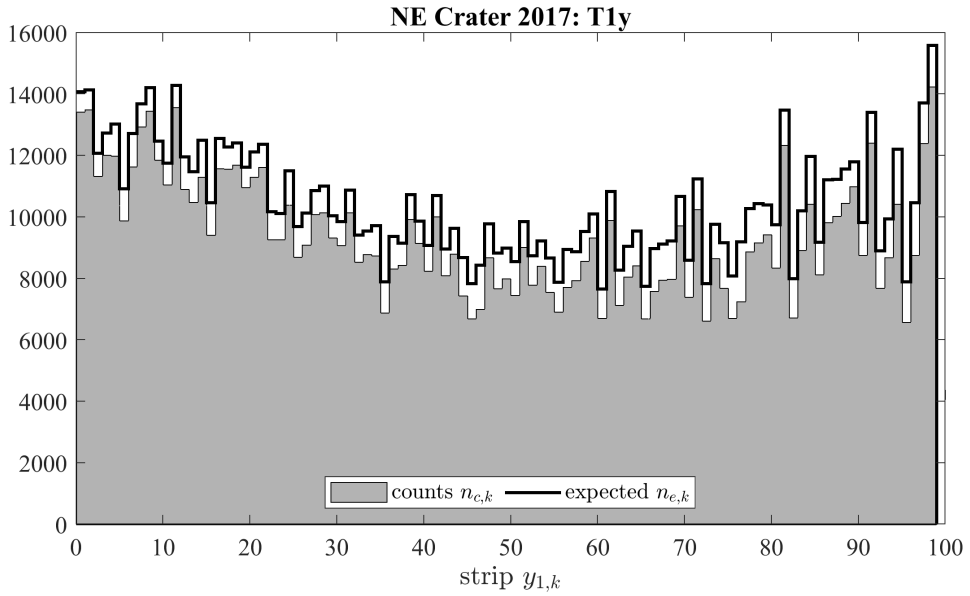
NE Crater 2017: T1y
16000
14000
12000
10000
8000
6000
4000
2000
0
counts $n_{c,k}$
expected $n_{e,k}$
0
10
20
30
40
50
60
70
80
90
100
strip $y_{1,k}$

(a)

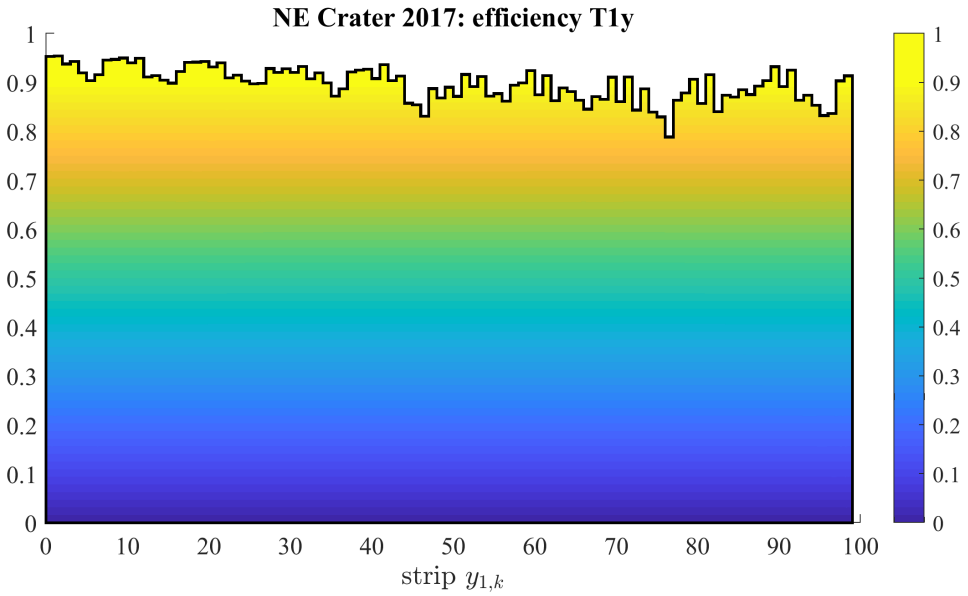
NE Crater 2017: efficiency T1y
1
0.9
0.8
0.7
0.6
0.5
0.4
0.3
0.2
0.1
0
0
10
20
30
40
50
60
70
80
90
100
strip $y_{1,k}$

(b)

Figure A.2

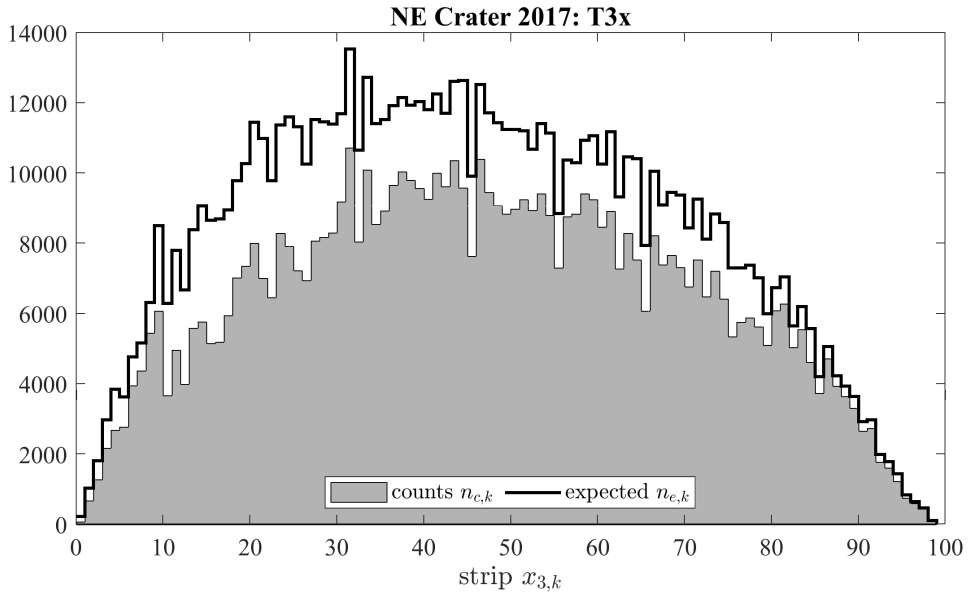
NE Crater 2017: T3x
14000
12000
10000
8000
6000
4000
2000
0
0
10
20
30
40
50
60
70
80
90
100
strip $x_{3,k}$
counts $n_{c,k}$
expected $n_{e,k}$

(a)

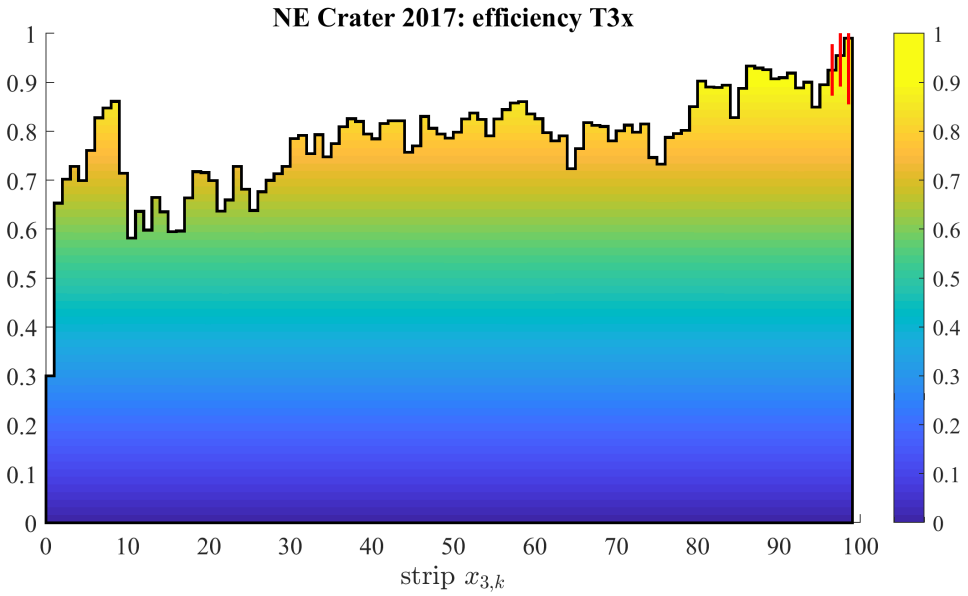
NE Crater 2017: efficiency T3x
1
0.9
0.8
0.7
0.6
0.5
0.4
0.3
0.2
0.1
0
0
10
20
30
40
50
60
70
80
90
100
strip $x_{3,k}$

(b)

Figure A.3

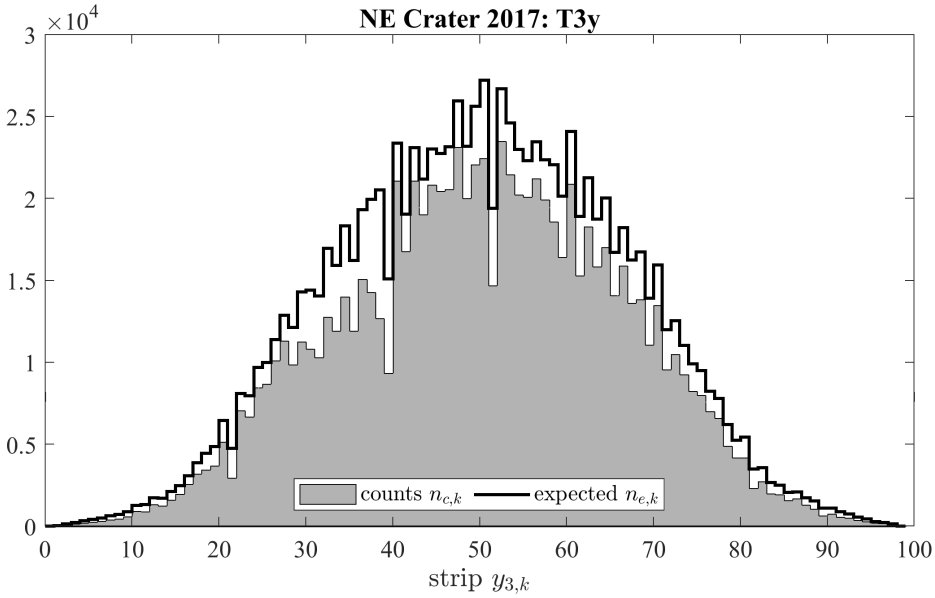
NE Crater 2017: T3y
×10^4
counts $n_{c,k}$
expected $n_{e,k}$
strip $y_{3,k}$

(a)

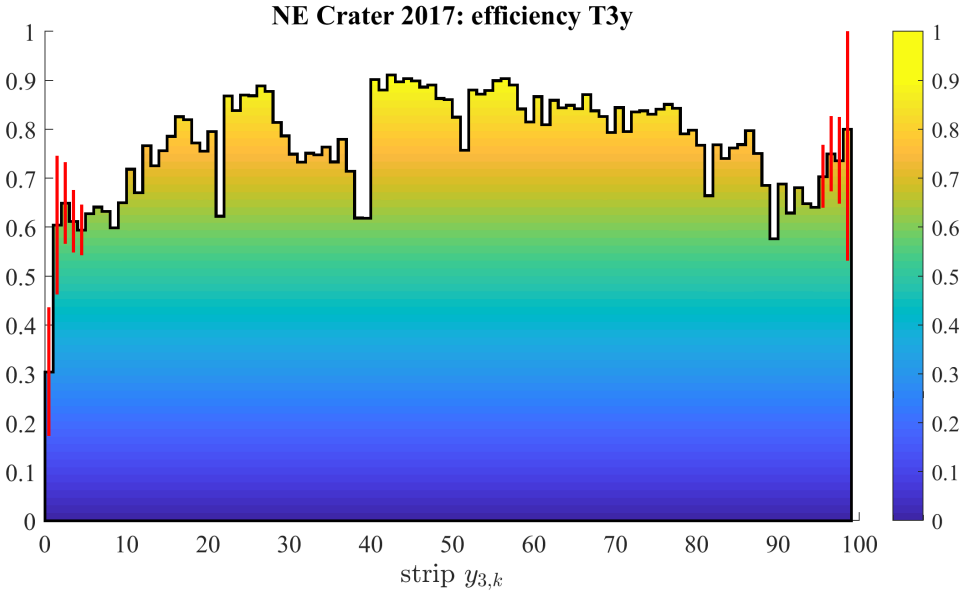
NE Crater 2017: efficiency T3y
strip $y_{3,k}$

(b)

Figure A.4

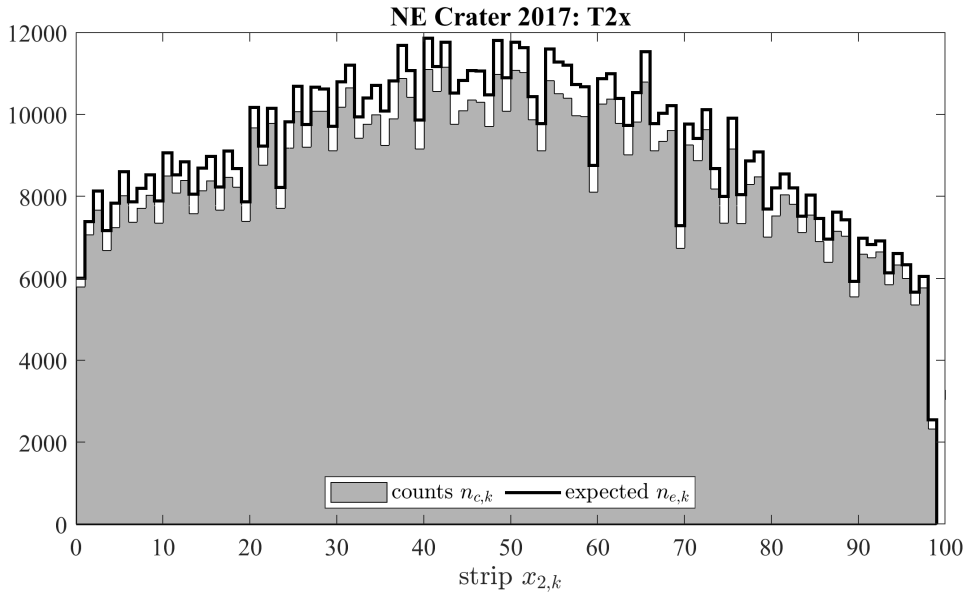
NE Crater 2017: T2x
12000
10000
8000
6000
4000
2000
0
counts $n_{c,k}$
expected $n_{e,k}$
0
10
20
30
40
50
60
70
80
90
100
strip $x_{2,k}$

(a)

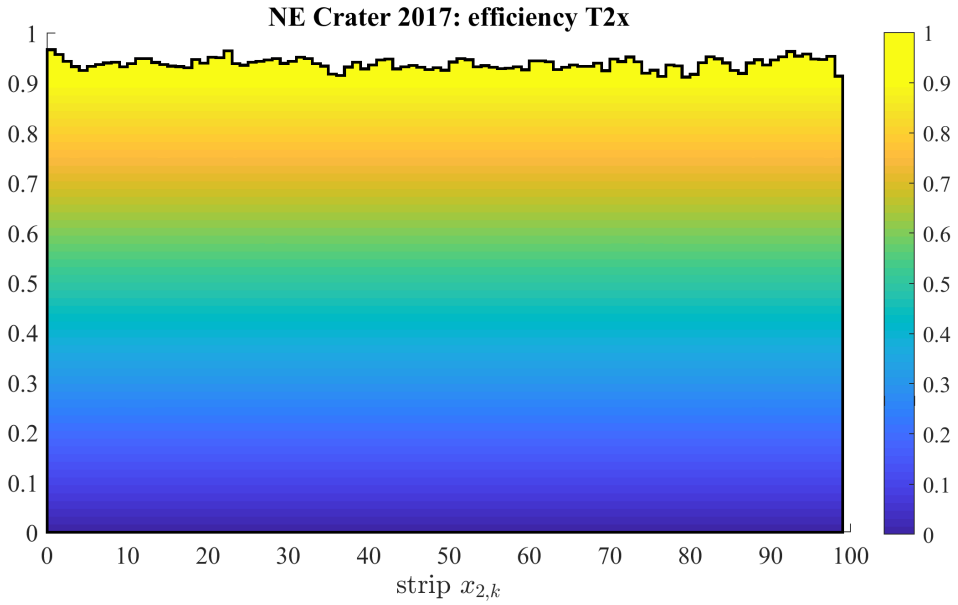
NE Crater 2017: efficiency T2x
1
0.9
0.8
0.7
0.6
0.5
0.4
0.3
0.2
0.1
0
0
10
20
30
40
50
60
70
80
90
100
strip $x_{2,k}$

(b)

Figure A.5

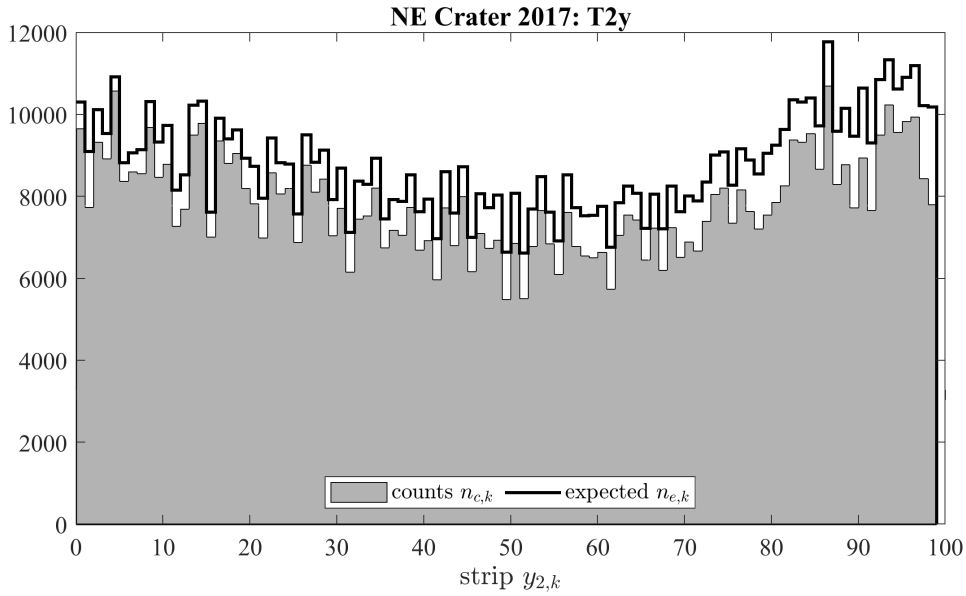
NE Crater 2017: T2y
12000
10000
8000
6000
4000
2000
0
counts $n_{c,k}$
expected $n_{e,k}$
0
10
20
30
40
50
60
70
80
90
100
strip $y_{2,k}$

(a)

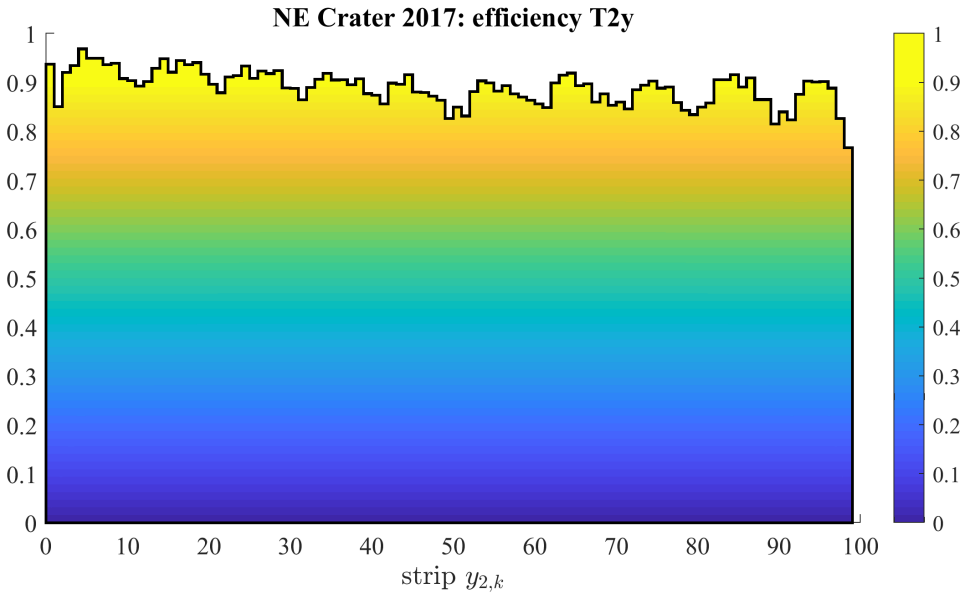
NE Crater 2017: efficiency T2y
1
0.9
0.8
0.7
0.6
0.5
0.4
0.3
0.2
0.1
0
0
10
20
30
40
50
60
70
80
90
100
strip $y_{2,k}$

(b)

Figure A.6

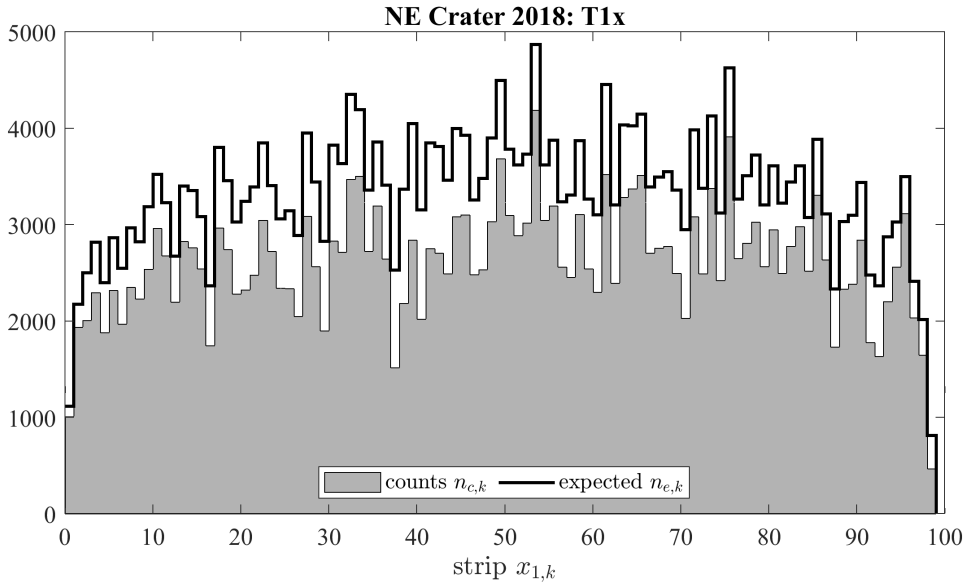
NE Crater 2018: T1x
5000
4000
3000
2000
1000
0
0
10
20
30
40
50
60
70
80
90
100
counts $n_{c,k}$
expected $n_{e,k}$
strip $x_{1,k}$

(a)

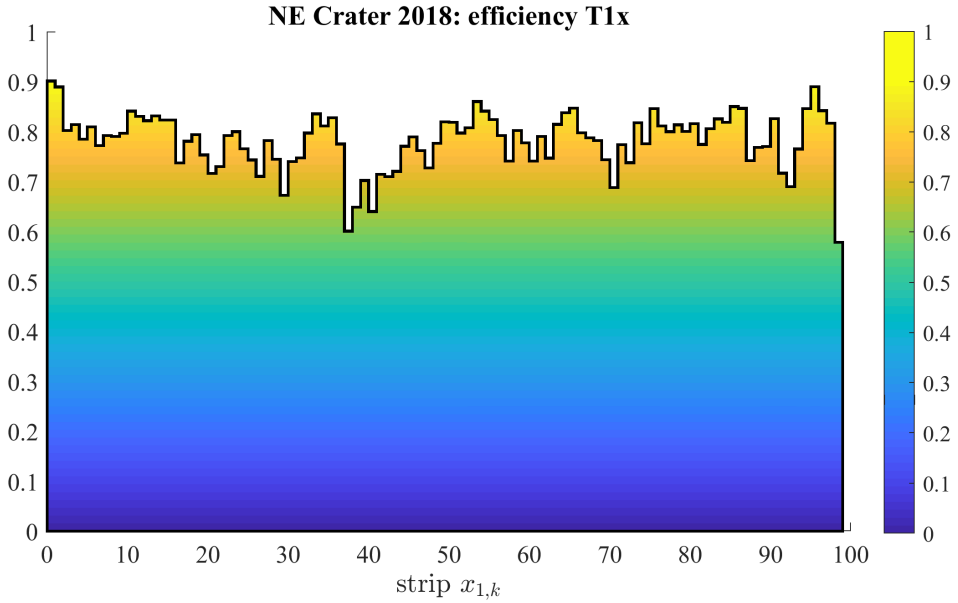
NE Crater 2018: efficiency T1x
1
0.9
0.8
0.7
0.6
0.5
0.4
0.3
0.2
0.1
0
0
10
20
30
40
50
60
70
80
90
100
strip $x_{1,k}$

(b)

Figure A.7

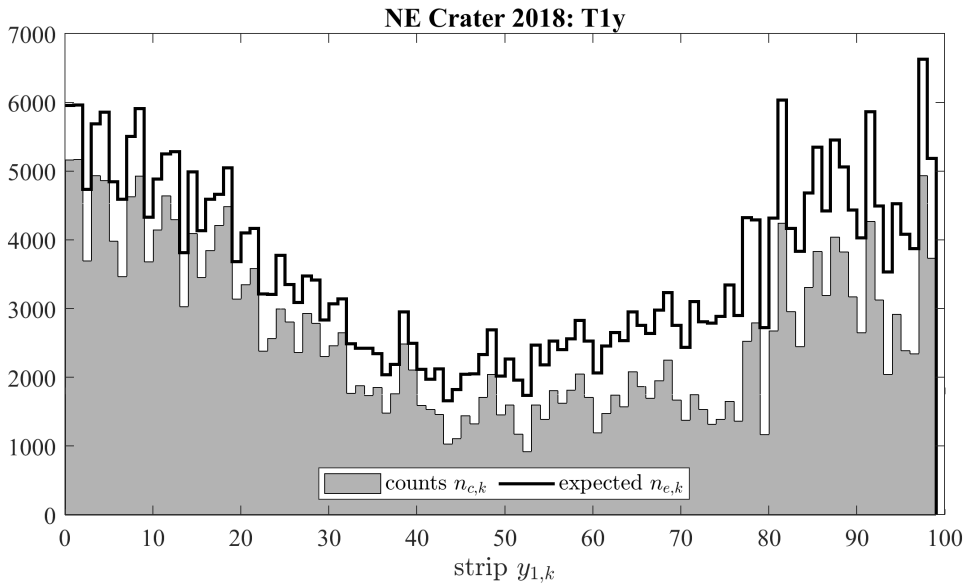
NE Crater 2018: T1y
7000
6000
5000
4000
3000
2000
1000
0
counts $n_{c,k}$
expected $n_{e,k}$
0 10 20 30 40 50 60 70 80 90 100
strip $y_{1,k}$

(a)

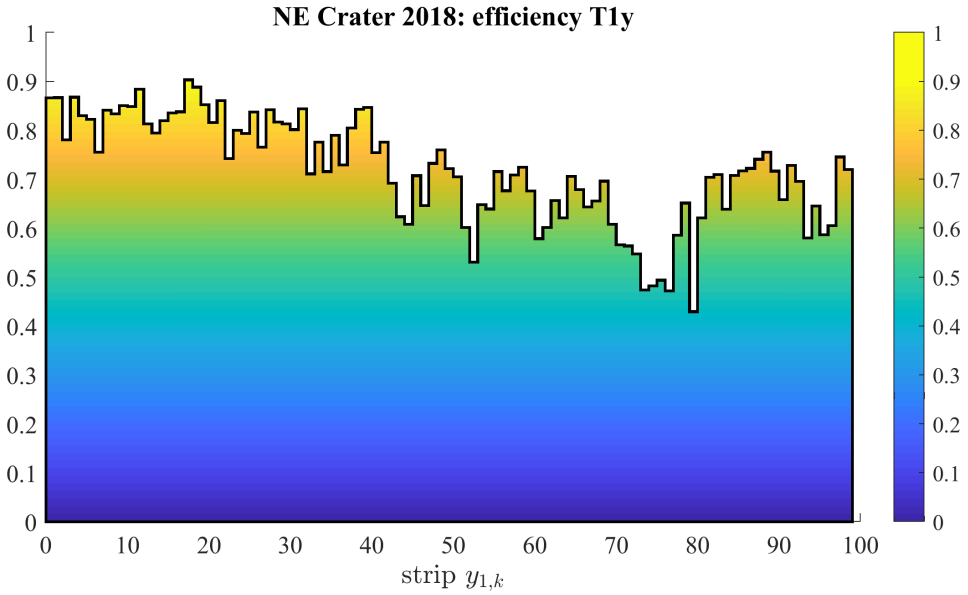
NE Crater 2018: efficiency T1y
1
0.9
0.8
0.7
0.6
0.5
0.4
0.3
0.2
0.1
0
0 10 20 30 40 50 60 70 80 90 100
strip $y_{1,k}$

(b)

Figure A.8

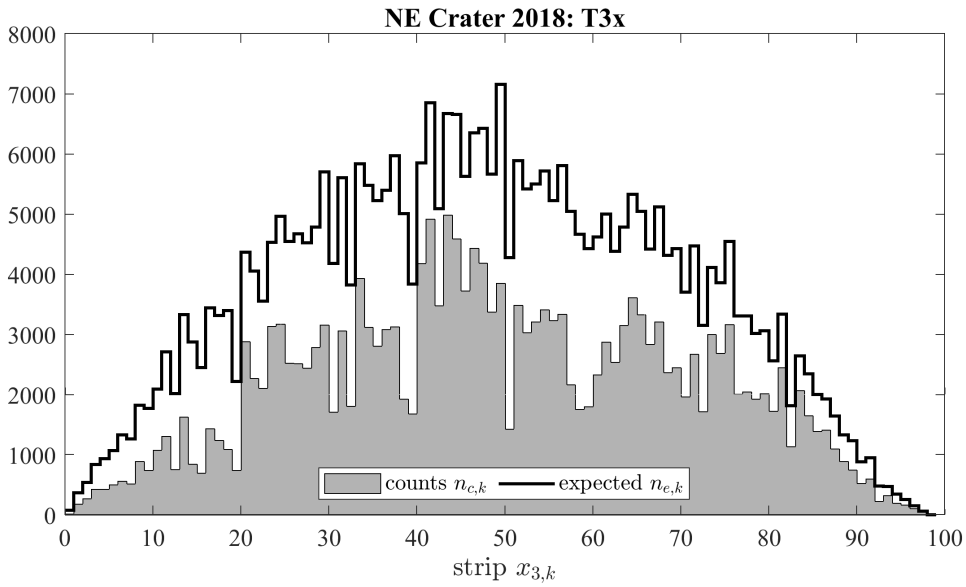
NE Crater 2018: T3x
8000
7000
6000
5000
4000
3000
2000
1000
0
0
10
20
30
40
50
60
70
80
90
100
counts $n_{c,k}$
expected $n_{e,k}$
strip $x_{3,k}$

(a)

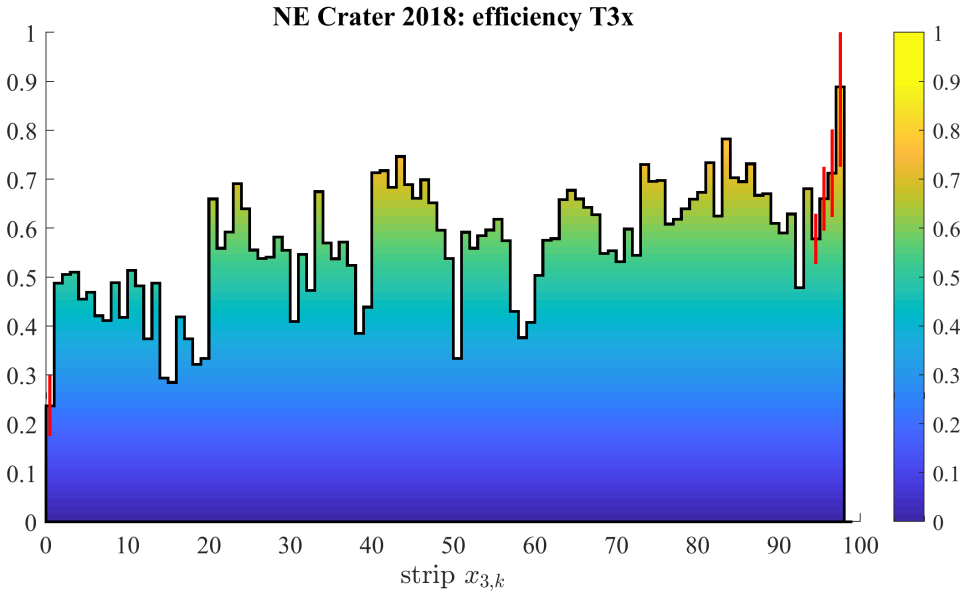
NE Crater 2018: efficiency T3x
1
0.9
0.8
0.7
0.6
0.5
0.4
0.3
0.2
0.1
0
0
10
20
30
40
50
60
70
80
90
100
strip $x_{3,k}$

(b)

Figure A.9

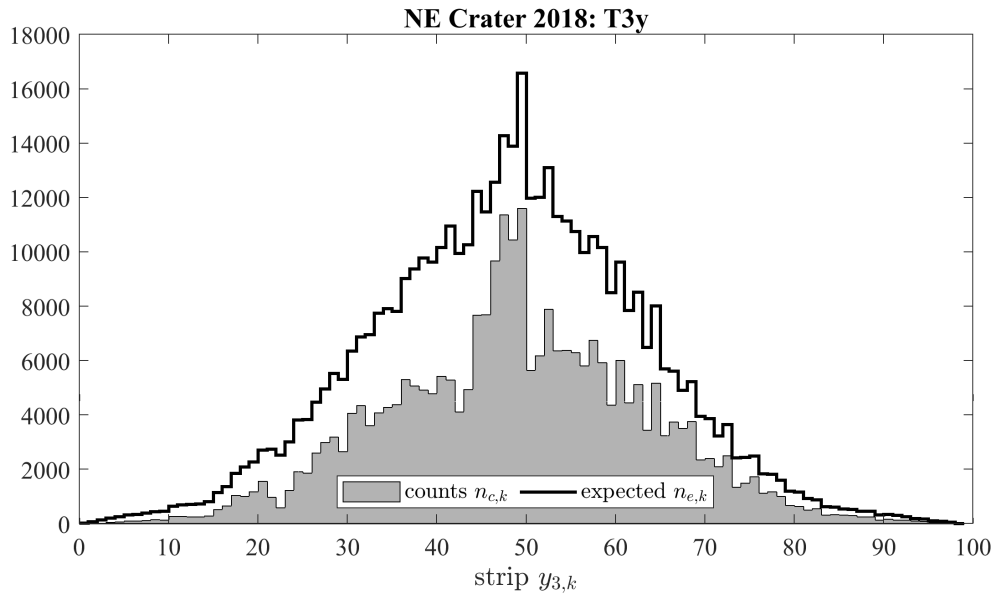

(a)

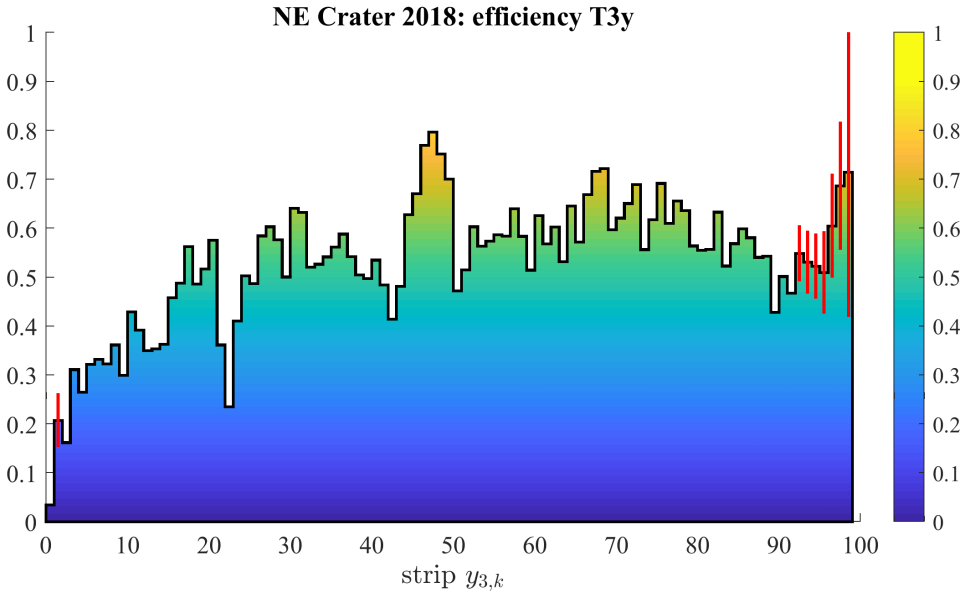

(b)

Figure A.10

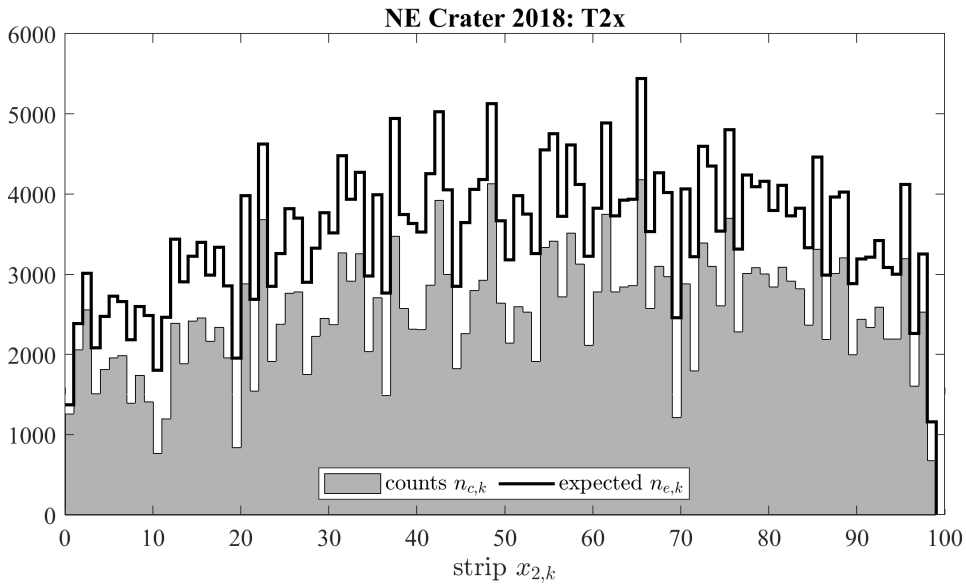

(a)

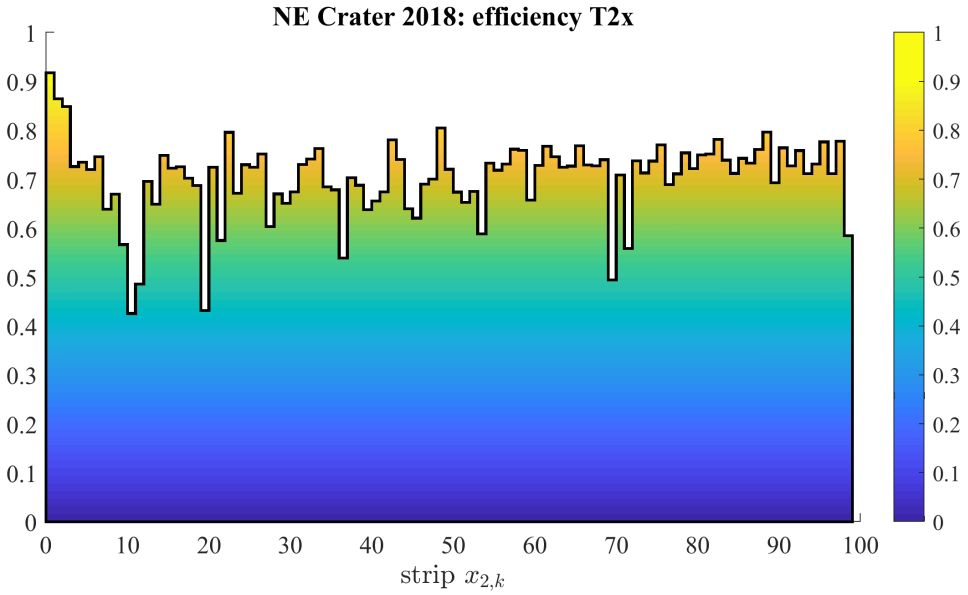

(b)

Figure A.11

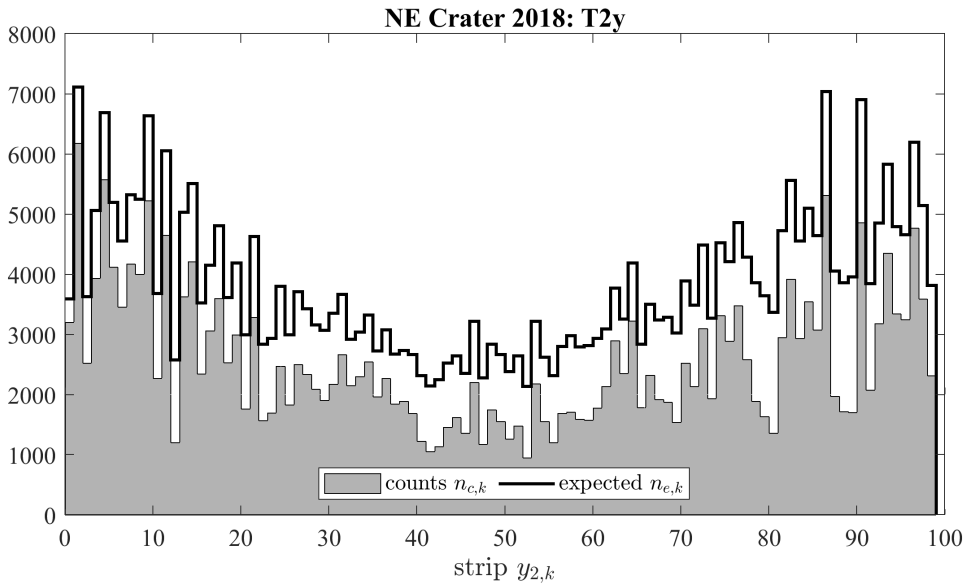

(a)

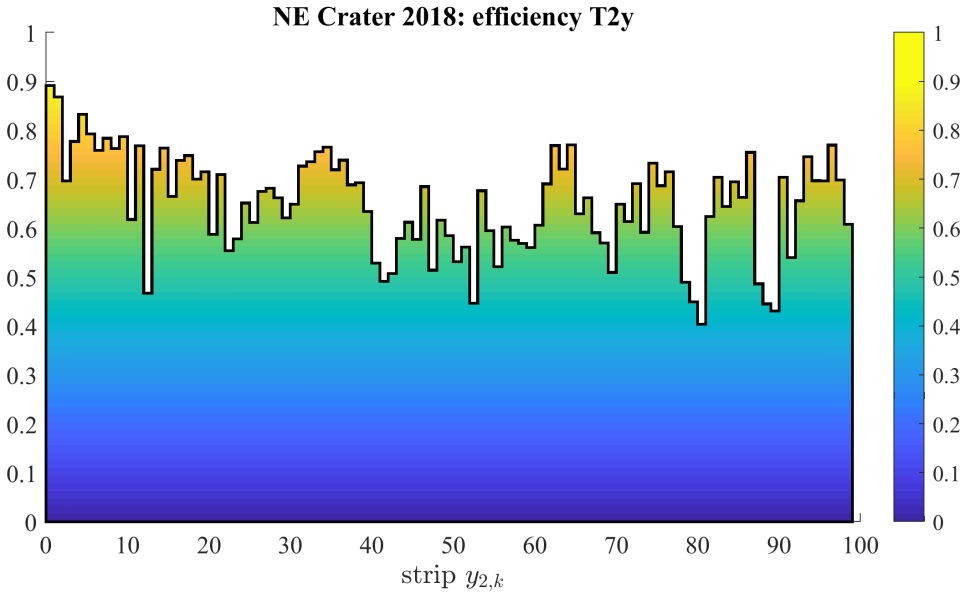

(b)

Figure A.12

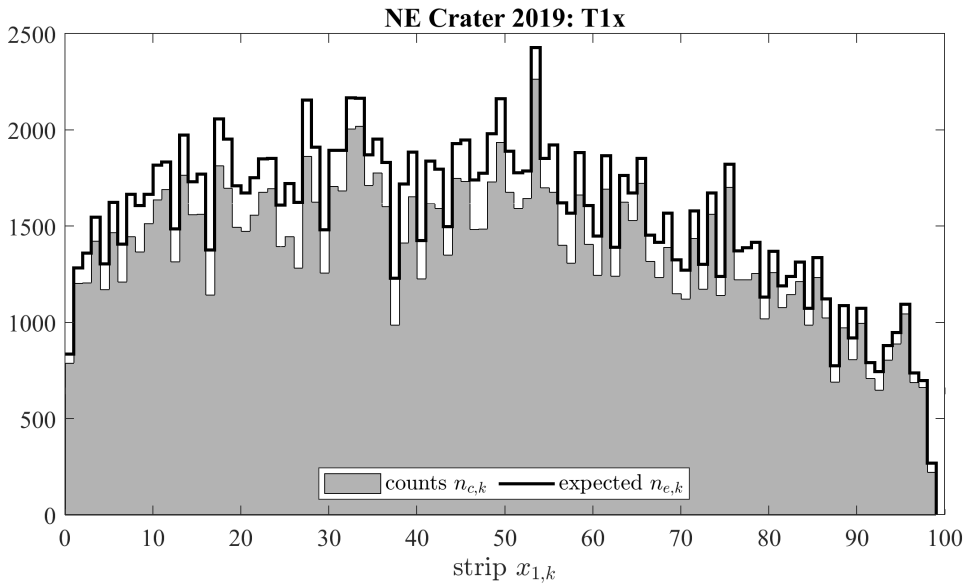

(a)

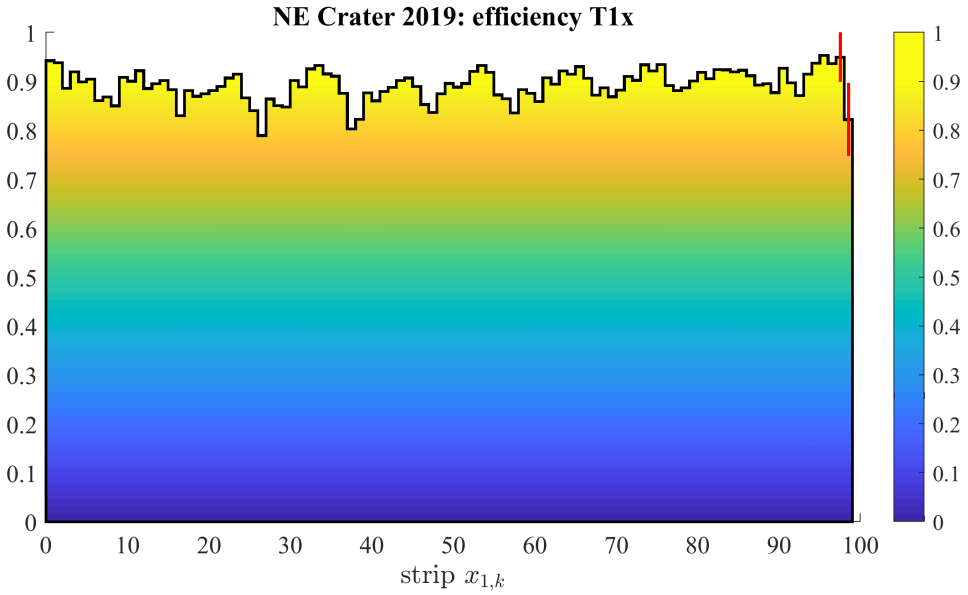

(b)

Figure A.13

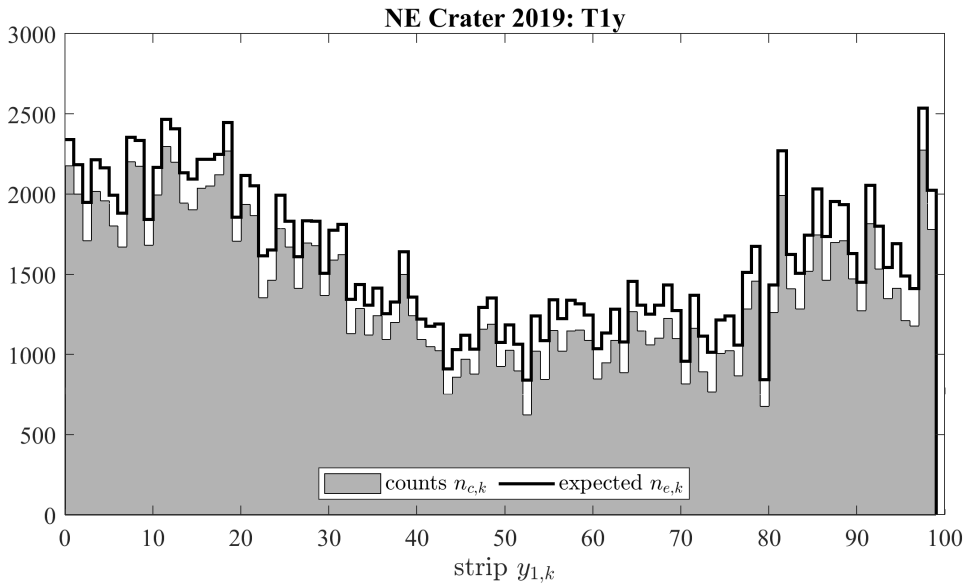

(a)

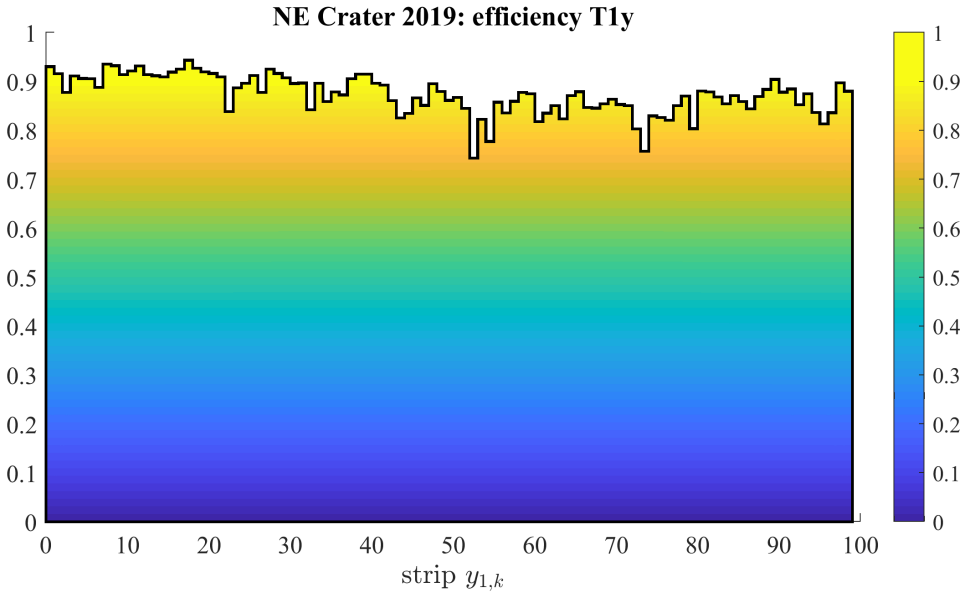

(b)

Figure A.14

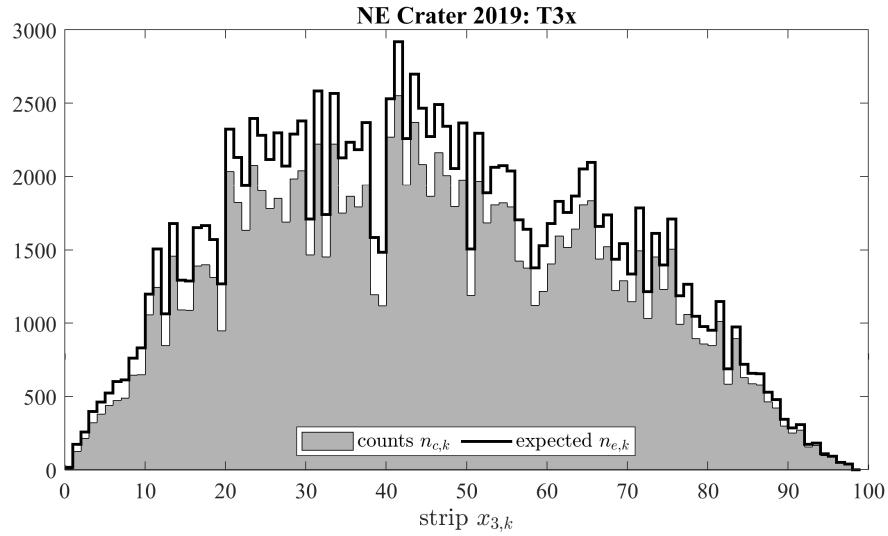

(a)

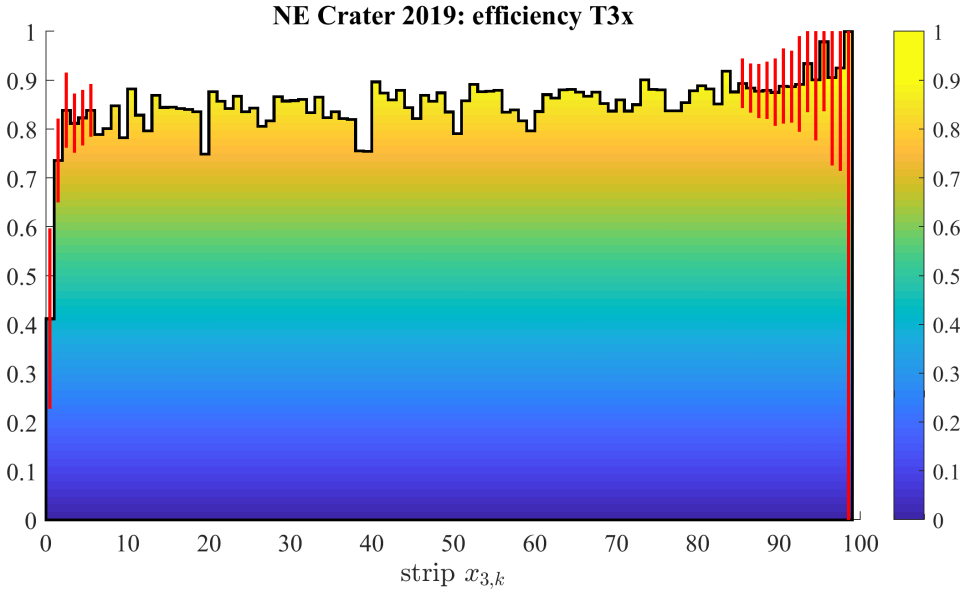

(b)

Figure A.15

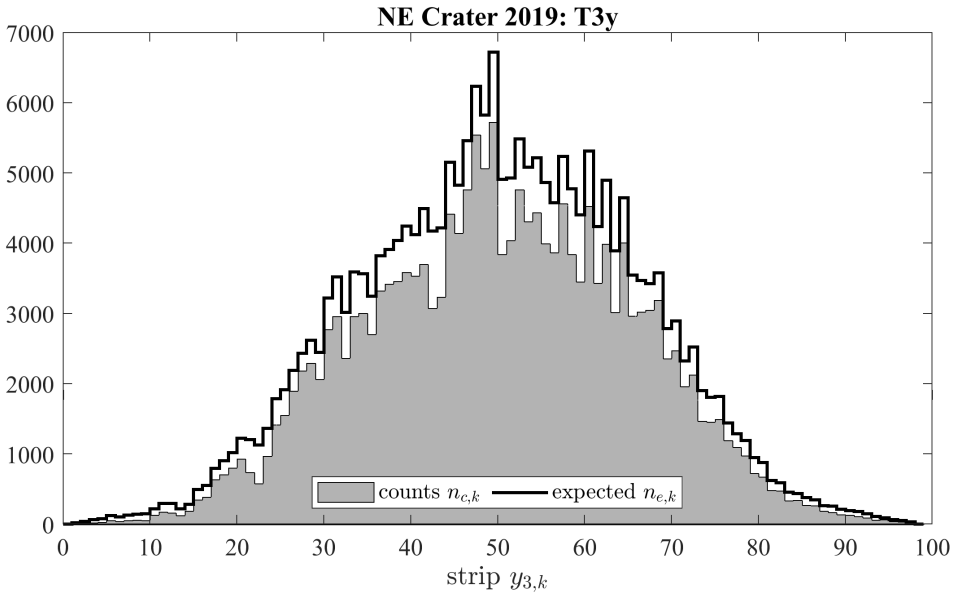

(a)

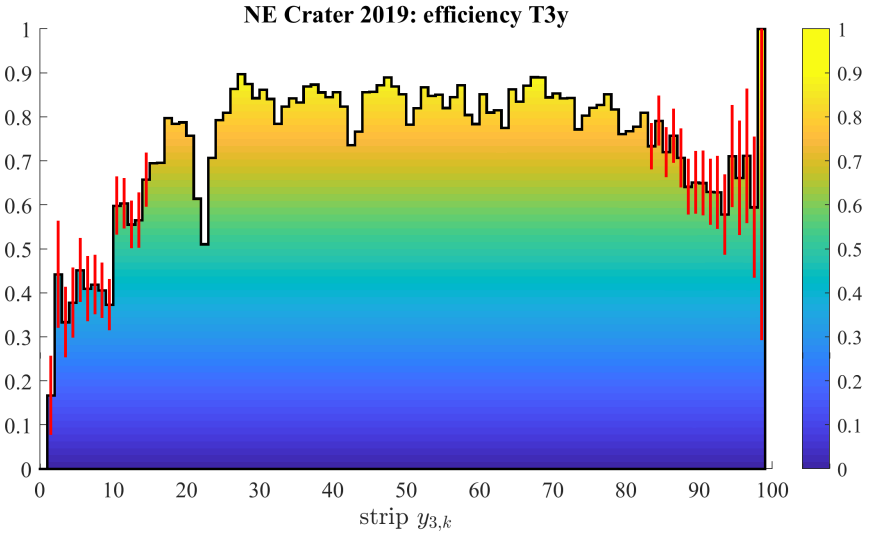

(b)

Figure A.16

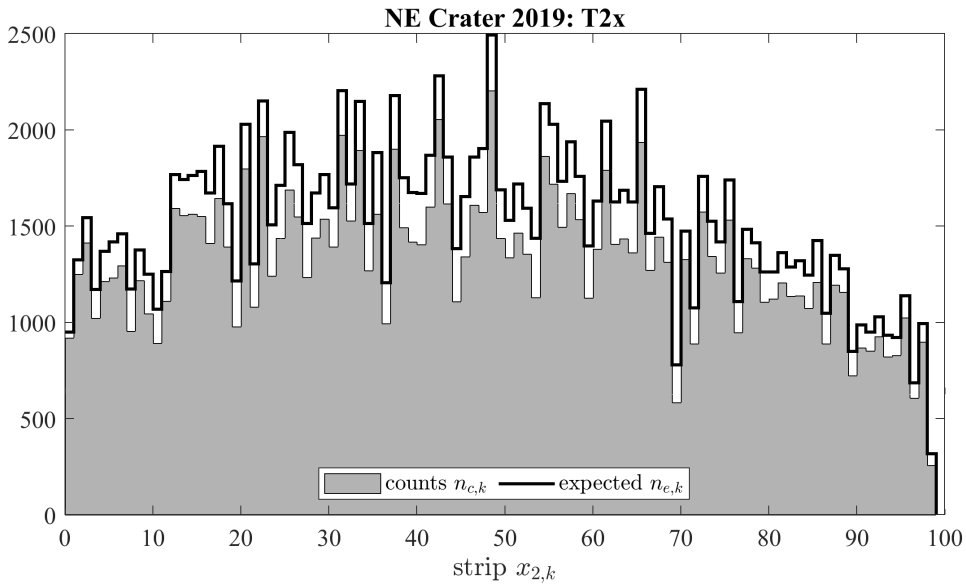

(a)

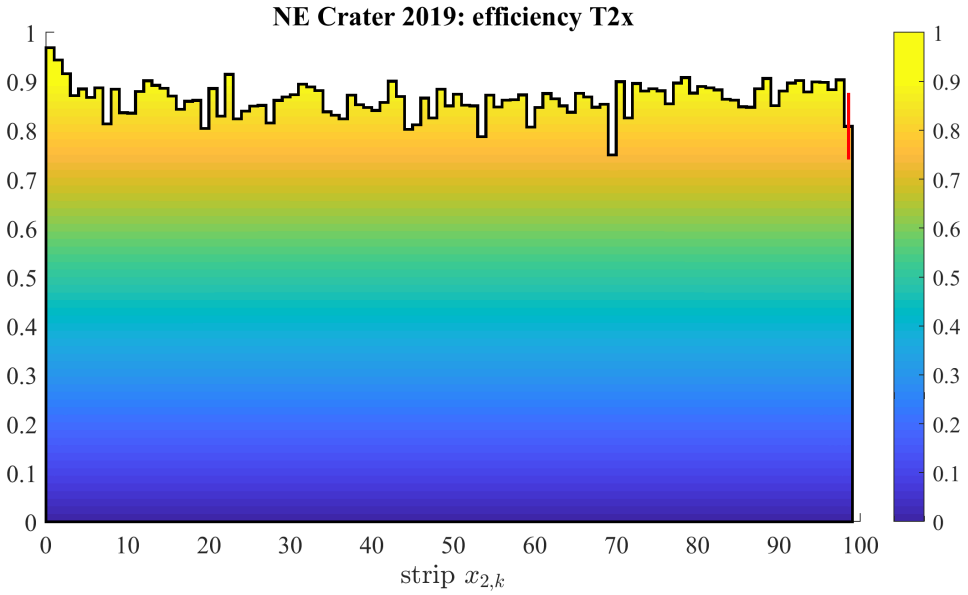

(b)

Figure A.17

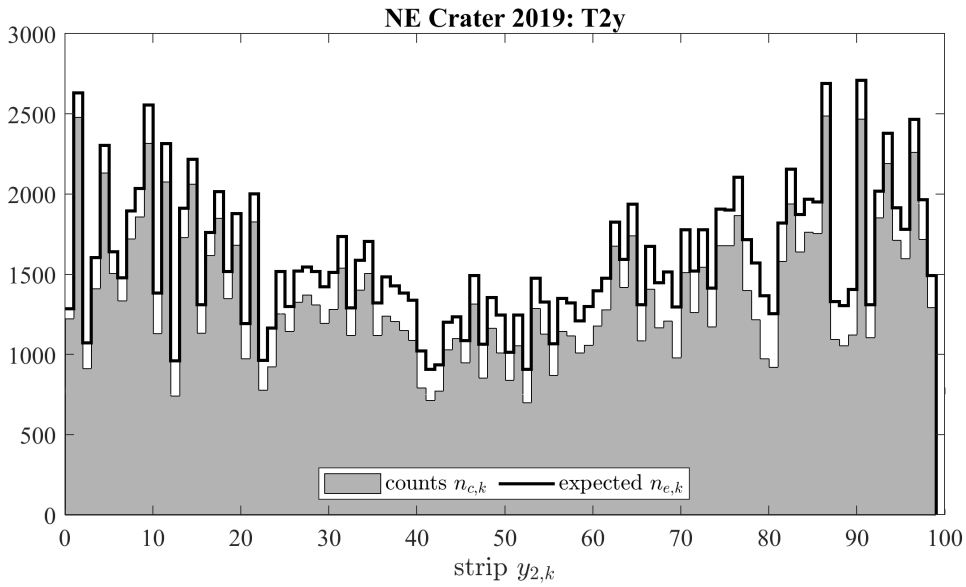

(a)

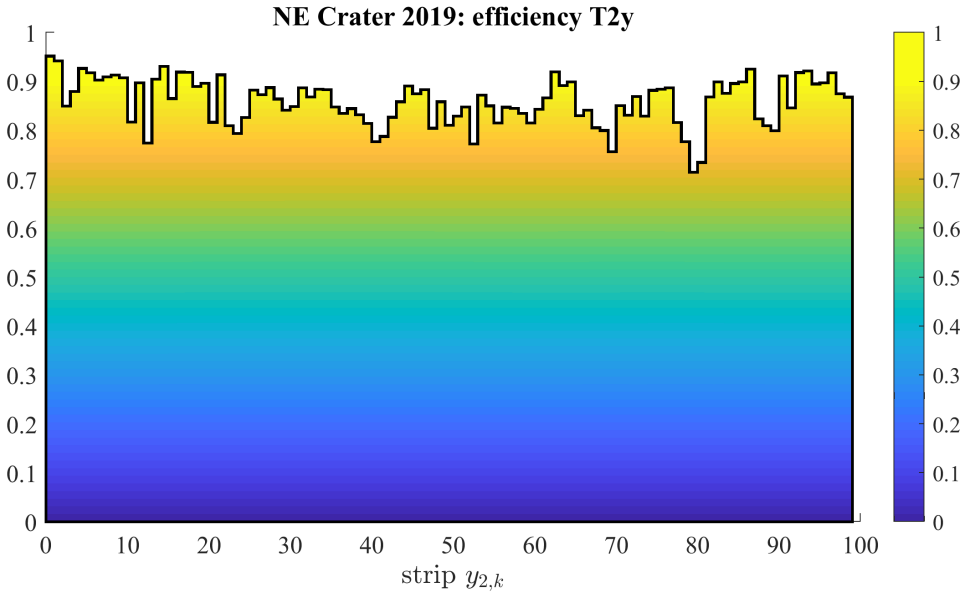

(b)

Figure A.18

Appendix B

Real acceptance distributions

Figures included in this appendix show the variations of angular acceptance distribution according to the efficiencies estimated for each data set. In particular:

- Figures B.1 to B.3 refer to corrected acceptance relative to NE Etna Crater measurement campaign of 2017;
- Figures B.4 to B.4 refer to corrected acceptance relative to NE Etna Crater measurement campaign of 2018;
- Figures B.7 to B.9 refer to corrected acceptance relative to NE Etna Crater measurement campaign of 2019.

Every Figure contains the theoretical acceptance $\mathcal{T}$ in the top panel in order to make clearer the comparison with corrected acceptance $\mathcal{T}(\bar{\varepsilon})$. Each of the three real distributions is shown from different perspective views.

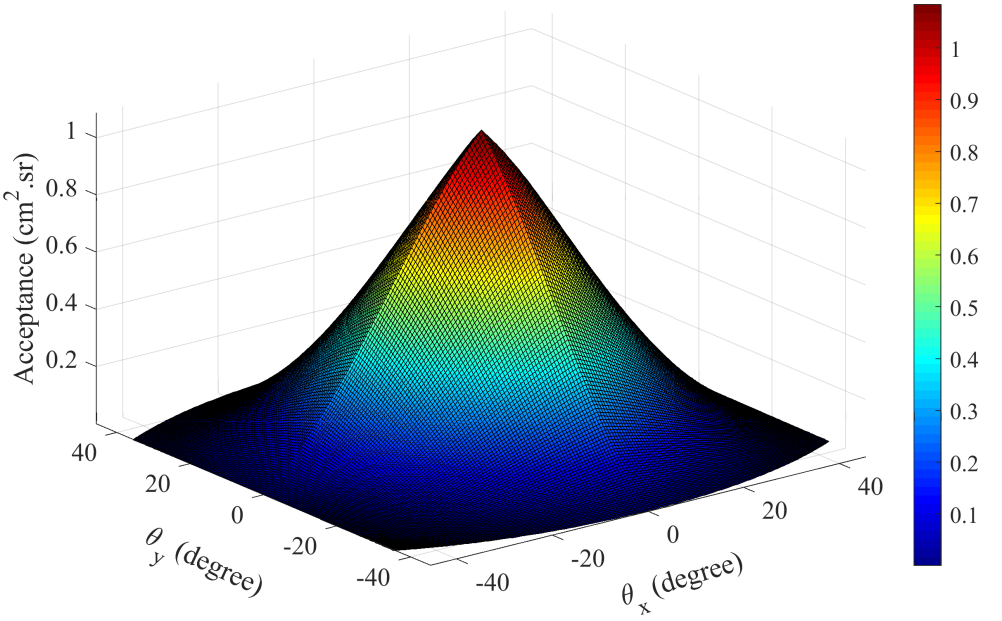

(a) $\mathcal{T}$.

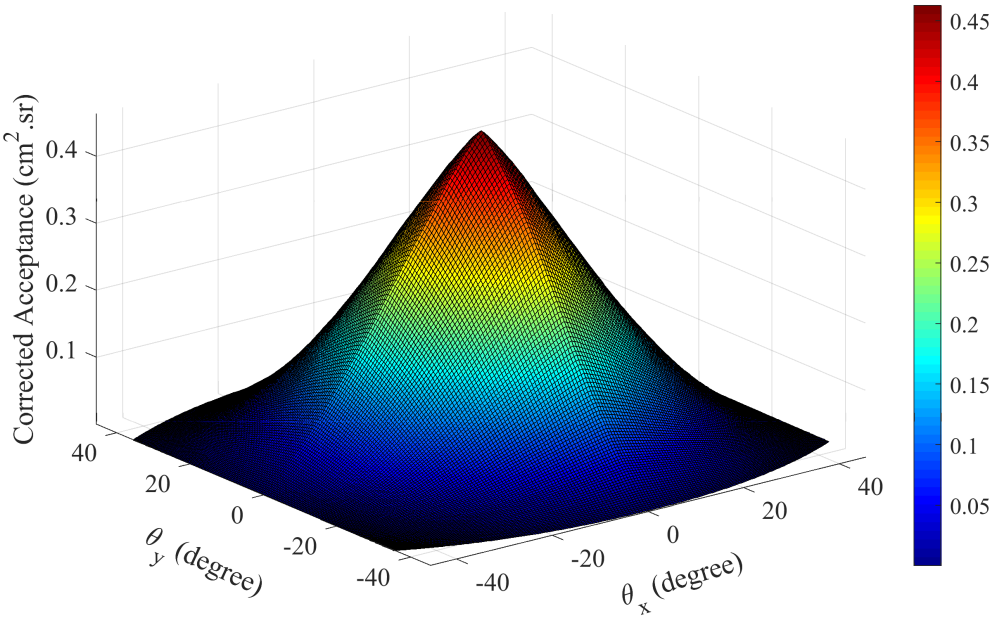

(b) $\mathcal{T}(\bar{\varepsilon})$.

Figure B.1: $\mathcal{T}(\bar{\varepsilon})$ refers to the measurement campaign of 2017 at North-East Etna crater.

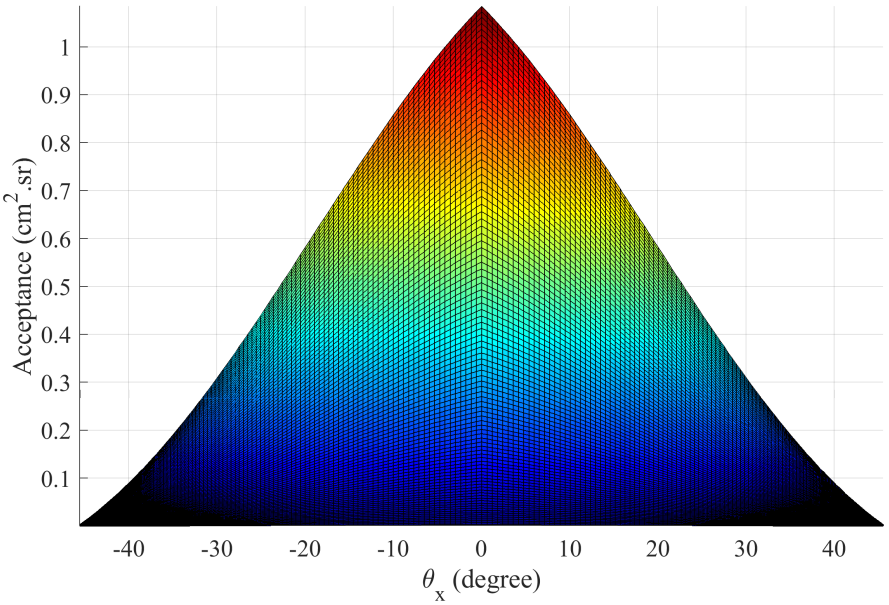

(a) $\mathcal{T}$.

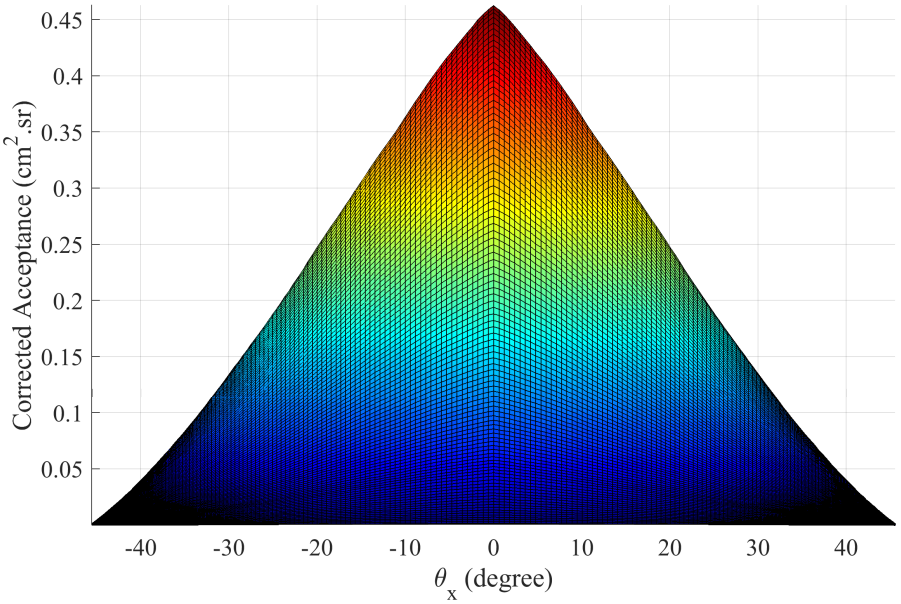

(b) $\mathcal{T}(\bar{\varepsilon})$.

Figure B.2: $\mathcal{T}(\bar{\varepsilon})$ refers to the measurement campaign of 2017 at North-East Etna crater.

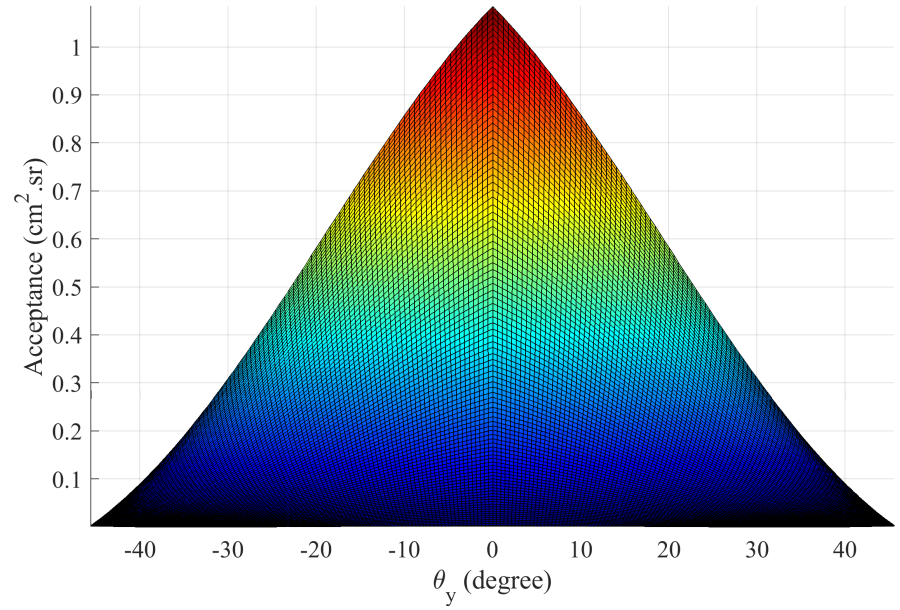

(a) $\mathcal{T}$.

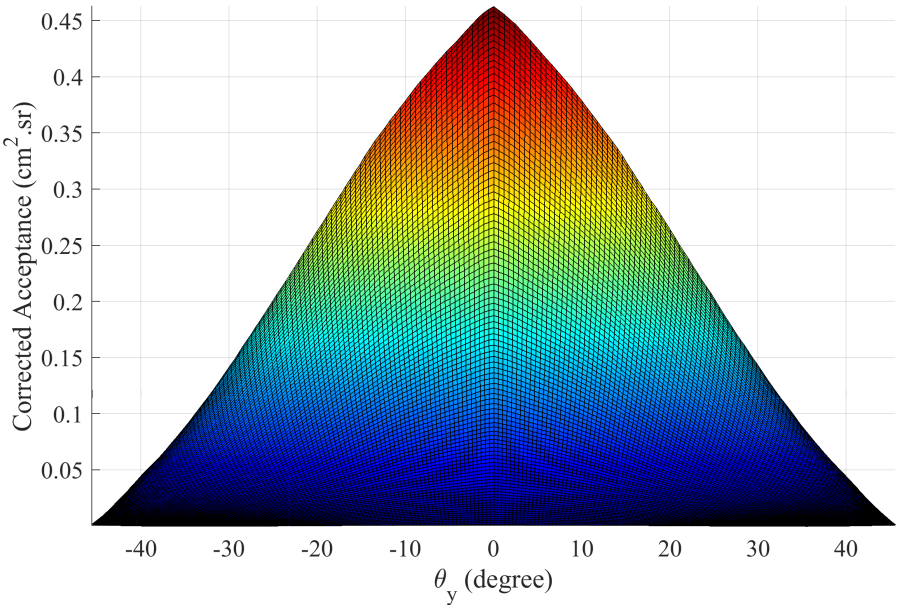

(b) $\mathcal{T}(\bar{\varepsilon})$.

Figure B.3: $\mathcal{T}(\bar{\varepsilon})$ refers to the measurement campaign of 2017 at North-East Etna crater.

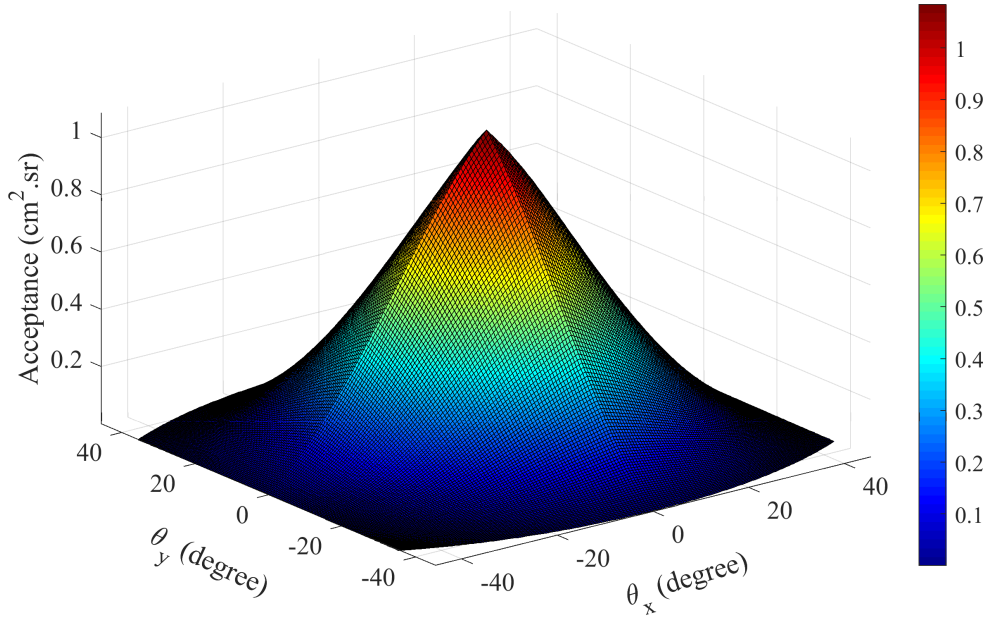

(a) $\mathcal{T}$.

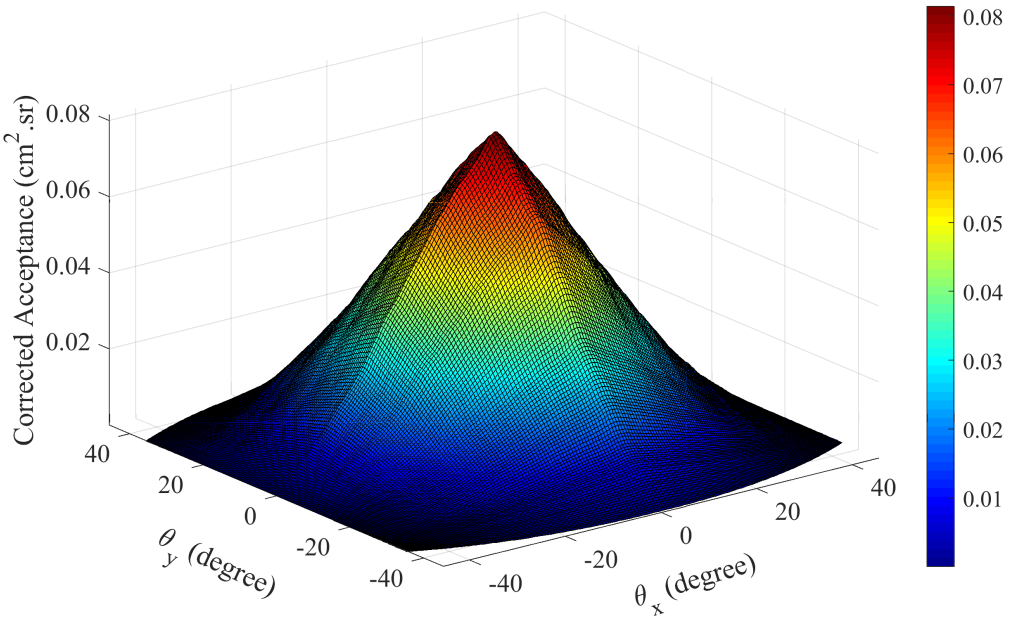

(b) $\mathcal{T}(\bar{\varepsilon})$.

Figure B.4: $\mathcal{T}(\bar{\varepsilon})$ refers to the measurement campaign of 2018 at North-East Etna crater.

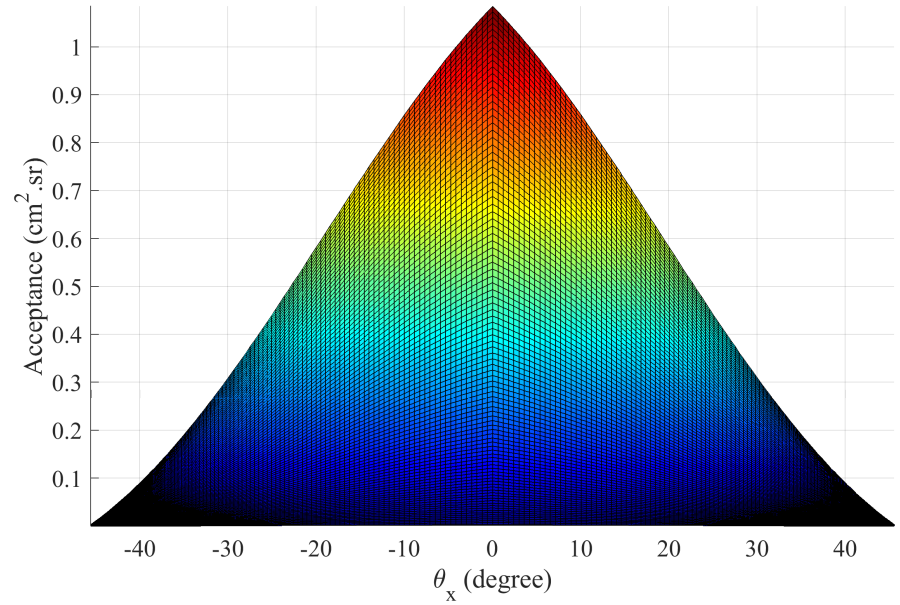

(a) $\mathcal{T}$.

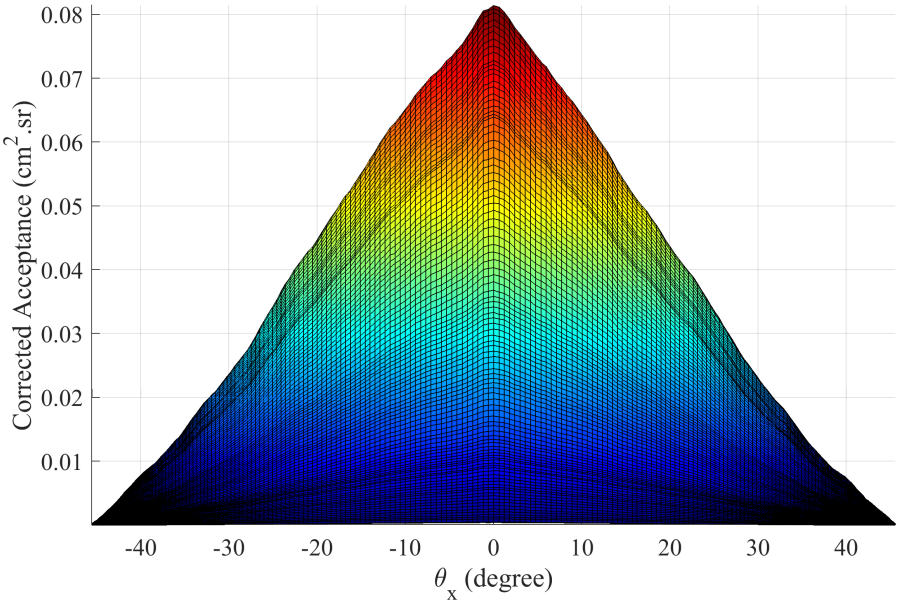

(b) $\mathcal{T}(\bar{\varepsilon})$.

Figure B.5: $\mathcal{T}(\bar{\varepsilon})$ refers to the measurement campaign of 2018 at North-East Etna crater.

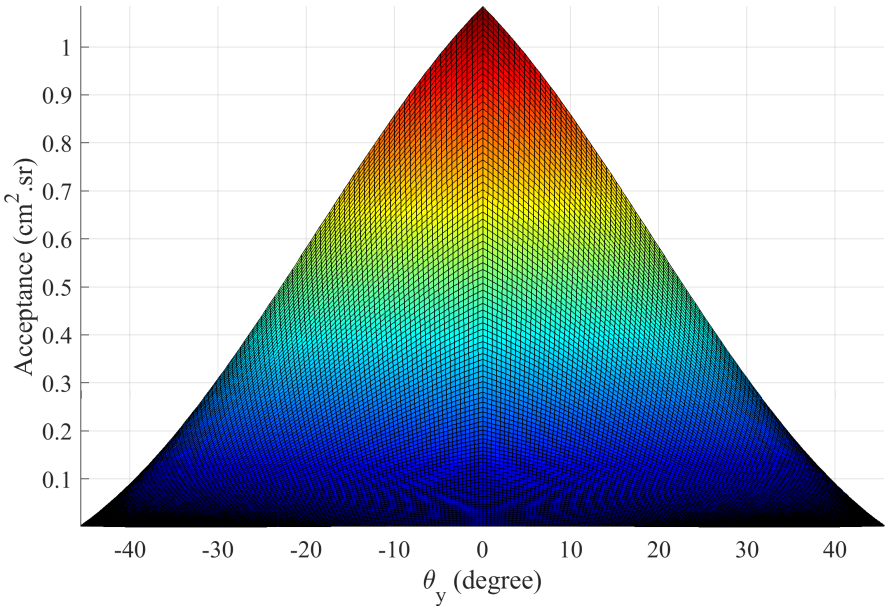

(a) $\mathcal{T}$.

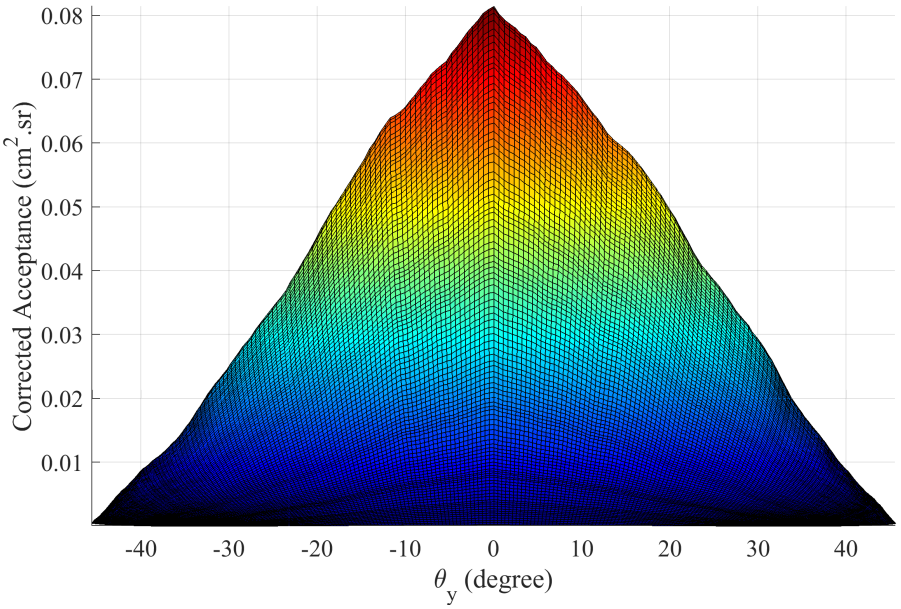

(b) $\mathcal{T}(\bar{\varepsilon})$.

Figure B.6: $\mathcal{T}(\bar{\varepsilon})$ refers to the measurement campaign of 2018 at North-East Etna crater.

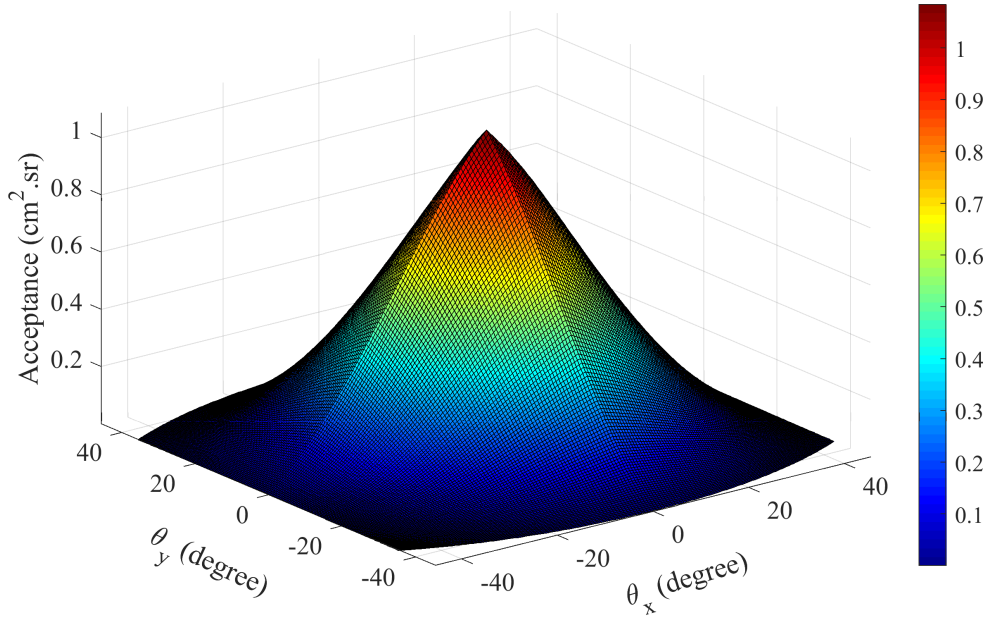

(a) $\mathcal{T}$.

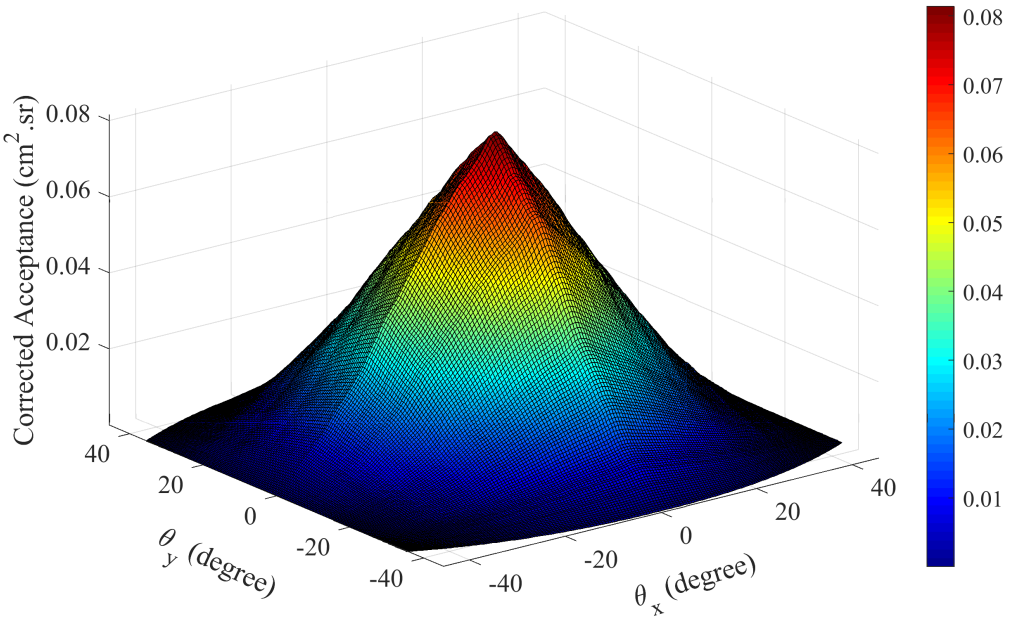

(b) $\mathcal{T}(\bar{\varepsilon})$.

Figure B.7: $\mathcal{T}(\bar{\varepsilon})$ refers to the measurement campaign of 2019 at North-East Etna crater.

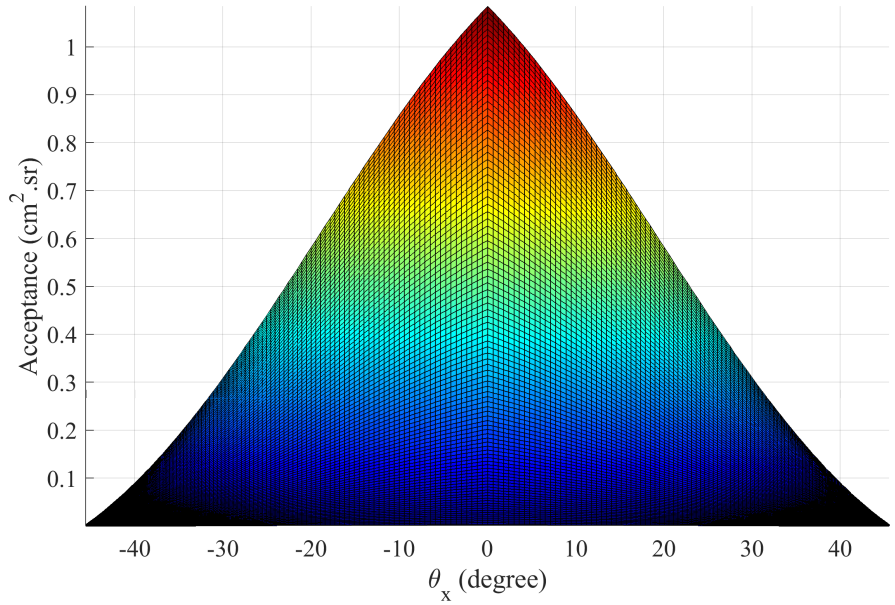

(a) $\mathcal{T}$.

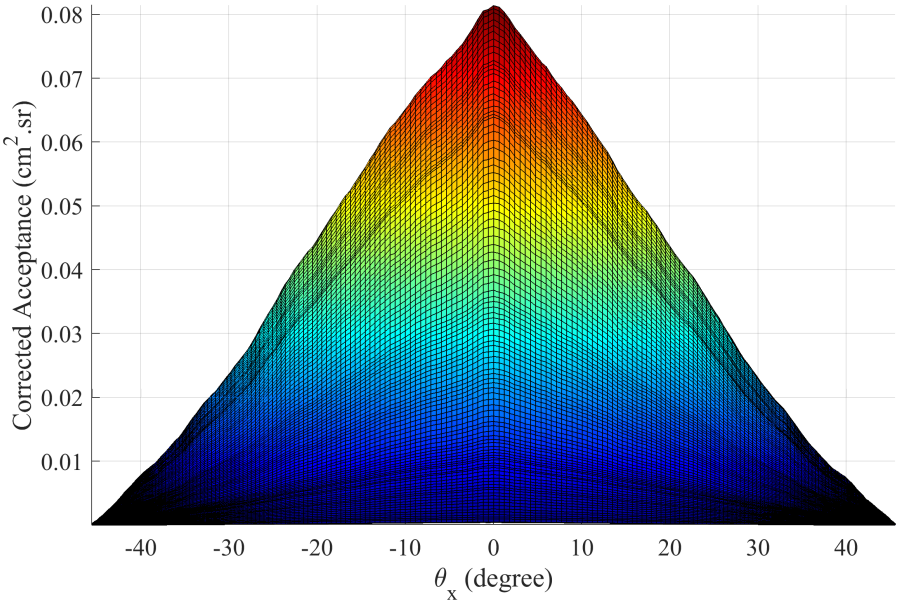

(b) $\mathcal{T}(\bar{\varepsilon})$.

Figure B.8: $\mathcal{T}(\bar{\varepsilon})$ refers to the measurement campaign of 2019 at North-East Etna crater.

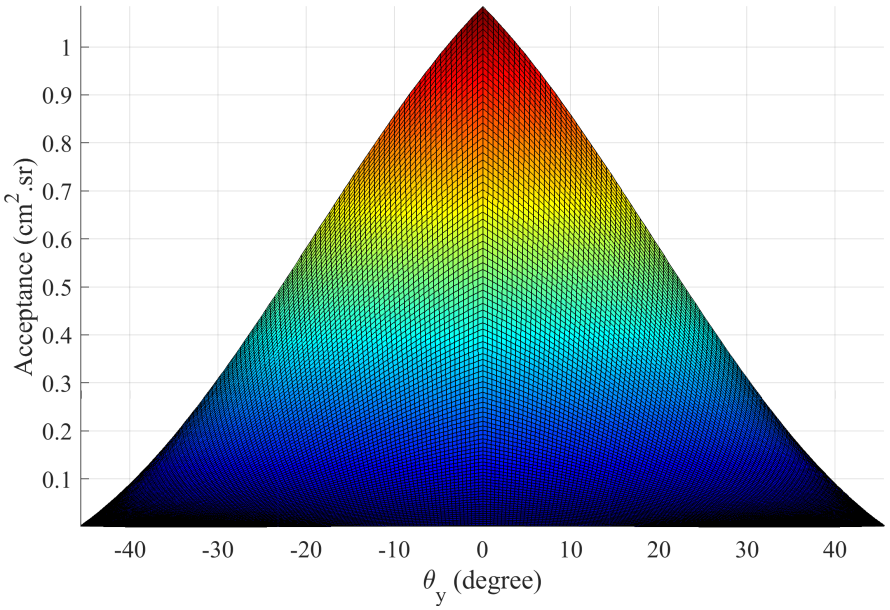

(a) $\mathcal{T}$.

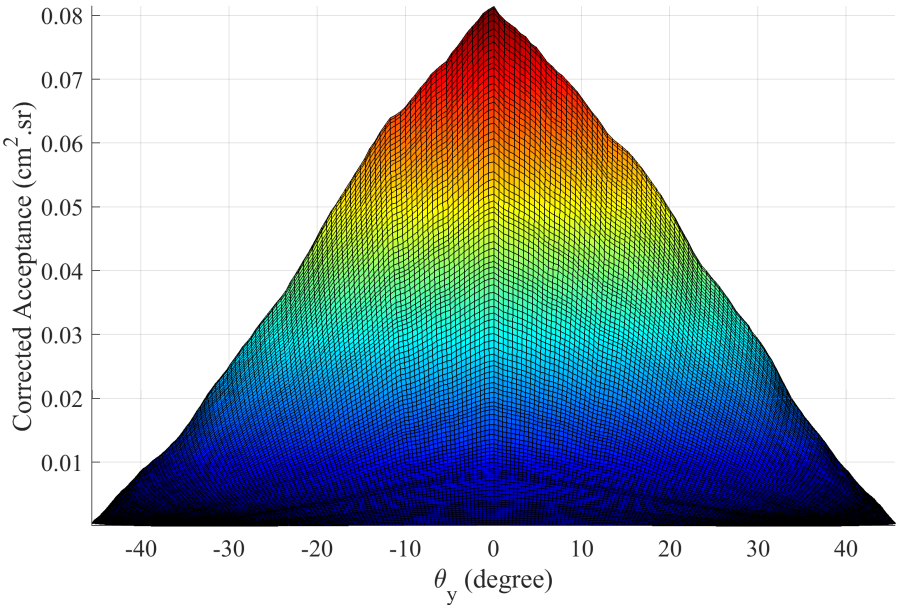

(b) $\mathcal{T}(\bar{\varepsilon})$.

Figure B.9: $\mathcal{T}(\bar{\varepsilon})$ refers to the measurement campaign of 2019 at North-East Etna crater.

Bibliography

[1] Seth H. Neddermeyer and Carl D. Anderson, Phys. Rev. **51**, 884 (1937).

[2] J. C. Street and E. C. Stevenson, Phys. Rev. **52**, 1003 (1937).

[3] E. P. George, Commonwealth Engineer **455**, (1955).

[4] L. W. Alvarez et al., Science **167**, 832 (1970).

[5] K. Morishima et al., Nature **552**, 386 (2017).

[6] D. Lo Presti et al., Nuclear Instruments and Methods in Physics Research Section A: Accelerators, Spectrometers, Detectors and Associated Equipment **904**, 195 (2018).

[7] C. Ferlito, Earth-Science Reviews **177**, 14 (2018).

[8] D. Dzurisin, *Volcano Deformation: New Geodetic Monitoring Techniques*, *Geophysical Sciences* (Springer-Verlag, Berlin Heidelberg, 2007).

[9] B. A. Chouet and R. S. Matoza, Journal of Volcanology and Geothermal Research **252**, 108 (2013).

[10] D. Carbone et al., Earth-Science Reviews **169**, 146 (2017).

[11] K. Jourde, D. Gibert, and J. Marteau, Geoscientific Instrumentation, Methods and Data Systems **4**, 177 (2015).

[12] C. Patrignani, Chinese Physics C **40**, 100001 (2016).

[13] Malcolm S. Longair, *High Energy Astrophysics* (Cambridge University Press, ADDRESS, 2011), google-Books-ID: KGe3FVbDNk4C.

[14] R. Bellotti et al., Phys. Rev. D **53**, 35 (1996).

[15] R. Bellotti et al., Phys. Rev. D **60**, 052002 (1999).

[16] M. Boezio et al., Phys. Rev. D **62**, 032007 (2000).

[17] M. Boezio et al., Phys. Rev. D **67**, 072003 (2003).

[18] S. Coutu and et al., Phys. Rev. D **62**, 032001 (2000).

[19] S. Haino and et al. (BESS Collab.), Physics Letters B **594**, 35 (2004).

[20] T. K. Gaisser and T. Stanev, Physics Letters B **592**, 228 (2004).

[21] Peter K.F. Grieder, *Cosmic Rays at Earth* (Elsevier, ADDRESS, 2001).

[22] M. P. De Pascale et al., Journal of Geophysical Research: Space Physics **98**, 3501 (1993).

[23] O. C. Allkofer, K. Carstensen, and W. D. Dau, Physics Letters B **36**, 425 (1971).

[24] O. C. Allkofer, K. Carstensen, W. D. Dau, E. Fahnders, W. Heinrich, and H. Jokioch, (1971).

[25] B. C. Rastin, J. Phys. G: Nucl. Phys. **10**, 1609 (1984).

[26] C. A. Ayre et al., J. Phys. G: Nucl. Phys. **1**, 584 (1975).

[27] J. Kremer et al., Phys. Rev. Lett. **83**, 4241 (1999).

[28] H. Jokisch et al., Phys. Rev. D **19**, 1368 (1979).

[29] Vivek Agrawal, T. K. Gaisser, Paolo Lipari, and Todor Stanev, Physical Review D **53**, 1314 (1996).

[30] M. G. Thompson, Edited by AW Wolfendale, Published by The Institute of Physics, London (1973).

[31] P. J. Hayman and A. W. Wolfendale, Proc. Phys. Soc. **80**, 710 (1962).

[32] A. Tang et al., Phys. Rev. D **74**, 053007 (2006).

[33] M. Ambrosio and et al., Astroparticle Physics **7**, 109 (1997).

[34] Serap Tilav and et al., arXiv:1001.0776 [astro-ph, physics:physics] (2010), arXiv: 1001.0776.

[35] F. Riggi et al., Nuclear Instruments and Methods in Physics Research Section A: Accelerators, Spectrometers, Detectors and Associated Equipment **912**, 16 (2018).

[36] K. Nagamine, *Introductory Muon Science* (Cambridge University Press, Cambridge, 2003).

[37] D. E. Groom, N. V. Mokhov, and S. I. Striganov, Atomic Data and Nuclear Data Tables **78**, 183 (2001).

[38] K Nagamine et al., Nuclear Instruments and Methods in Physics Research Section A: Accelerators, Spectrometers, Detectors and Associated Equipment **356**, 585 (1995).

[39] H. Tanaka et al., Nuclear Instruments and Methods in Physics Research Section A: Accelerators, Spectrometers, Detectors and Associated Equipment **507**, 657 (2003).

[40] H. K. M. Tanaka et al., Nuclear Instruments and Methods in Physics Research Section A: Accelerators, Spectrometers, Detectors and Associated Equipment **555**, 164 (2005).

[41] H. K. M. Tanaka, T. Nakano, S. Takahashi, J. Yoshida, and K. Niwa, Nuclear Instruments and Methods in Physics Research Section A: Accelerators, Spectrometers, Detectors and Associated Equipment **575**, 489 (2007).

[42] H. K. M. Tanaka et al., Earth and Planetary Science Letters **263**, 104 (2007).

[43] H. K. M. Tanaka et al., Geophysical Research Letters **34**, (2007).

[44] D. Gibert et al., Earth, Planets and Space **62**, 153 (2010).

[45] N. Lesparre et al., Geophysical Journal International **183**, 1348 (2010).

[46] N. Lesparre et al., Geoscientific Instrumentation, Methods and Data Systems **1**, 33 (2012).

[47] J. Marteau et al., Nuclear Instruments and Methods in Physics Research Section A: Accelerators, Spectrometers, Detectors and Associated Equipment **695**, 23 (2012).

[48] K. Jourde et al., Geophysical Research Letters **40**, 6334 (2013).

[49] R. Nishiyama et al., Journal of Geophysical Research: Solid Earth **119**, 699 (2014).

[50] C. Cârloganu et al., Geoscientific Instrumentation, Methods and Data Systems **2**, 55 (2013).

[51] A. Portal et al., Geoscientific Instrumentation, Methods and Data Systems **2**, 47 (2013).

[52] F. Ambrosino et al., Journal of Geophysical Research: Solid Earth **120**, 7290 (2015).

[53] G. Ambrosi et al., Nuclear Instruments and Methods in Physics Research Section A: Accelerators, Spectrometers, Detectors and Associated Equipment **628**, 120 (2011).

[54] F. Ambrosino et al., J. Inst. **9**, C02029 (2014).

[55] G. Saracino et al., Annals of Geophysics **60**, 0103 (2017).

[56] G. G. Barnaföldi et al., Nuclear Instruments and Methods in Physics Research Section A: Accelerators, Spectrometers, Detectors and Associated Equipment **689**, 60 (2012).

[57] D. Varga et al., High Efficiency Gaseous Tracking Detector for Cosmic Muon Radiography, 2016.

[58] L. Oláh et al., Scientific Reports **8**, 3207 (2018).

[59] Valeri Tioukov et al., Scientific Reports **9**, 6695 (2019).

[60] D. Beznosko, A. Bross, A. Dyshkant, and P.-V. Rykalin, in *IEEE Symposium Conference Record Nuclear Science 2004.* (PUBLISHER, ADDRESS, 2004), Vol. 2, pp. 790–793 Vol. 2.

[61] Scintillating Fiber | Saint-Gobain Crystals.

[62] G. Gallo and et al., J. Inst. **11**, C11014 (2016).

[63] 64ch multianode PMT assembly H8500C.

[64] MAROC | OMEGA - Centre de microélectronique.

[65] sbRIO-9651 - National Instruments.

[66] TDC-GPX2 | ams.

[67] W. Baldini, J. Inst. **12**, P03005 (2017).

[68] G. Baccani and et al., J. Inst. **13**, P11001 (2018).

[69] D. Bonanno and et al., Eur. Phys. J. Plus **134**, 281 (2019).

[70] Tadahiro Kin and et al., *Proceedings of International Symposium on Radiation Detectors and Their Uses (ISRD2016)*, No. 11 in *JPS Conference Proceedings* (Journal of the Physical Society of Japan, ADDRESS, 2016).

[71] S. Agostinelli and et al., Nuclear Instruments and Methods in Physics Research Section A: Accelerators, Spectrometers, Detectors and Associated Equipment **506**, 250 (2003).

[72] V. A. Kudryavtsev, Computer Physics Communications **180**, 339 (2009).

[73] Valentin Niess and et al., Computer Physics Communications **229**, 54 (2018).

[74] Domenico Lo Presti and et al., Sensors (Basel) **19**, (2019).

[75] Migliori Comunicazioni 2018.

[76] H. Tanaka, Muographers 2019: "Towards SDGs" Symposium | NEWS.

Acknowledgements

This is the end of my PhD and I have to admit that, first of all, it was an amazing experience. The research activities in which I was involved gave me the opportunity to learn a lot, not only from the side of scientific knowledge, but also about human relationships within a work group. I had the opportunity to travel from one end of the world to other, visiting Sao Paulo in Brazil and Tokyo in Japan, passing through Vienna. Every time that a journey in which you spent a lot of passion and energy come to an end it's hard to leave everything behind and the best way to close this experience is thanksgiving all the people which accompanied me.

Firstly, I would like to express my sincere gratitude to my supervisor Prof. Domenico Lo Presti for his continuous support of my PhD study and related research. He deserves a great plaudit for deciding three years ago to tackle the adventure of muography and all the successes that have been achieved so far have to be attributed primarily to him. His guidance helped me in all the time of research, but always allowing to follow my way in doing things. PhD is a step forward with respect to academic studies, is a time in which a young scientist should developed its individual ability in research and if I feel I have improved a lot, it's thanks to him.

Beside my supervisor, I would like to thank my thesis committee, Dr. Giovanni Bonanno and Prof. Giulio Saracino and, even if not included in the committee, Prof. Francesco Riggi. Their insightful comments and questions led me to widen my research from various perspectives.

A very special gratitude goes also to the current and former members

of the research team, Dr. Danilo Bonanno, Dr. Daniele Bongiovanni, Dr. Fabio Longhitano and Dr. Santo Reito. I learnt a lot from each one of them and I really appreciate the friendship which has been created with everyone. It was a pleasure to discuss with them out of the borders of our work.

Within the institutional framework, it has to be mentioned that the construction of the telescope was funded by FIR2014 (Future in Research) and strongly supported by Parco dell'Etna National Park, National Institute for Geophysics and Volcanology (INGV) and by the National Institute for Astrophysics (INAF).

Last but not least, I would like to thank my family and my life mate Federica: they have taught me everything I know beside of scientific knowledge, they've never let me miss their encouragement, they have always shown me their appreciation for every step forward I have taken in my work, they've sustained and stood me during the sleepless nights before the deadline of this thesis. I'm not gonna stop thanking them for what they did and will do for me, for my job and my life in general.

Ringraziamenti

Questa è la fine del mio dottorato e devo ammettere che, prima di tutto, è stata un'esperienza incredibile. Le attività di ricerca in cui sono stato coinvolto mi hanno dato l'opportunità di imparare molto, non solo dal lato della conoscenza scientifica, ma anche sulle relazioni umane all'interno di un gruppo di lavoro. Ho avuto l'opportunità di viaggiare da un capo all'altro del mondo, visitando San Paolo in Brasile e Tokyo in Giappone, passando per Vienna. Ogni volta che un viaggio in cui hai speso tanta passione ed energia si conclude è difficile lasciare tutto alle spalle e il modo migliore per concludere questa esperienza è ringraziare tutte le persone che mi hanno accompagnato.

In primo luogo, vorrei esprimere la mia sincera gratitudine al mio relatore, Prof. Domenico Lo Presti, per il suo continuo supporto al mio dottorato di ricerca. Merita un grande plauso per aver deciso tre anni fa di affrontare l'avventura della muografia e tutti i successi ottenuti finora devono essere attribuiti principalmente a lui. La sua guida mi ha aiutato in tutto il tempo della ricerca, ma mi ha sempre permesso di seguire il mio modo di fare le cose. Il dottorato è un passo avanti rispetto agli studi accademici, è un periodo in cui un giovane scienziato dovrebbe sviluppare le sue capacità individuali nella ricerca e se sento di essere migliorato molto, è merito suo.

Oltre al mio relatore, vorrei ringraziare la commissione della mia tesi, il Dr. Giovanni Bonanno e il Prof. Giulio Saracino e, anche se non incluso nel comitato, il Prof. Francesco Riggi. I loro commenti e le loro domande mi hanno spinto ad ampliare la mia ricerca da varie prospettive.

Un ringraziamento particolare va anche agli attuali ed ex membri del team di ricerca, il Dr. Danilo Bonanno, il Dr. Daniele Bongiovanni, il Dr. Fabio

Longhitano e il Dr. Santo Reito. Ho imparato molto da ognuno di loro e apprezzo molto l'amicizia che si è creata con tutti. È stato un piacere discutere con loro al di fuori dei confini del nostro lavoro.

Nell'ambito istituzionale, va ricordato che la costruzione del telescopio è stata finanziata dal FIR2014 (Future in Research) e fortemente sostenuta dal Parco Nazionale dell'Etna, dall'Istituto Nazionale di Geofisica e Vulcanologia (INGV) e dall'Istituto Nazionale di Astrofisica (INAF).

Infine, ma non per importanza, vorrei ringraziare la mia famiglia e la mia compagna di vita Federica: mi hanno insegnato tutto quello che so al di là delle conoscenze scientifiche, non mi hanno mai fatto mancare il loro incoraggiamento, mi hanno sempre dimostrato il loro apprezzamento per ogni passo avanti che ho fatto nel mio lavoro, mi hanno sostenuto e sopportato durante le notti insonni prima della scadenza di questa tesi. Non smetterò di ringraziarli per quello che hanno fatto e faranno per me, per il mio lavoro e per la mia vita in generale.